DEVELOPING A VALIDATED MODEL FOR PREDICTING GRAIN DAMAGE USING DEM

by

Zhengpu Chen

A Thesis

Submitted to the Faculty of Purdue University

In Partial Fulfillment of the Requirements for the degree of

Master of Science in Agricultural and Biological Engineering

School of Agricultural & Biological Engineering

West Lafayette, Indiana

August 2019

THE PURDUE UNIVERSITY GRADUATE SCHOOL
STATEMENT OF COMMITTEE APPROVAL

Dr. Kingsly Ambrose, Co-chair

School of Agricultural & Biological Engineering

Dr. Carl Wassgren, Co-chair

School of Mechanical Engineering

Dr. Richard Stroshine

School of Agricultural & Biological Engineering

Approved by:

Dr. Nathan Mosier

Head of the Graduate Program

To Mom and Dad

ACKNOWLEDGMENTS

I would like to express my deepest appreciation to my advisors, Dr. Kingsly Ambrose, and Dr. Carl Wassgren. Their ideas were always inspiring, and their guidance was invaluable when I met obstacles or lost direction. I would like to give my thanks to the committee member, Dr. Richard Stroshine, for his advice and support. He sets an example for me on how to be a good researcher. His breadth of knowledge and working ethic motivate me to learn more and work harder.

This project would not be possible without financial support from CNHi. I would like to thank the engineer from CNHi, Dr. Eric Veikle, for his insightful feedback and the help with the experiments.

I would like to acknowledge the assistance of the department lab managers, David Wilson and Scott Brand for constructing the experiment devices. They were always patient and would continue to help until the performance of the devices met my expectations.

Many thanks to my colleagues at CP3 group for listening to my ideas and problems and providing valuable suggestions. Special thanks to CP3 lab manager, Dr. Dhananjay Pai, who trained me to use the devices in the lab.

I would like to extend my sincere thanks to my friends, Dr. Zhihao Jia, Weijin Qiu, Mingyuan Chen, and Kunal Pardikar, who provide so many help and support in my daily life. They made my time at Purdue colorful and enjoyable. Finally, I would like to thank my family not only for their continuous love and support but also for teaching me how to be a good person.

TABLE OF CONTENTS

LIST OF TABLES

LIST OF FIGURES

ABSTRACT

Author: Chen, Zhengpu. MSABE
Institution: Purdue University
Degree Received: August 2019
Title: Developing a Validated Model for Predicting Grain Damage Using DEM
Committee Chair: Dr. Kingsly Ambrose and Dr. Carl Wassgren

Grain kernel damage during harvesting and handling continues to be a challenge in grain postharvest operations. The damage causes physical and physiological changes to grain, which reduces the grain quality and leads to significant yield loss. During harvesting and handling, grain kernels are subject to complex loading conditions consisting of a combination of impact, shear, and compression forces that can result in mechanical damage. Although there is considerable empirical data focused on kernel damage, there is a lack of generalizable mechanics-based predictive models. Mechanics-based models are desirable since they would be useful for providing guidance on designing and operating grain handling processes to minimize kernel damage and, thus, improve grain quality. The objective of the current study is to develop a mechanics-based model for predicting damage of corn and wheat kernels using the discrete element method (DEM).

The first step in DEM modeling is to determine the model input parameter values. This step is critical since the accuracy of the DEM simulations model is greatly affected by these parameters. The input parameters for the model developed in this current study are the physical and mechanical properties of corn and wheat kernels. These properties were determined by either direct measurement or calibration tests and validated with bulk material tests. X-ray micro-CT scanning method was used to acquire the grain kernel particle shape representation. The coefficient of friction (COF) was measured using a reciprocating pin tribometer. The coefficient of restitution (COR) was measured using the calibration method with a box containing multiple bins. The measured model parameter values were used to simulate common bulk material tests, i.e. bulk density and angle of repose. A comparison was made between the simulated results and the experimental measurements. The low percent error between experimental and simulated values indicate the accurate model parameter values estimation.

The damage resistance of corn and wheat kernels to compression, friction, and repeated impacts were measured using the universal testing machine, pin-on-disk tribometer, and Wisconsin

breakage tester, respectively. Lognormal distribution was used to model the compression test data, and three-parameter Weibull distribution was used to model the single and repeated impact test data. The statistical models were able accurately predict the damage probability based on the loading force or input energy. The wear damage was insignificant for corn-acrylic, corn-steel, and wheat-acrylic wear tests. For wheat-steel wear test, the average work done by the friction force to cause pericarp damage was 3.85 ± 1.50 J. The test results showed that the corn kernels were more susceptible to impact loading, while wheat kernels were more susceptible to compression loading. Both corn and wheat kernels had high resistance to wear damage.

The statistical model that predicts the impact damage probability based on impact energy was implemented in DEM. Stein breakage tester was used to validate the developed model. The damage level of the samples was then evaluated and compared with the predicted damage level output by the DEM simulation using the measured input parameters. However, it was found that the DEM simulation prediction error of damage level was high when the input parameters characterized by the Wisconsin breakage tester were used. The parameters were then recalibrated using Stein breakage tester. The model was able to give a good prediction on the damage fraction at different sample size and time levels when the recalibrated parameter values were used.

1. INTRODUCTION

1.1 Motivation

Grain kernel damage is problematic since it results in postharvest losses. The problem persists despite improvements in mechanical harvesting and handling techniques. Kernel damage causes physical and physiological changes in grain kernels, which reduces the grain quality and leads to significant yield and commercial losses. According to the *2016/2017 Corn Harvest Quality Report* [1], the average aggregate broken corn and foreign material (BCFM) percentage was 0.7% in the U.S. In BCFM-free corn, 4.8% of kernels were chipped and/or cracked, and another 4% of kernels contained internal stress cracks. In addition, 2.6% of the kernels were damaged by heat, frost, insects, sprouting, disease, weather, grounding, germ, and mold.

Although there is considerable empirical data focused on kernel damage, there is a lack of generalizable mechanics-based predictive models. Mechanics-based models are desirable since they would be useful for providing guidance on designing and operating grain handling processes to minimize kernel damage and, thus, improve grain quality.

The discrete element method (DEM) is a powerful modeling tool which has been widely used to simulate granular materials. DEM models the flow and mechanical behaviors of granular materials by tracking the particle motion and calculating the force applied to individual particles. Though validated DEM models have been developed to predict damage for rock during milling process [2], little public research has been found to model grain damage with DEM. There is great potential in developing and utilizing DEM for predicting grain kernel damage.

1.2 Objectives

The specific objectives of the current study are to:

- Give a comprehensive literature review on grain kernel damage, in terms of types of damage, sources of damage, damage prediction models, and experimental testing method.
- Characterize the physical and mechanical properties of the corn and wheat kernels for DEM simulation.
- Develop a grain damage prediction model and implement the model in DEM.

- Validate the developed model by comparing the results of the validation experiment and corresponding DEM simulation.

1.3 Chapter Outline

Studies were conducted based on the objectives and described in detail in the following chapters. A chapter outline is listed below

- Chapter 2: A comprehensive literature review was made on the types of grain kernel damage, sources of grain kernel damage, factors affecting damage, predictive damage models, and the experimental methods used to assess the damage.
- Chapter 4: The coefficients of friction of corn and wheat kernels were measured using a reciprocating-pin tribometer. The testing procedure and data analysis process were elaborated.
- Chapter 3: The material and interaction properties of corn and wheat kernels for DEM simulations were determined with direct measurement and calibration tests. The measured values were validated with bulk material tests and corresponding DEM simulations.
- Chapter 5: The damage resistance of corn and wheat kernels to compression, friction, and repeated impacts were quantified. The damage probability of the kernels was described with statistical models.
- Chapter 6: A damage model developed in Chapter 5 was implemented in DEM. The model was validated using a Stein breakage tester.
- Chapter 7: Conclusions were made and future work was suggested

1.4 References

[1] U.S. Grains Council. (2017). *Corn harvest quality report*. Retrieved from https://grains.org/wp-content/uploads/2018/02/2017-Corn-Harvest-Report.pdf

[2] Weerasekara, N. S., Powell, M. S., Cleary, P. W., Tavares, L. M., Evertsson, M., Morrison, R. D., … Carvalho, R. M. (2013). The contribution of DEM to the science of comminution. *Powder Technology*, *248*, 3–4. doi:10.1016/j.powtec.2013.05.032

2. A REVIEW OF GRAIN KERNEL DAMAGE: MECHANISMS, MODELING, AND TESTING PROCEDURES

2.1 Introduction

Grain kernel damage is a persistent problem in agricultural production. The causes of grain kernel damage vary greatly depending on kernel properties, environmental conditions, and harvesting and handling machine operational settings. The *Grain Inspection Handbook* published by the U.S. Department of Agriculture Grain Inspection, Packers and Stockyards Administration [1] categorizes corn kernel damage as being caused by heat, frost, extreme weather, sprouting, grounding, disease, insects, germ, or mold. To narrow the scope, the focus of this review is mechanical damage induced by harvesting and handling operations. This chapter presents a comprehensive review of the types of mechanical damage, sources of damage, factors affecting the level of damage, damage prediction models, and the experimental methods that assess damage.

2.2 Types of Damage

Mechanical, thermal, and biological damage are the three main types of grain kernel damage. The main interest of this review is mechanical damage. Mechanical damage can be classified into two categories based on the visibility of the damage, i.e., external and internal [2, 3]. External damage includes open cracks in the grain, while internal damage lies underneath the pericarp and cannot be detected without special instrumentation.

To describe the location of damage better, cross-sectional renderings of corn and wheat kernels are provided in Fig. 2.1. Grain kernels contain a germ or embryo that grows into a whole plant; a endosperm or cotyledon that is rich in protein, carbohydrate, and/or fat to provide sufficient nutrients for the germ to germinate; and a pericarp or bran that acts as a barrier and protects the grain kernel from outside damage and contamination.

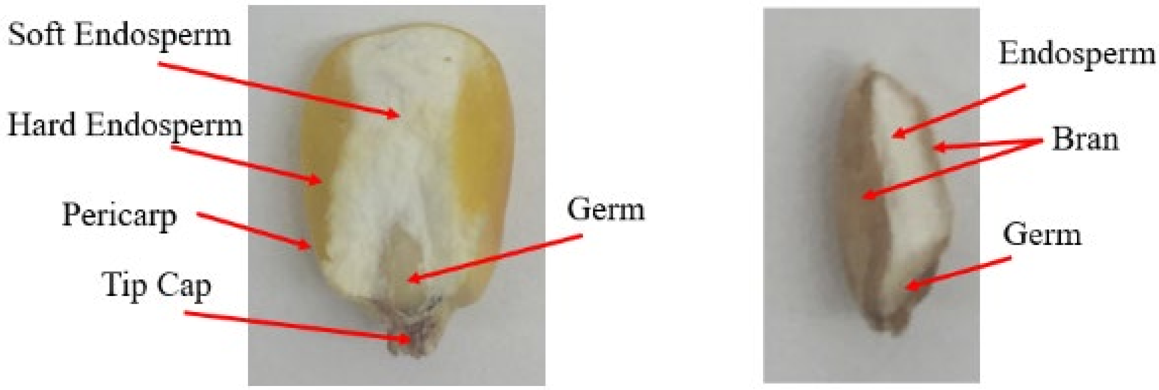

Fig. 2.1 Grain kernel cross sectional views. Left: corn; Right: wheat

2.2.1 External Damage

External damage includes broken, chipped, and scuffed kernels, or kernels with fine cracks on the pericarp that can be visually observed by the naked eye [4]. Various methods have been proposed to further classify external damage in order to assess the severity of damage. The earliest classification found in the literature was given by Koehler [5], who conducted a detailed study on corn pericarp injuries. Based on the location, the damage could be categorized into three major classes: 1. kernels with sound pericarps; 2. kernels with the tip cap broken off; and 3. kernels with a pericarp injury. Kernels with a pericarp injury could be further classified as having: 1. severe crown injury; 2. slight crown injury; 3. injury over the plumula; 4. injury over the radicle; 5. injury around the edge of the germ; or 6. other pericarp injuries.

The drawback of this classification method is that it requires an in-depth knowledge of grain kernel anatomy to assess the grain quality. In addition, relating the kernel damage to processing quality and storability is a challenging task. Chowdhury and Buchele [4] developed a numerical damage index to evaluate damage more critically, and is less subjective and now widely used for testing corn. The damage is assessed based on the change in the color of kernels with the application of a fast green dye. The dye only adheres to the starch, while the other parts of corn kernels do not react to the application of this dye. According to these authors, the severity of the damage can be classified into five levels: 1. broken kernels and fine material that pass through a 12/64-inch round-hole sieve; 2. severely damaged (broken, chipped, and crushed kernels, with more than 1/3 of the whole kernel missing); 3. major damage (open cracks, chipped, and severe pericarp damage highlighted by green dye); 4. minor damage (hairline cracks and spots of pericarp missing highlighted by green dye); or 5. sound kernels with no damage. Fig 2.2 is a picture of kernel samples illustrating the levels of damage.

Researchers have also strived to develop automatic methods for detecting grain kernel damage, which usually require a more simple and standardizable classification [6–11]. In a study on using a computer vision system to evaluate corn and soybean quality [7], external damage was categorized into three classes, i.e., broken (the original shape of the kernel is lost); chipped (white floury endosperm is exposed due to the loss of part of the pericarp and vitreous endosperm, but the overall kernel shape is unchanged); and starch-cracked (open pericarp with exposed endosperm). Overall, different methods have been proposed based on the objectives of the studies. However, there is still a lack of consensus on defining the severity of external damage.

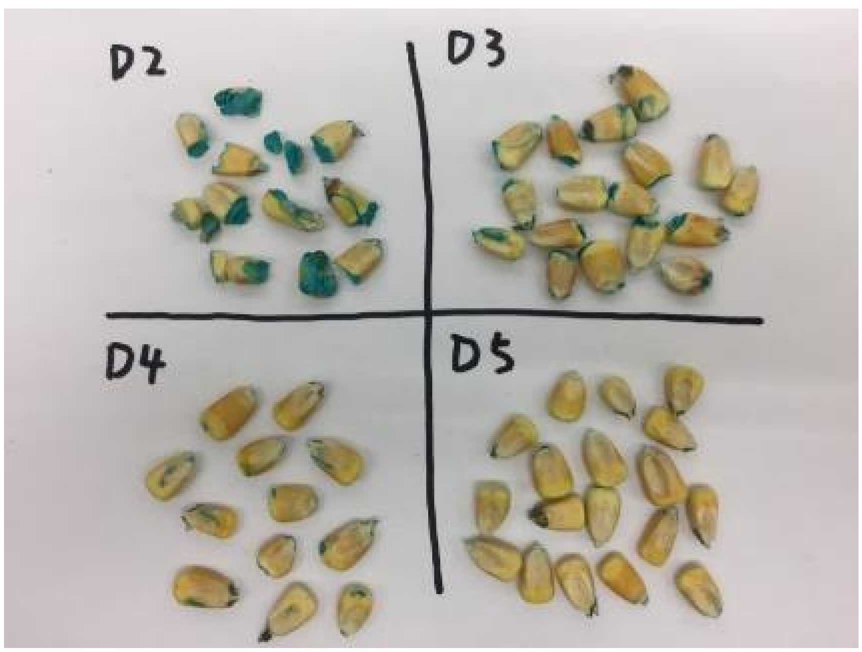

Fig. 2.2 Levels of grain damage. D2, severe damage (top left); D3, major damage (top right); D4, minor damage (bottom left); D5, Sound Kernel (bottom right)

2.2.2 Internal Damage

Compared with external damage, internal damage is harder to detect through visual inspection. The major internal damage that reduces corn quality is stress cracks. Gunasekaran et al. [12] defined stress cracks as the fine fissures in a kernel's endosperm, underneath the pericarp. The formation and propagation of internal stress cracks depend on the kernel's structure, composition, and variety. Microscopic structural analysis of kernel fissures was conducted by Robutti et al. [13], Balastreire et al. [14], and Gunasekaran et al. for corn [15]; Wang and Jeronimidis for wheat [16]; and Li and Mao for rice [17]. The microscopic analysis indicated that, in general, a stress crack develops as a single crack and progresses to multiple cracks. Multiple cracks appear as the internal stresses increase [18]. It is found that cracks usually initiate from internal flaws in the weaker region of the endosperm of the kernel [14]. With an increase in stress, cracks propagate through the cell walls around the starch granules towards the surface of the kernel. The most common cause of stress cracking is a rapid change in temperature and moisture [19–22], especially during drying and rewetting processes. Internal damage can also occur due to impact during harvesting and handling processes [23, 24].

With the cracks being internal, evaluation of kernel stress cracks requires special instrumentation. One simple and widely used method is to examine the kernels individually over a light source, such as a lightbox (Fig. 2.3) [21]. The backlight method can be used to quickly estimate the degree of internal damage for corn; however, the method is not applicable to grains that have low transmittance, such as wheat. Similar visualization methods include computer vision [12, 25], scanning electron microscopy, and X-ray micro tomography (Fig. 2.4) [26–28], which have been adopted by researchers in recent years. Compared to backlighting the kernels, these methods are able to provide more information on the width, length, and location of stress cracks, along with how stress cracks propagate within the kernel. However, these tests are time-consuming and require costly equipment, restricting their widespread use.

Fig. 2.3 Corn kernel illuminated by back light. From Left to right: No stress crack; Single stress crack; Multiple stress cracks. Red outlines were drawn around the stress cracks

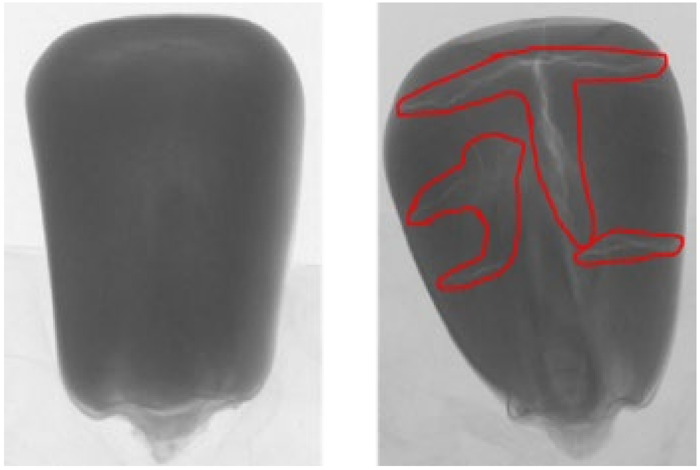

Fig. 2.4 X-ray images of corn kernels (Left: undamaged; Right: with internal stress cracks). Red outlines were drawn around the stress cracks

2.3 Negative Effects of Grain Mechanical Damage

External and internal damage in grain kernels affects their quality and leads to various challenges during downstream processes. The decrease in grain quality affects the kernel germinability, storability, feed value, handling, and processing characteristics. Mechanical damage has negative effects on various agricultural production processes (e.g., planting, storage, and food processing), and eventually results in yield and commercial losses. Low-quality grain also affects both human and livestock health. The following list summarizes the negative effects of external and internal damage:

- Significant mechanical damage to grain kernels leads to a lower grade and typically a price discount.
- Minor damage, like chipped or hairline fissures on the pericarp, has little effect on grain germinability. However, missing a large fraction of the kernel and/or having deep cracks in the endosperm or germ may result in a significant decrease in germination rate [29].
- Grain kernels with a damaged seed coat are more susceptible to insect infestation and microbiological contamination, which decreases the allowable storage time, causes nutrient loss, and can even result in the presence of toxic compounds if certain types of fungi grow on the kernels [30, 31].

- Both internal and external damage decrease mechanical strength and increase the breakage susceptibility of the grain. Consequently, more serious physical damage could occur in downstream handling operations [32].
- Kernel damage also affects the grain's water absorption rate, which could lead to overcooking or undercooking during grain processing operations [33].
- The yield of large flaking grits in dry milling and the yield of starch in wet milling are lower for grain with a higher degree of breakage and more stress cracks [12, 20].

2.4 Sources of Damage

There are many mechanisms that can lead to grain kernel damage. Prior to harvest, damage occurs mainly from severe weather conditions and insect infestation. During harvesting and subsequent handling operations, grain is subject to impact, compaction, and frictional loads that can result in mechanical damage. Another major factor is the drying process used to reduce the kernel moisture content from harvest conditions (18 – 25%) to safe storage conditions (13 – 15%). The high-temperature air used for drying grains generates thermal and moisture stress gradients inside the kernels that can lead to internal cracks. During storage of damaged kernels, there will be an increased fungal growth and accompanying risk of contamination with mycotoxins due to easy accessibility to exposed starch and other components in the kernels.

2.4.1 Damage caused by machines

2.4.1.1 Harvesting

Mechanical damage caused during the combine harvesting process has been studied by many researchers [34–45]. These studies conclude that the harvesting process is the primary source of mechanical damage. To better illustrate the process, an internal view of a combine in an operating state is shown in Fig. 2.5. The harvesting process can be divided into four steps: cutting, threshing, separation, and cleaning [46]. Throughout the entire harvesting process, grain is subject to impact, friction, and compression loads.

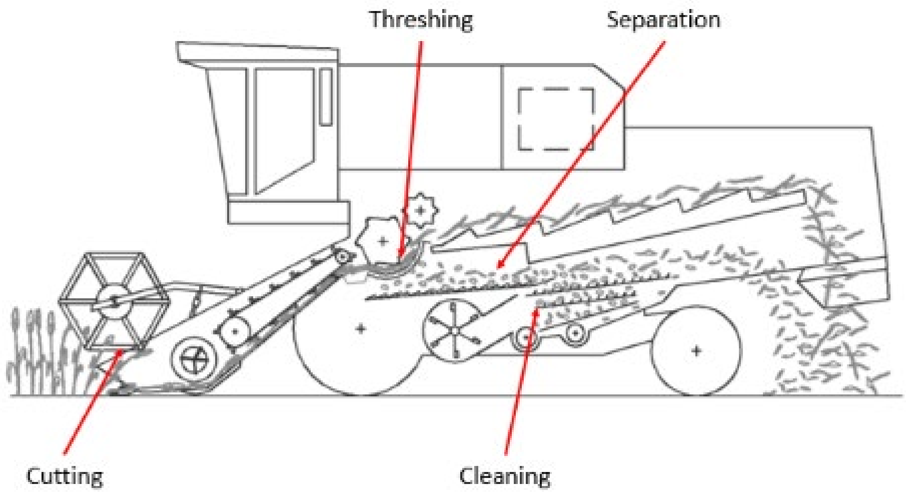

Fig. 2.5 Illustration of the combine harvesting process [47]

Among the four steps of the harvesting process, threshing is the primary source of mechanical damage [48]. In a combine harvester, threshing occurs between the cylinder and the concave. Threshing is the process of detaching grain from other parts of the plant by applying mechanical forces that create a combination of impact, shear, and compression [49]. An illustration of the threshing process is shown in Fig. 2.6. Even after threshing and before dropping through the concave opening, the detached kernels continue bouncing between the cylinder and concave bar. During this bouncing, the kernels are subjected to impact forces from the cylinder and concave bar and compressive forces from the threshing device and incoming plant material [48].

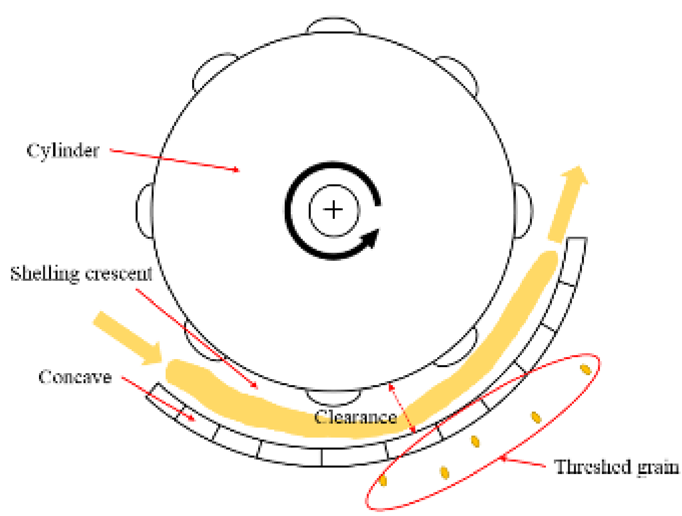

Fig. 2.6 Schematic of threshing process

Machine parameter settings of cylinder speed, concave clearance, and feed rate are the primary factors that affect the level of grain damage. Table 2.1 provides a summary of factors that lead to kernel damage during harvesting. Among these parameters, cylinder speed has the largest influence. At higher cylinder speeds, grain is subject to larger impulsive forces due to impacts with the cylinder, concave, and other kernels [34]. Compared to cylinder speed, concave clearance has a less significant effect on grain kernel damage. In general, a decrease in concave clearance results in an increase in mechanical damage [36, 37, 40, 44]. This trend occurs because a small concave clearance tends to increase the chance that grain kernels are jammed, and the grain kernels may be impacted multiple times in the shelling crescent (the space between the cylinder and the concave) before they exit the threshing chamber. The grain kernel damage level also decreases with an increase in feed rate [34, 37]. At a higher feed rate, plant material inside the machine is denser and cushions the grain from impacts.

Table 2.1 A summary of affecting factors related to combine harvesting operation

Factors	Grain type	Method/Devices used to test	Reference
Physical properties, morphological characteristics of corn and cob	Corn	Stationary laboratory sheller	[35]
Moisture content, cylinder speed, concave length	Corn	Stationary laboratory sheller	[38]
Types of combine harvester	Corn	Stationary laboratory sheller	[39]
Types of combine, cylinder speed, concave clearance	Corn	Field tests using combine harvesters	[44]
Moisture content, cylinder speed, concave length	Corn	Field tests using combine harvesters	[36]
Moisture content, cylinder speed, concave length	Corn	Stationary laboratory sheller	[48]
Concave length	Corn	Stationary laboratory sheller	[50]
Types of combine harvester	Corn	Field tests using combine harvesters	[51]
Corn ear orientation during shelling	Corn	Stationary laboratory sheller	[52]
Cylinder speed, cylinder inflation pressure	Corn	Stationary laboratory sheller (rubber roller sheller)	[53]
Grain variety, cylinder peripheral speed, moisture content, number of passes through thresher	Rice	Thresher	[45]
Cylinder speed, concave clearance, feed rate	Wheat	Stationary laboratory sheller	[34]
Type of thresher, moisture content, peripheral speed, total throughput	Wheat	Stationary laboratory sheller	[54]
Feed rate, cylinder speed, concave clearance	Wheat, barley	Stationary laboratory sheller	[37]
Moisture content, cylinder speed, concave length	Navy bean	Field test using combine harvesters	[40]
Types of combine, cylinder speed, concave clearance	Soybean	Field test using combine harvesters	[42]
Moisture content, cylinder speed, length of storage period after threshing	Soybean	Stationary laboratory sheller	[43]
Moisture content, cylinder speed, concave clearance, concave length, cylinder configuration, concave configuration	Soybean	Stationary laboratory sheller, field test using combine harvesters	[55]

Besides machine parameters, other influencing factors affecting damage include the kernel residence time within the shelling crescent and the corn ear orientation during shelling [48, 52, 55, 56]. A longer residence time inside the shelling crescent results in a larger number of impacts and longer loading durations. The level of damage increases almost linearly as the kernels travel further along the concave [56]. Mahmoud and Buchele [52] evaluated the effect of corn ear orientation on mechanical damage and found that the tip-in orientation caused a higher level of damage compared to the roll-in orientation.

2.4.1.2 Handling

The handling process is another major source of grain kernel mechanical damage. The most common handling equipment used by commercial and farm grain handlers, aggregators, and processors includes belt conveyors, drag chain/flight conveyors, screw/auger conveyors, bucket conveyors, and pneumatic conveyors [57]. Examples of these different kinds of conveyors are shown in ff 2.7. The degree of damage caused by handling equipment is considered to be one of the key factors in evaluating their performance. Thus, various laboratory and field experiments have been conducted by researchers to test the damage induced by different types of handling equipment [58–62]. However, most researchers limited the scope of their study to quantifying the damage and few conducted in-depth studies to understand the grain kernel damage mechanisms. Table 2.2 provides a summary of the influencing factors from handling operations. The major factors such as conveying speed, conveying distance, and feed rate are discussed in the following sections.

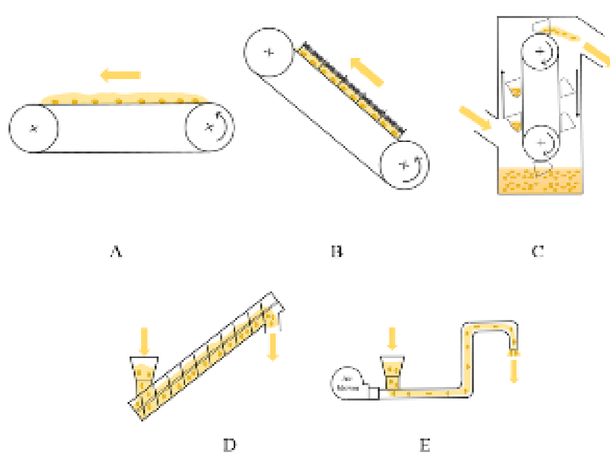

Fig. 2.7 Common mechanical handling devices used by the grain handling industry. From A to E: belt conveyor; flight conveyor; bucket conveyor; screw conveyor; pneumatic conveyor

Table 2.2 A summary of affecting factors related to handling operation

Factors	Grain Type	Handling system	References
Conveying speed, feed rate, conveying distance	Corn	Screw conveyor	[63]
Conveying speed, entrance opening height	Castor seed	Screw conveyor	[64]
Number of passes, screw-tube clearance	Wheat	Screw conveyor	[65]
Shape of grain, size of grain, screw-tube clearance	Spinach, rapeseed, millet, blue peas, wheat	Screw conveyor	[66]
Conveying speed, screw-tube clearance	Wheat	Screw conveyor	[67]
Air velocity, conveying distance, wheat variety, harvesting conditions	Wheat	Pneumatic conveyor	[68]
Air velocity, grain flow rate, conveying distance, discharge device	Corn	Pneumatic conveyor	[69]
Air velocity, feed rate	Corn	Pneumatic conveyor	[70]
Type of conveyor, conveying rate, grain variety, moisture content, drying condition	Corn	Drag conveyors	[61]
Type of conveyor, feed rate, number of passes, inclination angle, moisture content	Soybean	Steel-flighting screw conveyor, screw conveyor with rubber intake, steel-core bristle screw conveyor, rubber-flight conveyor, pneumatic conveyor, belt conveyor	[62]
Type of conveyor, feed rate, conveying speed, inclination angle, moisture content	Corn, soybean	Standard screw conveyor, perforated-tube screw conveyor, U-trough screw conveyor, vertical bucket elevator	[60]

A bucket elevator utilizes multiple buckets fixed on a moving belt to haul grain kernels vertically. Fiscus et al. [58], Foster and Holman [59], and Hall [60] experimentally quantified the grain mechanical damage caused by bucket elevators. Their results showed that the percent damage (by weight) was less than 3.2 % and the damage depended on the grain and handling conditions. Hall [60] identified that bucket elevators mainly damage grain during the process of filling-in and discharging the grain. The buckets impact the grain with a higher force when filling in at the bottom of the leg (boot section), and the grain impacts the housing at the head section at the top of the elevator during discharge. When working at a low capacity, the same grain would be hit by the bucket at the boot section more times than when working at a higher capacity. Thus, the damage created by the bucket elevator was higher compared with other handling systems.

Common screw conveyors consist of three basic components: a screw to move the material, a trough/casing/housing to contain the material and the screw, and a motor to drive the screw. The major function of the screw conveyor is to elevate and transport bulk material over short to medium distances [71]. This is achieved by pushing the material forward along the axis of the screw casing with the thrust movement of the rotating screw flight [72]. The sources of damage in screw conveyors can be classified into two categories: i) kernels shearing at the conveyor inlet section where the screw flight enters the casing, and ii) kernels jamming in the clearance between the screw flight and casing [66].

Screw conveyor machine or operational parameters affecting the damage level are conveying load, conveying speed, inclination angle, and clearance between the screw and the casing. Increasing the speed of conveying generates more damaged grain since, in such a condition, the grain kernels impact the casing wall at a higher speed [63, 64, 73]. Moreover, increasing the speed leads to a decline in conveyor filling percentage and a greater percentage of the grain is conveyed near the perimeter of the screw flight [74]. As a result, kernels have a higher probability of being jammed between the screw flight and the casing. Working at the rated capacity, there is less empty space within the conveyor and the grains cannot bounce around and strike on the wall or auger surfaces [60]. It was found that the damage during conveying increases significantly if the conveyor was operated below the rated capacity [62]. The effect of inclination angle on grain damage is inconsistent among articles. Experiments on shelled corn tested at zero and 50° [63] and on paddy tested at 10°, 20°, and 30° [73] indicated that inclination angle had no significant effect on damage level. However, an experiment on soybeans tested at 15° and 30° suggested that a significant amount of damage was produced when the angle of inclination was steep [62]. As for the effect of clearance on damage, a study showed that grain was more likely to be jammed when the size of the clearance was close to the size of the grain [75]. Theoretically, little jamming will occur if the clearance is much smaller than the grain size. The critical clearance that should not be exceeded in order to prevent the kernels from jamming can be estimated from the grain shape, the roundness of the screw blade edge, and the coefficient of friction between the grain and surface [66]. The cost of manufacturing goes up when the requirement for the clearance accuracy is high and, thus, clearances are generally not small. The mechanical damage also decreases with a screw-tube clearance much larger than the grain size; however, the conveying capacity for this configuration is low.

The quality of kernels has been found to only degrade slightly during pneumatic handling [68, 70]. Grain kernels are broken by high speed impacts against the conveying tube, especially at elbow sections. The other major cause of damage is getting crushed at airlock feeders [76]. The major mechanical parameters affecting the damage level are the air velocity and the conveying distance. A study on shelled corn damage in pneumatic conveyors reported that dust production and the percent fines increased exponentially when the air velocity exceeded a critical speed of 20 m/s [69, 70]. Converse et al. [68] studied mechanical damage to wheat in pneumatic conveyors and found that the grain kernel damage increased almost linearly with the conveying distance.

Grain kernel damage caused by belt conveyors and drag chain/flight conveyors is reported less frequently in the literature as compared to the previously discussed conveyors. Misra et al. [62] tested six soybean-seed conveyors for capacity and seed damage, including a steel flight auger, an auger with a rubber intake, a pneumatic conveyor, a rubber belt conveyor, a rubber flight conveyor, and a steel-core bristle auger. Compared with the other type of conveyors, damage by belt and flight conveyors was low (less than 1% by weight) during conveying. Johnson [61] quantitatively measured the shelled corn damage caused by drag conveyors and found that the percentage of broken corn increased by less than 1% after conveying for 30 meters. The drag conveyor type (flat bottom and U-trough) and conveying rate had no significant effect on the damage level. Mwaro et al. [77] determined the damage rate of shelled corn at various moisture contents transported using three different drag conveyors. The percentage of grain breakage ranged from 1.6% to 4.6%, with the highest damage occurring when the conveyor operated below the rated capacity (1/4th of the rated capacity). The study indicated that kernel damage was mainly the result of compression between the conveyor flight and casing.

Grain kernels are also subject to impact when free falling onto a hard surface, such as unloading grain from a combine into a cart or filling into a storage bin. Various drop tests were conducted with shelled corn, soybeans, and wheat [58, 59]. It was found that mechanical damage to the grain increases with the drop height. This is because, with increasing drop height, the kernels gain velocity that results in a large impact load [78]. Foster and Holman [59] suggested limiting the drop height to 12 meters (40 feet) to reduce the damage by free-fall. The damage depended on the type of grain when tested at the same conditions. Wheat was less susceptible to impact damage (percentage damage was less than 0.4%) than soybeans, and soybeans were less susceptible to impact damage than corn.

2.4.2 Other Sources of Damage

The primary focus of this study is mechanical damage caused by harvesting and subsequent handling operations. However, other sources of pre-harvest and post-harvest damage are discussed briefly in this section.

In order to increase storage life, grain is dried to a low moisture content before storing in a bin. Furthermore, during storage, rewetting (rehydration) could occur due to changes in ambient weather conditions. Many studies have described the kernel damaged caused by drying and rehydration [18–21, 79, 80]. Drying and rewetting generate temperature and moisture gradients within grain kernels that create internal tensile stresses [81]. Fluctuations in ambient temperature and relative humidity could induce internal stresses sufficiently large to cause stress cracks [79]. The factors affecting stress crack formation were summarized by Gunasekaran et al. [32] and include drying rate, temperature and moisture gradients, initial and final moisture contents, drying air temperature and airflow rate, and the type of corn. Improper drying or unfavorable storage conditions can increase grain kernel damage and susceptibility to damage through insect and mold growth during storage [31]. Damage caused by fungi in stored grains includes generating hot spots (fungi-induced hot spots have been reported to increase grain temperature up to 64 °C [82]), producing toxic substances (e.g., aflatoxins, ochratoxins, and fumonisins [83]), decreasing germinability, and causing nutrient loss. It was found that initial contamination level, temperature, moisture content, invasion of pests, and the type of storage containers used are the major factors affecting fungal growth in stored grain [31].

2.4.3 Cumulative damage

The damage level of grain increases from harvest to storage. Pierce and Hanna [84] simulated a sequence of on-farm handling processes, including harvesting, drying, and conveying, and measured the cumulative damage levels and breakage susceptibility after each process. The authors found that the type of damage was highly influenced by the method of handling and processing. Harvesting accounted for 60% of the seed coat damage while conveying accounted for 65% of the broken corn and fine material. Drying and cooling processes did not directly increase the external damage; however, they contributed to 40% of the breakage susceptibility, which significantly increased the probability of damage in subsequent handling operations.

2.5 Grain Kernel Properties and Handling Conditions Affecting Damage

In addition to harvest and handling methods, physical and mechanical properties of the grain kernels can affect damage susceptibility, such as moisture content and composition, as well as handling conditions such as grain impact velocity, contact surface type, angle of impact, and kernel orientation of loading. Table 2.3 summarizes the factors that lead to impact damage of kernels.

Table 2.3 A summary of affecting factors related to impact damage

Factors	Grain type	Method/Devices used to test	References
Moisture content, temperature, drop height	Pea bean	Free fall drop test	[24]
Type of handling, drop height, impact angle, impact surface, type of spout end, feeding method	Corn, soybean, wheat	Free fall drop test, grain thrower test, bucket elevator test	[58]
Type of handling, impact velocity, type of contact surface	Corn, soybean, wheat, pea bean	Free fall drop test, spouting drop test, grain thrower test, bucket elevator test	[59]
Impact velocity, moisture content	Soybean	Centrifugal impactor	[51]
Impact velocity, moisture content	Corn	Centrifugal impactor	[85]
Impact velocity, moisture content	Corn	Centrifugal impactor	[86]
Moisture content, impact velocity, type of impact surface, angle of impact surface, grain orientation	Corn	Pneumatic projector	[87]
Impact velocity	Cottonseed	Static rupture test (seed loading frame), impact rupture test (pneumatic projector)	[88]
Moisture content, impact velocity, grain orientation	Corn (with internal cracks)	Rotating synchronized disks impactor	[23]
Impact velocity, grain size, temperature, grain orientation, moisture content	Navy bean	Rotating synchronized disks impactor	[89]
Grain orientation, moisture content	Soybean	Rotating synchronized disks impactor	[90]
Impact velocity, moisture content	Kidney beans	Rotary hammer impactor	[91]
Impact velocity, number of impacts, moisture content	Wheat	Rotary hammer impactor	[92]
Moisture content, impact velocity	Chickpea	Rotary hammer impactor	[93]
Moisture content, impact velocity, grain orientation	Navy bean	Rotary hammer impactor	[94]
Moisture content, impact velocity	Soybean	Rotary hammer impactor	[29]
Impact velocity, moisture content, orientation	Cottonseed	Rotary hammer impactor	[95]
Contact surface hardness, grain orientation	Soybean	Rotary bars impactor	[96]
Moisture content, impact energy	Wheat, triticale seeds	Drop weight impactor	[97]
Moisture content, impact energy	Pinto bean	Drop weight impactor	[98]
Impact velocity, moisture content	Corn	Grain impact system	[99]
Grain size, moisture content	Corn	Rigid-hammer mill	[100]
Impact velocity, moisture content	Bambara nut	Slingshot impactor	[101]

2.5.1 Physical and Mechanical Properties

Moisture content is one of the most significant factors affecting the level of grain kernel damage. Mechanical properties, like failure strength, modulus of elasticity, and brittleness, are closely correlated with moisture content. Studies have shown that with an increase in kernel moisture content the breakage susceptibility first decreases and then beyond a certain moisture level it increases [102, 103]. Grain kernels at low moisture content are more likely to break since they are more brittle, less elastic, and have lower rupture energy than kernels at a higher moisture content [55, 104]. However, when the kernel moisture exceeds a certain limit, the kernels become too soft to withstand damage. It has been reported that there exists an optimum moisture content (wet basis) for specific types and variety of grain at which the damage would be minimized [93, 97], e.g., 13% for rapeseed [78], 28% for winter wheat [78], 20% for lentil seeds [79], and 17.5% for chickpea [93]. Compared with moisture content, other physical properties such as temperature, size, and shape, have less influence on grain kernel damage [87]. At low temperatures, grain is more brittle, so that handling induces more damage during winter than summer [58, 100]. Large kernels are more easily damaged than small kernels since larger kernels have more mass and, consequently, are subject to greater force during impact [89]. Experimental work has proved this effect of size on kernel damage for corn [100], soybean [51], and navy beans [89].

2.5.2 Effect of impact velocity, impact angle, impact surface, and kernel orientation

Impact damage is one of the major causes of grain breakage during harvesting and handling operations. The level of impact damage is mainly influenced by impact velocity, kernel orientation, angle of impact, and the surface on which the impact occurs.

Grain impact velocity, related to machine parameters such as cylinder rotational speed and conveying speed, is a significant parameter influencing the level of damage. Kernels impacting at a higher velocity are subjected to a higher impact load, which consequently leads to more damage. Empirical relationships correlating impact velocity and damage level have been developed for various kinds of grain through single kernel impact experiments [24, 85, 87, 89, 92, 104]. For corn and soybeans, the impact damage becomes significant when the impact velocity is higher than 10 m/s [23, 90]. For navy beans, as the impact velocity increased from 5 m/s to 15 m/s, the percentage of damaged beans increased from 0.17% to 32.88% [98].

Angle of impact, i.e., the angle between the direction of grain movement and the impact surface, also plays a role in damage level. Keller et al. [87] reported that reducing the angle of impact reduces kernel damage; however, the decrease in damage depended on the type of contact surface. For instance, reducing the angle of impact from 90° to 45° reduced kernel damage by 25% on steel and urethane surfaces, while the reduction on a concrete surface was less. The effect of kernel orientation varies with the grain type since the kernel shape, structure, and composition differ from one variety to another. Impact damage at different kernel orientations was studied by various researchers for corn [23], soybeans [90, 96], navy beans [89], barley [104], oats [104], and cottonseeds [95]. Taking soybeans as an example, impacting on the radicle resulted in a decrease in kernel germination rate while impacting on the cotyledon caused minor damage [90, 96]. Impact tests considering the influence of contact surface type showed that kernels impacting on a concrete surface experienced more damage than those impacting on steel, and grain-on-grain impact caused less damage than impacting on concrete and steel surfaces [58, 59, 87, 96]. These results demonstrate that kernels impacting on rougher and less resilient surfaces leads to an increased damage.

2.6 Models for Predicting Particle Damage

2.6.1 Models Developed for Grain Kernels

Damage prediction models for grain kernels are mostly derived from experimental data using regression analyses. A summary of a number of empirical models for grain impact damage is given in Table 2.4. It is worth noting that Shahbazi et al. conducted a series of impact damage tests on different grain types and varieties (including mung bean seeds [105], wheat [92, 97, 106], triticale seeds [97], pinto beans [98], lentil seeds [103], chickpea seeds [93], navy beans [94], and kidney beans [91]) at different moisture content levels, and constructed prediction models based on regression analyses. The problem with empirical models is that the regression results are dependent on the experimental method and material conditions [107]. It is challenging to compare models since the experiments used to generate the model data used different test apparatuses, grain varieties, velocities, and moisture contents. However, despite these limitations, empirical models have improved researchers' understanding of the factors that influence grain kernel damage. Moreover, these studies have greatly improved the development and refinement of the apparatuses used to generate kernel damage, e.g., the centrifugal impactor [51, 85, 86, 108, 109], the pendulum impactor [49], the pneumatic impactor [88], the rotary arm impactor [29, 92, 93, 102], the rotating disk impactor [23, 89, 90], the slingshot impactor [101], and the drop bar impactor [97], and approaches to assess damage, e.g., sieving and screening [58, 59], the fast green dye test [23, 87], the germination test [103], the light box test [23], and the x-ray analysis [89].

Table 2.4 A summary of empirical models for predicting grain impact damage

Grain type	Parameters tested[a]	Apparatus	Impact condition	Form of regression models[a]	Moisture content (%)[b]	Speed (m/s or rpm)	Reference
Cotton seed	V	Pneumatic impactor	Single kernel	$PD = \alpha \cdot V^{\beta}$	6, 10, 14	15.24, 20.32, 25.4, 30.48, 40.64	[88]
Soybean and shelled corn	V	Free fall drop test	In bulk	$PD = \alpha \cdot V^{\beta}$	Soybean: 11, 12.5; Corn: 13, 15	12.29, 15.87, 18.54	[59]
Bambara nut	V, MC	Slingshot impactor	Single kernel	$PD = \alpha e^{\beta V}$ $PD = b_0 + b_1 V$ $PD = b_0 + b_1 MC$	10, 20, 30, 40	3, 7, 11, 15	[101]
Soybean	MC	Rotary hammer impactor	Single kernel	$PD = \alpha e^{\beta MC}$	Aldana: 7.1, 11.5, 14.4, 16.3, 20.3; Polan: 7.9, 12.5, 14.6, 16.7, 19.9; Progres: 6.7, 12.5, 14.8, 17.2, 20.0	21.46	[29]
Rape seed and wheat	MC	Rotary hammer impactor	Single kernel	$PD = b_0 + b_1 MC + b_2 MC^2$	Wheat: 8, 12, 16, 20, 24, 28, 32; Rapeseed: 5, 7, 9, 11, 13, 15		[102]
Wheat and triticale seed	MC, impact energy level	Drop weight impactor	Single kernel	$PD = b_0 + b_1 MC + b_2 MC^2$	7.5, 12, 17, 22, 27		[97]
Navy bean	V, MC, kernel orientation	Rotary hammer impactor	Single kernel	$PD = b_0 + b_1 MC + b_2 MC^2$ $PD = b_0 + b_1 V + b_2 V^2$	10, 12.5, 15, 17.5, 20, 25	5, 7.5, 10, 12.5, 15	[94]
Bean seed after drying	N, MC	Centrifugal impactor	In bulk	$PD = b_0 + b_1 N + b_2 MC$	14, 17, 21	1,000, 1,500, 2,000, 2,500	[109]
Shelled corn	N, MC	Centrifugal impactor	In bulk	$PD = b_0 + b_1 N + b_2 MC \cdot N$ $+ b_3 MC^2$	8.5, 13.9, 18.9, 24.1, 29.2	2,000, 2,500, 3,000, 3,500, 4,000	[85]
Shelled corn	N, MC	Centrifugal impactor	In bulk	$PD = b_0 + b_1 N + b_2 MC + b_3 MC^2$	9.3, 14.1, 28	1,500, 2,000, 2,500, 3,000, 3,500	[86]
Chickpea	V, MC	Rotary hammer impactor	Single kernel	$PD = b_0 + b_1 MC + b_2 MC \cdot V + b_3 V^2 + b_4 MC^2$	7.5, 10, 12.5, 15, 17.5, 20	5, 7.5, 10, 12.5, 15, 17.5, 20	[93]
Kidney bean	V, MC	Rotary hammer impactor	Single kernel	$PD = b_0 + b_1 V + b_2 MC + b_3 MC \cdot V + b_4 V^2 + b_5 MC^2$	5, 10, 15, 20	5, 7.5, 10, 12	[91]
Wheat	V, MC, n	Rotary hammer impactor	Single kernel	$PD = b_0 + b_1 V + b_2 MC + b_3 n + b_4 V^2 + b_5 MC^2 + b_6 n^2$	7.5, 12, 15.3, 19, 23.3	5, 10, 15, 20, 25, 30	[92]
Corn before shelling	MC, cob MC, V, weight of ear, testing date (X_1-X_5)	Rotary impact testing machine	Impact whole ears, before shelling	$PD = b_0 + b_1 X_1 + \cdots + b_5 X_5 + b_{11} X_1^2 + \cdots + b_{55} X_5^2 + b_{12} X_1 X_2 + \cdots + b_{45} X_4 X_5$	6, 10, 14	12.7, 15.24, 20.32	[110]

[a] Percent damage, PD in %, is the number of damaged kernel divided by the total number of kernel used in test; Impact velocity, V in m/s, is the linear velocity when the kernel was impacted; Number of rotations, N in rpm, is the impeller speed of centrifugal impactor; Grain kernel moisture content, MC in % wet basis; Number of impact n; $\alpha, \beta, and\ b$ are constant determined by empirical data

[b] Grain kernel moisture content, MC in wet basis

Over the last decade, attempts have been made to develop mechanistic models for predicting grain kernel damage during handling processes. While empirical models are built on direct observation, measurement, and extensive data, mechanistic models describe the process based on an understanding of physics or chemistry [111]. For example, grain kernel damage has been modeled using the finite element method (FEM) [112] to give detailed force and deformation analysis on kernels. In FEM, the kernel is divided into a collection of connected elements, each of which follows a specified stress-strain relationship. The deformation of the system of elements is determined from Newton's Laws numerically. Xu et al. [113] used FEM to simulate impact between a threshing tooth and a single rice kernel. Based on a stress analysis in a single kernel, the critical velocity corresponding to the critical tensile stress (minimum stress that causes permanent plastic deformation or cracks) was predicted to be 29.5 m/s. The simulation prediction was close to the experimental result of 30 m/s. Another investigator modeled the compression of individual and bulk Jatropha curcas seeds in a container [114, 115]. The results of the model indicated that the coefficient of friction between seeds and between a seed and the container played a significant role in the initial stage of the pressing process. The authors observed that the information provided by the FEM model is useful for optimizing the design of oil pressing machines to increase energy efficiency.

In recent years, the discrete element method (DEM) has become a useful tool for studying the mechanics and dynamics of grain systems. In DEM simulations, the dynamics of every kernel is modeled [116]. At each time step in the simulation, kernel-kernel and kernel-boundary contacts are detected, the contact forces are then calculated based on a specific force model, and the kernel accelerations are found using Newton's Laws. These accelerations are then integrated in time to determine new kernel states. DEM has been used to investigate grain damage, including modeling of compression damage of rapeseed [117], damage of sorghum and wheat in a vertical screw conveyor [118], breakage of corn in drag chain conveyors [77], and wheat breakage during milling [119]. The lattice element method (LEM) is an intermediate approach between DEM and FEM and can be used to study the fracture of heterogeneous materials. LEM has been used to model the fragmentation of protein and starch components within wheat endosperm [120, 121].

Compared to empirical models, mechanistic models can provide deeper insight, can be applied to a greater variety of systems, and can be used to reduce experimental testing [111]. However, developing mechanistic models requires a fundamental understanding of the significant physics in the system. In addition, developing and running mechanistic models can be time-consuming.

2.6.2 Damage Models for Non-grain Materials

In this section, models that are developed and being used to predict the damage mechanisms in minerals and pharmaceutical compacts are described. Though the biological materials are very complex in terms of size, shape and chemical composition, these models could be adapted to predict the damage mechanisms in grain kernels. The application of these models for grain kernels would require assumptions to overcome the variability in kernels due to variety, physical characteristics, non-uniformity chemical composition, etc. However, appropriate adaption of these models would help develop improved mechanistic models using the modeling techniques such as FEM, DEM and LEM.

2.6.2.1 Impact Models

Though grain kernel impact damage is undesirable, impact-induced breakage of ore and rock is crucial in size reduction processes, thus it is widely studied in the science of comminution. The degree of impact damage is usually expressed as a function of impact velocity (v) or specific kinetic energy ($\frac{v^2}{2}$). Different forms of breakage probability models for single impacts were summarized by Rozenblat et al. [122] and include the logistic model [123], Weibull model [124–127], lognormal model [128], and power law model [129]. These models were developed to better predict particle fragmentation during size reduction and pneumatic conveying processes.

One commonly used analytical impact model, developed by Ghadiri and Zhang [130], predicts the single-impact attrition of particles with a semi-brittle failure mode. The model proposed that the fraction of material removed per impact, ξ, is,

$$\xi = \alpha \frac{\rho v^2 l H}{K_c^2} \tag{2.1}$$

where, α is a proportionality constant that is independent of material properties and particle size, ρ is the particle density, v is the impact velocity, l is the characteristic particle size, H is the particle's hardness, and K_c is the fracture toughness of the particle. The proportionality constant α can be determined from a single particle impact test [131]. The model was validated by comparing experimental test data collected using the impact device shown in Fig. 2.8. Particles made of ionic single crystals were fed into the device individually and accelerated by compressed air to a specific speed. The particle impacted perpendicularly against a rigid target and the mass loss of the particle was measured.

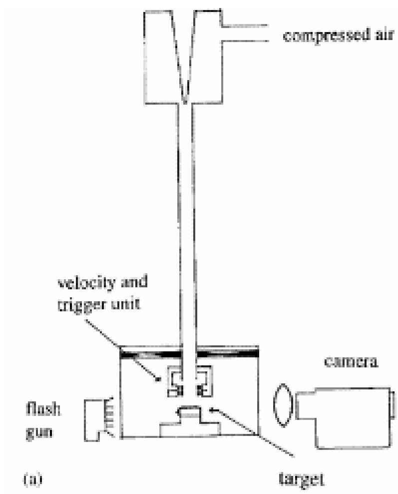

Fig. 2.8 Impact damage testing device (Ghadiri and Zhang Model) [130]

Using dimensional analysis, Vogel and Peukert [132] derived a fracture mechanics model to predict breakage probability, P_B,

$$P_B = 1 - \exp[-f_{\mathrm{Mat.}} xk \left(E_m - E_{m,\mathrm{min}}\right)] \tag{2.2}$$

where f_{Mat} is a material strength parameter, x is the initial particle size, k is the number of impacts, E_m is the mass-specific impact energy, and $E_{m,min}$ is the minimum specific impact energy below which breakage does not occur. The material parameters $f_{Mat.}$ and $E_{m,min}$ can be determined by single particle comminution experiments using the impact device developed by Schönert and Marktsheffel [133], as shown in Fig. 2.9. During the test, a single particle is fed into the disk-shaped rotor by the vibration feeder. The rotor accelerates the particle to a specified speed through centrifugal force. At the end of the radial channel in the rotor, the particle is released into an evacuated grinding chamber, then impacts on the saw tooth shaped target ring at an angle of 90°. A large number of particles (2500 particles for each test condition) were tested to acquire statistically reliable breakage probability parameters.

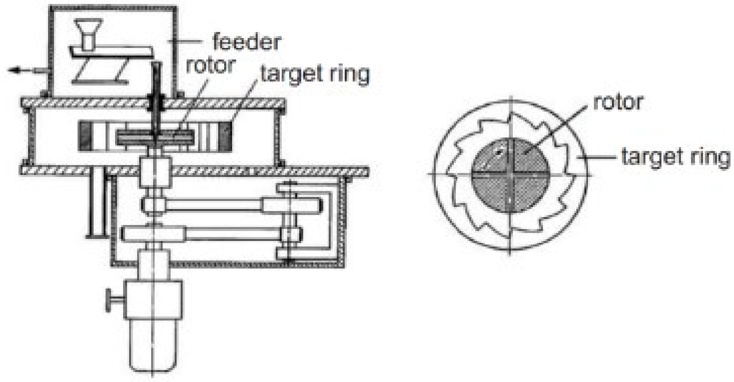

Fig. 2.9 Impact test device for Vogel and Peukert model [132]

Shi and Kojovic [134] proposed a modified Vogel and Peukert model to predict the breakage index, t_{10} (the cumulative percentage passing 1/10 of the initial size), instead of the breakage probability of the particle. The advantage of t_{10} is that it can be used to predict the full size distribution of the fragments. The parameter t_{10} can be expressed as follows,

$$t_{10} = M\{1 - \exp[-f_{\mathrm{Mat.}} xk\,(E_m - E_{m,min})]\} \tag{2.3}$$

where M is the maximum t_{10} value achievable in a single breakage event, and E_m, $E_{m,min}$, $f_{\mathrm{Mat.}}$, x, and k are the same as in equation (2.2). The model was validated using the data from drop weight tests on eight types of ore [135]. Using one set of model parameters ($E_{m,min}$ and f_{Mat}), the model was fitted to the whole data set for each ore type. The average R^2 value was 0.98 indicating that the model fits the data well.

2.6.2.2 Wear Model

Besides the damage caused by direct impact, shear also causes a significant amount of wear damage to particles [136]. Wear damage occurs during industrial processes such as fluidized bed drying and coating, cyclone separation, sandblasting, stirring, and bulk materials handling [137]. Meng and Ludema [138] and Zmitrowicz [139] reviewed the various wear models developed for solid materials. Meng and Ludema [138] reported over 300 prediction equations for friction and wear, and classified these equations into three categories: empirical relationships, contact-mechanics-based equations, and models based on material failure mechanisms. Zmitrowicz [139] provided an updated summary of wear relations along with a description of different wear patterns, including abrasion, ploughing, erosion, cavitation, corrugation, and fatigue.

In these models, the Archard wear model [140] is widely used for granular materials. When the deformation of the material is in the plastic range, the worn volume W is proportional to the applied load P and is independent of the apparent area of contact:

$$W = Ks\frac{P}{p_m} \tag{2.4}$$

where K is an empirically determined wear coefficient, s is the sliding distance, and p_m is the flow pressure, which is approximately equivalent to the hardness H of the softer contacting surface. A wide range of materials has been tested using a pin-on-disk system, as shown in Fig. 2.10, to acquire the K value and validate the model [141]. The test setup includes a pin and a flat circular disk positioned perpendicular to the pin. During the test, the pin presses against the disk at a specific load and the disk revolves around the disk center. The amount of wear on the pin can be quantified by its volume loss.

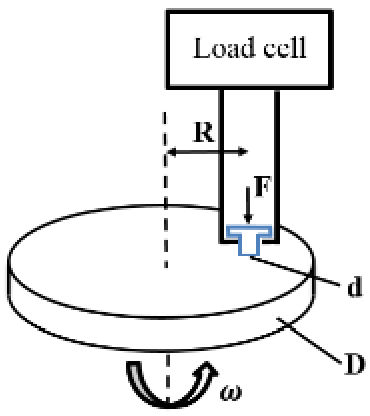

Fig. 2.10 Pin-on-disk wear test system. Here, F is the normal force acted on the pin, d is the pin or ball diameter, D is the disk diameter, R is the wear track radius, and ω is the rotation velocity of the disk [142]

Based on the empirical analysis on attrition of catalyst particles in a fluidized bed system, Gwyn [143] expressed particle attrition as a simple time-dependent power law relationship,

$$W = K_p t^m \tag{2.5}$$

where W is the weight fraction attrited, t is the attrition time, m is a constant independent of particle size, and K_p is a parameter that is a function of initial particle size. The relationship is usually used by replacing time t with shear strain Γ. Though the model generally fits the data well, it lacks a theoretical explanation and fails to give good predictions at large shear strains [144].

To account for the effect of applied normal stress σ, Ouwerkerk [136] modified Gwyn's formula to correlated attrition rate with $\Gamma\sigma^2$. The model has been found to provide a good fit to experimental data [145],

$$W = a\left[\Gamma\left(\frac{\sigma}{\sigma_{ref}}\right)^2\right]^b \tag{2.6}$$

where a and b are stress-dependent constants and σ_{ref} is a reference stress level.

Neil and Bridgwater [146] further studied the Gwyn model with the goal of improving prediction accuracy. Three devices, a fluidized bed, screw pugmill, and annular shear cell, were used for particle attrition experiments. The study found that a better fit was acquired when correlating the attrition rate with $\Gamma\sigma^{\phi}$, where ϕ was an empirically determined constant. In addition, they combined the Gwyn formula with the Schuhmann function, $W = W_T\left(\frac{d}{d_T}\right)^G$, to better describe the mass-size distribution,

$$W_T = A\left(\frac{\sigma\Gamma^{\phi}}{\sigma_{SCS}}\right)^{\beta} \tag{2.7}$$

where d is the average initial particle diameter, d_T is the diameter of the largest particle, W is the mass of degradation product having a size less than d, W_T is the mass of degradation product having a size less than d_T, G is Schuhmann size distribution modulus, A and β are empirical constants, and σ_{SCS} is the side-crushing strength of a single particle. The model was further validated by Bridgwater et al. [147] with annular shear cell tests. The authors proved the validity of the model for different particle shapes under a wide range of stresses and strains. Ghadiri et al. [145], however, pointed out that the model worked well only when fine debris was considered and not when large fragments were included in the model.

2.6.2.3 Fatigue Model

Fatigue damage may occur when a particle is subject to repeated loading and unloading. The fatigue damage of particles was examined by Jensen et al. [148] using the discrete element method (DEM) modeling technique. In their DEM simulation of particle damage, Jensen et al. [148] defined a critical energy density, W_0, and a total energy the particle can absorb before breakage W_i^{max},

$$W_i^{max} = W_0 V_i \tag{2.8}$$

where V_i is the volume of particle i. The authors proposed a particle damage criterion in which a particle would break only when the accumulated work done to particle i, W_i, is equal or greater than W_i^{max}. The particle would remain undamaged if $W_i < W_i^{max}$. The value of the critical energy density W_0 which gave the best correlation with DEM simulations was compared to experimental results using quartz sand and calcareous sand grain breakage [149]. The simulation and the values determined from experiments showed good agreement with each other.

Several fatigue models were developed based on the Vogel and Peukert (2004) model. Similar to Jensen et al. [148], a critical energy E_0 is defined in these modified Vogel and Peukert models. When the input energy is less than E_0, it is assumed that no damage was done to the particle. However, unlike the Jensen et al. model [148], when the work done on a particle is larger than the specific energy E_0, the particle damage probability increases with the cumulative effective energy $\sum_i(E_i - E_0)$, in which E_i is the impact energy in the i-th collision of the particle. An incremental breakage model based on the Vogel and Peukert model [132] was developed by Delaney et al. [150] to predict rock size and shape distributions during comminution in AG and SAG mills. The probability of a rock's "survival" decreases until the rock breaks. A modified model was developed to describe the daughter size distribution $t(k)$,

$$t(k) = A(k)\left\{1 - \left[\exp\left(b(k)\sum_i(E_i - E_0)\right)\right]\right\} \tag{2.9}$$

where $A(k)$ and $b(k)$ are coefficients for a set of $k = 6$ size classes from t_2 to t_{75}, which are calibrated from drop weight tests.

Capece et al. [151] modified the Vogel and Peukert model [132] to fit a typical milling process (e.g., a ball mill), during which a particle is impacted multiple times at different impact energies. The total number of impacts k in Eq. (2.9) is replaced with $\sum_{l=1}^{L} f_{coll,l}t$, i.e.,

$$P_B = 1 - \exp\left[-f_{\mathrm{Mat.}}x\sum_{l=1}^{L} f_{coll,l}\left(E_{m,l} - E_{m,min}\right)t\right] \tag{2.10}$$

where $f_{coll,l}$ is a collision frequency, t is milling time, and E_m, $E_{m,min}$, $f_{\mathrm{Mat.}}$, x, and P_B are the same as in equation (2.2). The model can be used to quantify milling performance with particle size interactions.

A limitation of the Vogel and Peukert and associated models is that they do not have parameters that explicitly account for the effect of material weakening by repetitive impacts [152]. A fatigue model proposed by Tavares [152] assumes that under repeated loading events, the stiffness of the particle decreases. This weakening effect can be described by a variable D, named the degree of damage. The degree of damage generated in the *n*th loading event D_n^* is calculated as,

$$D_n^* = \left[\frac{2\gamma}{(2\gamma - 5D_n^* + 5)}\frac{E_{k,n}}{E_{n-1}}\right]^{\frac{2\gamma}{5}} \tag{2.11}$$

where γ is an empirically determined damage accumulation coefficient, $E_{k,n}$ is the specific impact energy at the *n*th impact event, and E_{n-1} is the specific fracture energy of the particle before the *n*th impact. The diminishing stiffness leads to a decrease in the specific fracture energy. The relationship between the specific fracture energy before (E_{n-1}) and after (E_n) loading event *n* is as follows,

$$E_n = E_{n-1}(1 - D_n^*) \tag{2.12}$$

When the loading energy for a given loading event is larger than the specific fracture energy, the particle is considered to be broken. The advantage of this model is that only one parameter, i.e., the damage accumulation coefficient γ, needs to be fitted using experiment data acquired from impact or quasi-static compression tests.

A different approach to modeling fatigue damage is to calculate the decrease in particle strength [153] expressed in terms of a breakage force. The reduced compression strength after *n* loading events is modeled by,

$$\mathrm{F}' = \mathrm{F_m}\left\{1 + \frac{\mathrm{P_1}}{\exp\left[\mathrm{P_3} - \mathrm{P_2}(\mathrm{P}^*)^{\frac{1}{3}}\right]^2}\right\}^{-\frac{3}{2}\mathrm{n}} \tag{2.13}$$

where *F'* is the new compression strength, F_m is the initial compression strength, and P^* is the ratio between the applied normal compression stress and initial compression strength. P_1, P_2, and P_3 are model parameters evaluated by functions of the system and material properties. When implementing the model, P_1 can be assumed to be a constant, while P_2, and P_3 can be determined by fitting single particle impact test data.

2.7 Summary

This chapter reviews various aspects of grain kernel mechanical damage during harvesting and handling operations. The topics examined include the types of damage, sources of damage, factors affecting damage, and models used to predict kernel damage. Single kernel damage tests using lab built devices have been used to study the effect of loading conditions, physical and mechanical properties of the grain on damage level; while the bulk material damage tests using actual harvesting and handling equipment have been conducted to study the effect of operational settings on damage level.

Predicting grain kernel damage is challenging due to several reasons. First, kernel damage processes are complex, with the underlying processes remaining unclear or impractical to model precisely. Second, grain kernels are irregularly-shaped, anisotropic, heterogeneous, and non-linear viscoelastic materials. Moreover, the properties may change due to moisture content or biological activity [154]. Third, harvesting and handling operations create diverse loading conditions, which are hard to model exactly. Fourth, grain kernel damage can take different forms, e.g., different types of external and internal damage. Lastly, measuring and quantifying damage is challenging. There is no common agreement on how to quantify the severity of external damage and measuring the damage level can be time consuming depending on the method.

Various empirical models have been developed with regression analysis to correlate the damage level with the influencing factors. However, these models are essentially curve fits to considerable experimental data, which are often not generalizable and typically do not give insight into the physics of grain damage. Particle damage has been studied extensively for minerals, soils, composites, and pharmaceuticals, which have relatively homogeneous properties, but the damage prediction models for those material have not been widely extended to grains. According to this review, only a few studies have attempted to develop mechanics-based damage prediction models for cereal grains. More effort is needed in developing, applying, and validating the mechanics-based models since the models would be helpful in designing and operating handling and processing equipment to reduce damage and improve grain quality.

2.8 References

[1] USDA. (2013). *Grain inspection handbook. Book II, Chapter 4: Corn*. *Grain Inspection Handbook*. Retrieved from http://www.gipsa.usda.gov/publications/fgis/handbooks/gihbk2_insphb.html

[2] Chowdhury, M. H. (1978). *Development of a colorimetric technique for measuring mechanical damage of grain*. Iowa State University.

[3] Christenbury, G. D. (1975). *A photoelectric system for measuring mechanical damage of corn*. Iowa State University. Retrieved from http://lib.dr.iastate.edu/rtd

[4] Chowdhury, M. H., & Buchele, W. F. (1976). Development of a numerical damage index for critical evaluation of mechanical damage of corn. *Transactions of the ASAE*, *19*(3), 428–432.

[5] Koehler, B. (1957). *Pericarp injuries in seed corn: Prevalence in dent corn and relation to seedling blights*. University of Illinois. Agricultural Experiment Station.

[6] Gunasekaran, S., Paulsen, M. R., & Shove, G. C. (1986). Laser Optical Method for Detecting Corn Kernel Defects. *Transactions of the ASAE*, *29*(1), 294–298.

[7] Gunasekaran, S., Cooper, T. M., & Berlage, A. G. (1988). Evaluating quality factors of corn and soybeans using a computer vision system. *Transactions of the ASAE*, *31*(4), 1264–1271.

[8] Liao, K., Paulsen, M. R., Reid, J. F., Ni, B. C., & Bonifacio-Maghirang, E. P. (1993). Corn Kernel Breakage Classification by Machine Vision Using a Neural Network Classifier. *Transactions of the ASAE*, *36*(6), 1949–1953. doi:10.13031/2013.28547

[9] Ng, H. F. (1996). *Evaluation of mechanical and mold damage of shelled corn*. University of Minnesota.

[10] Steenhoek, L. W., Misra, M. K., Hurburgh, J., & Bern, C. J. (2001). Implementing a computer vision system for corn kernel damage evaluation. *Applied Engineering in Agriculture*, *17*(2), 235–240. doi:DOI: 10.13031/2013.5448

[11] Gong, Z. Y., Cheng, F., Liu, Z. H., Yang, X. L., Zhai, B. J., & You, Z. H. (2015). Recent Developments of Seeds Quality Inspection and Grading Based on Machine Vision. In *2015 ASABE Annual International Meeting*.

[12] Gunasekaran, S., Cooper, T. M., Berlage, a G., & Krishnan, P. (1987). Image processing for stress cracks in corn kernels. *Transactions of the ASAE*, *30*(1), 266–271.

[13] Robutti, J. L., Hoseney, R. C., & Wassom, C. E. (1974). Modified opaque-2 corn endosperms II: Structure viewed with a scanning electron microscope. *Cereal Chemistry*, *51*(2), 173–180.

[14] Balastreire, L. A., Herum, F. L., & Blaisdell, J. L. (1982). Fracture of corn endosperm in bending part II : Fracture analysis by fractography and optical microscopy. *Transactions of the ASAE*, *25*(4), 1062–1065.

[15] Gunasekaran, S., & Paulsen, M. R. (1985). Breakage Resistance of Corn as a Function of Drying Rates. *Transactions of the ASAE*, *28*(6), 2071–2076. doi:10.13031/2013.32568

[16] Wang, L., & Jeronimidis, G. (2008). Investigation of the fracture mode for hard and soft wheat endosperm using the loading-unloading bending test. *Journal of Cereal Science*, *48*(1), 193–202. doi:10.1016/j.jcs.2007.09.004

[17] Dong, L., & Mao, Z. (2003). Experimental Study on the Microscopic Structure of Stress Cracks of Rice Kernel after Sun Drying. In *2003 ASAE Annual International Meeting*.

[18] Thompson, R. A., & Foster, G. H. (1963). *Stress cracks and breakage in artificially dried corn*.

[19] Kunze, O. R., & Hall, C. W. (1965). Relative humidity changes that cause brown rice to crack. *Transactions of the ASAE*, *8*(3), 396–399.

[20] Brown, R. B., Fulford, G. N., Daynard, T. B., Meiering, a. G., & Otten, L. (1979). Effect of drying method on grain corn quality. *Cereal Chemistry*, *56*(6), 529–532.

[21] Kirleis, A. W., & Stroshine, R. L. (1990). Effects of hardness and drying air-temperature on breakage susceptibility and dry-milling characteristics of Yellow Dent Corn. *Cereal Chemistry*, *67*(6), 523–528. Retrieved from http://www.aaccnet.org/cerealchemistry/abstracts/1990/CC1990a123.asp

[22] George A. Ekstrom, J. B. Liljedahl, & and R. M. Peart. (2013). Thermal Expansion and Tensile Properties of Corn Kernels and Their Relationship to Cracking During Drying. *Transactions of the ASAE*, *9*(4), 0556–0561. doi:10.13031/2013.40033

[23] Moreira, S. M. E., Krutz, G. W., & Foster, G. H. (1980). Crack formation in corn subject to impact. *Transactions of the ASAE*, *24*(4), 889–892.

[24] Perry, J. S., & Hall, C. W. (1966). Evaluating and reducing mechanical-handling damage to pea beans. *Transactions of the ASAE*, *9*(5), 696–701.

[25] Reid, J. R., Kim, C., & Paulsen, M. R. (1991). Computer vision sensing of stress cracks in corn kernels. *Transactions of the ASAE*, *34*(5), 2236–2244.

[26] Wozniak, W. (2001). Mechanical properties of wheat grain in relation to internal cracks. *International Agrophysics*, *15*, 59–64.

[27] Guelpa, A., du Plessis, A., Kidd, M., & Manley, M. (2015). Non-destructive Estimation of Maize (Zea mays L.) Kernel Hardness by Means of an X-ray Micro-computed Tomography (μCT) Density Calibration. *Food and Bioprocess Technology*, *8*(7), 1419–1429. doi:10.1007/s11947-015-1502-3

[28] Sood, S., Mahajan, S., Doegar, A., & Das, A. (2016). Internal crack detection in kidney bean seeds using X-ray imaging technique. In *2016 International Conference on Advances in Computing* (pp. 2258–2261). doi:10.1109/ICACCI.2016.7732388

[29] Sosnowski, S., & Kuzniar, P. (1999). Effect of dynamic loading on the quality of soybean. *International Agrophysics*, *13*, 125–132.

[30] Harein, P., & Meronuck, R. (1990). Stored grain losses due to insects and molds and the importance of proper grain management. In *Stored Product Management* (pp. 29–31).

[31] Mohapatra, D., Kumar, S., Kotwaliwale, N., & Singh, K. K. (2017). Critical factors responsible for fungi growth in stored food grains and non-Chemical approaches for their control. *Industrial Crops and Products*. doi:10.1016/j.indcrop.2017.06.039

[32] Gunasekaran, S., Deshpande, S. S., Paulsen, M. R., & Shove, G. C. (1985). Size characterization of stress cracks in corn kernels. *Transactions of the ASAE*, *28*(5), 1668–1672.

[33] U.S. Grains Council. (2017). *Corn harvest quality report*. Retrieved from https://grains.org/wp-content/uploads/2018/02/2017-Corn-Harvest-Report.pdf

[34] Vas, F. M., & Harrison, H. P. (1969). The effect of selected mechanical threshing parameters on kernel damage and threshability of wheat. *Canadian Agricultural Engineering*, *69*(11), 83–91.

[35] Waelti, H., & Buchele, W. F. (1969). Factors affecting corn kernel damage in combine cylinders. *Transactions of the ASAE*, *12*(1), 55–59.

[36] Quick, G. R. (2003). Combine “sweet spot”: integrating harvested yield, grain damage and losses. In *Proceedings of the International Conference on Crop Harvesting*. Louisville, Kentucky.

[37] Špokas, L., Steponavičius, D., & Petkevičius, S. (2008). Impact of technological parameters of threshing apparatus on grain damage. *Agronomy Research*, *6*(Special issue), 367–376. Retrieved from http://agronomy.emu.ee/vol06Spec/p6S22.pdf

[38] Hall, G. E., & Johnson, W. H. (1970). Corn kernel crackage induced by mechanical shelling. *Transactions of the ASAE*, *13*(1), 51–55.

[39] Brass, R. W., & Marley, S. J. (1973). Roller shelter : low damage corn shelling cylinder. *Transactions of the ASAE*, *16*(1), 64–66.

[40] Pickett, L. K. (1973). Mechanical damage and processing loss during navy bean harvesting. *Transactions of the ASAE*, *16*(6), 1047–1050.

[41] Paulsen, M. R., & Nave, W. R. (1980). Corn damage from conventional and rotary combines. *Transactions of the ASAE*, *23*(5), 1110–1116. Retrieved from http://ovidsp.ovid.com/ovidweb.cgi?T=JS&CSC=Y&NEWS=N&PAGE=fulltext&D=caba1&AN=19812410750 http://oxfordsfx.hosted.exlibrisgroup.com/oxford?sid=OVID:cabadb&id=pmid:&id=doi:&issn=0001-2351&isbn=&volume=23&issue=5&spage=1110&pages=1110-1116&date=1980&title=T

[42] Newbery, R. S., Paulsen, M. R., & Nave, W. R. (1980). Soybean quality with rotary and conventional threshing. *Transactions of the ASAE*, *23*(2), 303–308. Retrieved from http://ovidsp.ovid.com/ovidweb.cgi?T=JS&CSC=Y&NEWS=N&PAGE=fulltext&D=caba1&AN=19800713601 http://oxfordsfx.hosted.exlibrisgroup.com/oxford?sid=OVID:cabadb&id=pmid:&id=doi:&issn=0001-2351&isbn=&volume=23&issue=2&spage=303&pages=303-308&date=1980&title=Tran

[43] Singh, K. N., & Singh, B. (1981). Effect of crop and machine parameters on threshing effectiveness and seed quality of soybean. *Journal of Agricultural Engineering Research*, *26*(4), 349–355. doi:10.1016/0021-8634(81)90076-7

[44] Ajllan, N. A. (1983). *Effect of combine cylinder design on mechanical damage of corn*. Iowa State University. Retrieved from http://lib.dr.iastate.edu/rtd%0Ahttp://lib.dr.iastate.edu/rtd/14467

[45] Sharma, A. D., Kunze, O. R., & Sarker, N. N. (1992). Impact damage on rough rice. *Transactions of the ASAE*, *35*(6), 1929–1934.

[46] Srivastava, A. K., Goering, C. E., Rohrbach, R. P., & Buckmaster, D. R. (2006). Grain Harvesting. In *Engineering Principles of Agricultural Machines* (2nd ed., pp. 403–435). St. Joseph, Michigan: American Society of Agricultural and Biological Engineers.

[47] Miu, P. (2014). *Combine Harvester Theory, Modeling, and Design*.

[48] Chowdhury, M. H., & Buchele, W. F. (1978). The nature of corn kernel damage inflicted in the shelling crescent of grain combines. *Transactions of the ASAE*, *21*(4), 610–614. Retrieved from http://ovidsp.ovid.com/ovidweb.cgi?T=JS&CSC=Y&NEWS=N&PAGE=fulltext&D=caba1&AN=19792402148 http://oxfordsfx.hosted.exlibrisgroup.com/oxford?sid=OVID:cabadb&id=pmid:&id=doi:&issn=0001-2351&isbn=&volume=21&issue=4&spage=610&pages=610-614&date=1978&title=Tran

[49] Srivastava, A. K., Herum, F. L., & Stevens, K. K. (1976). Impact Parameters Related to Physical Damage to Corn Kernel. *Transactions of the ASAE*, *19*(6), 1147–1151.

[50] Mahmoud, A. R., & Buchele, W. F. (1975). Distribution of Shelled Corn Throughput and Mechanical Damage in a Combine Cylinder. *Transactions of the ASAE*, *18*(3), 448–452.

[51] Paulsen, M. R., Nave, W. R., & Gray, L. E. (1981). Soybean Seed Quality as Affected by Impact Damage. *Transactions of the ASAE*, *24*(6), 1577–1582.

[52] Mahmoud, A. R., & Buchele, W. F. (1975). Corn Ear Orientation Effects on Mechanical Damage and Forces on Concave. *Transactions of the ASAE*, *18*(3), 444–0447.

[53] Chowdhury, M. H. (1973). *Effects of the operating parameters of the rubber roller sheller*. Iowa State University. Retrieved from http://lib.dr.iastate.edu/rtd%0Ahttp://lib.dr.iastate.edu/rtd/14474

[54] Wacker, P. (2005). Maize Grain Damage during Harvest. *Harvest Technology*, *60*(2), 84–85.

[55] Young, R. E. (1968). *Mechanical damage to soybeans during harvesting*. Iowa State University.

[56] Mahmoud, A. R. (1972). *Distribution of damage in maize combine cylinder and relationship between physico-rheological properties of shelled grain and damage*. Iowa State University.

[57] Labiak, J. S., & Hines, R. E. (1999). Grains and Grain Quality. In F. W. Bakker-Arkema (Ed.), *CIGR Handbook of Agricultural Engineering, Volume IV: Agro-Processing Engineeirng* (pp. 11–20). St. Joseph: American Society of Agricultural Engineers.

[58] Fiscus, D. E., Foster, G. H., & Kaufmann, H. H. (1971). Physical Damage of Grain Caused by Various Handling Techniques. *Transactions of the ASAE*, *14*(3), 480–485.

[59] Foster, G. H., & Holman, L. E. (1973). *Grain Breakage Caused by Commercial Handling Methods*. *Marketing Research Report* (Vol. No. 968).

[60] Hall, G. E. (1974). Damage during handling of shelled corn and soybeans. *Transactions of the ASAE*, *17*(2), 335–338.

[61] Johnson, R. S. (1984). *Damage to shelled corn during transport in drag conveyors*. Kansas State University.

[62] Misra, M. K., Shyy, Y., Baudet, L., & Marley, S. J. (1991). Conveyors for bulk handling of seed soybeans. *Applied Engineering in Agriculture*, *7*(6), 735–740.

[63] Sands, L. D., & Hall, G. E. (1971). Damage to Shelled Corn During Transport in a Screw Conveyor. *Transactions of the ASAE*, *14*(3), 584–585.

[64] Bouse, L. F., Schoenleber, L. G., & Porterfield, J. G. (1964). Screw Conveyor Capacity and Castor Seed Damage. *Transactions of the ASAE*, *7*(2), 152–156.

[65] Stevens, G. N. (1966). Aspects of the performance of small auger grain conveyors. *Journal of Agricultural Engineering Research*, *11*(1), 11–18. doi:10.1016/S0021-8634(66)80003-3

[66] Rademacher, F. J. C. (1981). On Seed Damage in Grain Augers. *Journal of Agricultural Engineering Research*, *26*, 87–96.

[67] Roberts, A. W., & Arnold, P. C. (1966). *Grain Damage due to Agricultural Machinery Part 1 - Harvesting Machines (survey only) and Auger Conveyors*. *Wollongong University College Bulletin*. Retrieved from http://ro.uow.edu.au/wucbull/6

[68] Converse, H. H., Rao, B. V., Hodges, T. O., & Chung, D. S. (1970). Mechanical Damage To Wheat in Pneumatic Conveying. In *Winter Meeting American Society of Agricultural Engineers American Society of Agricultural Engineers*.

[69] Baker, K. D., Stroshine, R. L., Magee, K. J., Foster, G. H., & Jacko, R. B. (1986). Grain Damage and Dust Generation in a Pressure Pneumatic Conveying System. *Transactions of the ASAE*, *29*(3), 840–847.

[70] Magee, K. J., Stroshine, R. L., Foster, G. H., & Baker, K. D. (1983). Nature and extent of grain damage caused by pneumatic conveying systems. In *Winter Meeting American Society of Agricultural Engineers American Society of Agricultural Engineers*.

[71] Jovanović, A., Pezo, L., Stanojlović, S., Kosanić, N., & Lević, L. (2015). Discrete element modelling of screw conveyor-mixers. *Hemijska Industrija*, *69*(1), 95–101. doi:10.2298/HEMIND130412026J

[72] Patel, J., Patel, S., & Patel, S. (2012). Review on numerical and experimental study of screw conveyor. *International Journal of Advanced Engineering Research Studies*, *I*(IV), 66–69.

[73] Zareiforoush, H., Komarizadeh, M. H., & Alizadeh, M. R. (2010). Effects of crop-machine variables on paddy grain damage during handling with an inclined screw auger. *Biosystems Engineering*, *106*(3), 234–242. doi:10.1016/j.biosystemseng.2010.02.008

[74] Bouse, L. F. (1956). *Some Screw Conveyor Parameters That Affect Capacity and Seed Damage*. Oklahoma State University.

[75] Roberts, A. W., & Willis, A. H. (1962). Performance of grain augers. *Proceedings of the Institution of Mechanical Engineers*, *176*(8), 165–194.

[76] Mwaro, W., Maranga, S., & Ikua, B. (2014). Establishing the Amount of Grain Breakage Taking Place in Bulk Maize during Conveyance through the Drag Chain Conveyor. *Proceedings of the 2012 Mechanical Engineering Conference on Sustainable Research and Innovation*, *4*, 166–172. Retrieved from http://www.jkuat-sri.com/ojs/index.php/proceedings/article/view/208

[77] Mwaro, W., Maranga, S., Ikua, B., & Kanali, C. . (2014). Modeling Maize Grain Breakage in the Drag Chain Conveyor Handling Systems. *Proceedings of 2014 International Conference on Sustainable Research and Innovation*, *5*, 124–128.

[78] Stephens, L. E., & Foster, G. H. (1977). Reducing Damage to Corn Handled through Gravity Spouts. *Transactions of the ASAE*, *20*(2), 367–371.

[79] White, G. M., Ross, I. J., & Poneleit, C. G. (1982). Stress Crack Development in Popcorn as Influenced by Drying and Rehydration Processes. *Transactions of the ASAE*, *25*(3), 768–772.

[80] Herter, U. (1987). *Effect of drying on corn seed quality*. Iowa State University.

[81] O. R. Kunze. (1979). Fissuring of the Rice Grain After Heated Air Drying. *Transactions of the ASAE*, *22*(5), 1197–1201. doi:10.13031/2013.35183

[82] Sinha, R., & Wallace, H. (1966). Association of granary mites and seed-borne fungi in stored grain and in outdoor and indoor habitats. *Annals of the Entomological Society of America*, *59*(6), 1170–1181. Retrieved from https://academic.oup.com/aesa/article-abstract/59/6/1170/98302

[83] Bullerman, L. B., & Bianchini, A. (2007). Stability of mycotoxins during food processing. *International Journal of Food Microbiology*, *119*(1–2), 140–146. doi:10.1016/j.ijfoodmicro.2007.07.035

[84] Pierce, R. O., & Hanna, M. A. (1985). Corn Kernel Damage During on-Farm Handling. *Transactions of the ASAE*, *28*(1), 239–242.

[85] Singh, S. S., & Finner, M. F. (1983). A Centrifugal Impacter for Damage Susceptibility Evaluation of Shelled Corn. *Transactions of the ASAE*, *26*(6), 1858–1863.

[86] Sharda, R. (1976). *A Mechanical Damage Susceptibility Tester for Shelled Corn*. Ohio State University.

[87] Keller, D. L., Converse, H. H., Hodges, T. O., & Chung, D. S. (1972). Corn Kernel Damage Due to High Velocity Impact. *Transactions of the ASAE*, *15*(2), 330–332.

[88] Kirk, I. W., & McLeod, H. E. (1967). Cottonseed Rupture from Static Energy and Impact Velocity. *Transactions of the ASAE*, *10*(2), 217–219.

[89] Hoki, M., & Pickett, L. K. (1973). Factors Affecting Mechanical Damage of Navy Beans. *Transactions of the ASAE*, *16*(6), 1154–1157.

[90] Bartsch, J. A., Haugh, C. G., Athow, K. L., & Peart, R. M. (1986). Impact Damage to Soybean Seed. *Transactions of the ASAE*, *29*(2), 582–586.

[91] Khazaei, J. (2009). Influence of Impact Velocity and Moisture on Mechanical Damage in Beans Influence of Impact Velocity and Moisture Content on Mechanical Damages of White Kidney Beans Under Loadings. *Cercetări Agronomice în Moldova*, *42*(1(137)), 5–18.

[92] Khazaei, J., Shahbazi, F., Massah, J., Nikravesh, M., & Kianmehr, M. H. (2008). Evaluation and modeling of physical and physiological damage to wheat seeds under successive impact loadings: Mathematical and neural networks modeling. *Crop Science*, *48*(4), 1532–1544. doi:10.2135/cropsci2007.04.0187

[93] Shahbazi, F. (2011). Impact damage to chickpea seeds as affected by moisture content and impact velocity. *Applied Engineering in Agriculture*, *27*(5), 771–775.

[94] Shahbazi, F., Saffar, A., & Analooei, M. (2011). Mechanical damage to navy beans as affected by moisture content, impact velocity and seed orientation. *Quality Assurance and Safety of Crops and Foods*, *3*, 205–211. doi:10.1111/j.1757-837X.2011.00114.x

[95] Clark, R. L., Welch, G. B., & Anderson, J. H. (1969). Effect of High-Velocity Impact on Germination and Crackage of Cottonseed. *Transactions of the ASAE*, *12*(6), 748–751.

[96] Evans, M. D., Holmes, R. G., & McDonald, M. B. (1990). Impact Damage To Soybean Seed As Affected By Surface Hardness and Seed Orientation. *Transactions of the ASAE*, *33*(1), 234–240.

[97] Shahbazi, F., Valizadeh, S., & Dowlatshah, A. (2012). Mechanical damage to wheat and triticale seeds related to moisture content and impact energy. *Agricultural Engineering International: CIGR Journal*, *14*(4), 150–155.

[98] Shahbazi, F., Saffar, A., & Analooei, M. (2011). Mechanical damage to pinto beans as affected by moisture content and impact energy. *Agricultural Engineering International: CIGR Journal*, *13*(2), Manuscript No.1867.

[99] Ajayi, O. A., & Clarke, B. (1997). High velocity impact of Maize Kernels. *Journal of Agricultural and Engineering Research*, *67*(2), 97–104. doi:10.1006/jaer.1997.0156

[100] Jindal, V. K., Herum, F. L., & Hamdy, M. Y. (1979). Selected Breakage Characteristics of Corn. *Transactions of the ASAE*, *22*(5), 1193–1196.

[101] Baryeh, E. A. (2002). A simple grain impact damage assessment device for developing countries. *Journal of Food Engineering*, *56*(1), 37–42. doi:10.1016/S0260-8774(02)00145-0

[102] Szwed, G., & Lukaszuk, J. (2007). Effect of rapeseed and wheat kernel moisture on impact damage. *International Agrophysics*, *21*(3), 299–304.

[103] Shahbazi, F., Valizade, S., & Dowlatshah, A. (2017). Mechanical damage to green and red lentil seeds. *Food Science and Nutrition*, *5*(4), 943–947. doi:10.1002/fsn3.480

[104] Bilanski, W. (1966). Damage resistance of seed grains. *Transactions of the ASAE*, *9*(3), 360–363.

[105] Shahbazi, F., Valizadeh, S., & Dolatshaie, A. (2011). Correlating the data on the mechanical damage to mung bean seeds under impact loading. *International Journal of Food Engineering*, *7*(6), Article 10. doi:10.1515/1556-3758.2649

[106] Shahbazi, F. (2012). A Study on the Seed Susceptibility of Wheat (Triticum aestivum L .) Cultivars to Impact Damage. *Journal of Agricultural Science and Technology*, *14*, 505–512.

[107] Anazodo, U. G. N., Wall, G. L., & Norris, E. R. (1981). Corn Physical and Mechanical Properties As Related To Combine Cylinder Performance. *Canadian Agricultural Engineering*, *23*(1), 23–30.

[108] Cooke, J. R., & Dickens, J. W. (1971). A Centrifugal Gun for Impaction Testing of Seeds. *Transactions of the ASAE*, *14*(1), 147–155.

[109] Ptasznik, W., Barnard, J., Giec, W., & Khan, A. A. (1995). Susceptibility of Bean Seeds to Thermal and Impact Damage. *Journal of Agricultural Engineering Research*, *61*(2), 137–144. doi:10.1006/jaer.1995.1040

[110] Burkhardt, T. H., & Stout, B. A. (1974). Laboratory Investigations of Corn Shelling Utilizing High-Velocity Impact Loading. *Transactions of the ASAE*, *17*(1), 11–14.

[111] Tham, M. (2007). *Overview of Mechanistic Modelling Techniques*. Retrieved from https://www.yumpu.com/en/document/view/17836401/overview-of-mechanistic-modelling-techniques

[112] Segerlind, L. J. (1984). Applied Finite Element Analysis. New York: Wiley. doi:10.1016/0898-1221(77)90080-3

[113] Xu, L., Li, Y., Ma, Z., Zhao, Z., & Wang, C. (2013). Theoretical analysis and finite element simulation of a rice kernel obliquely impacted by a threshing tooth. *Biosystems Engineering*, *114*(2), 146–156. doi:10.1016/j.biosystemseng.2012.11.006

[114] Petrů, M., Novák, O., Herák, D., & Simanjuntak, S. (2012). Finite element method model of the mechanical behaviour of Jatropha curcas L. seed under compression loading. *Biosystems Engineering*, *111*(4), 412–421. doi:10.1016/j.biosystemseng.2012.01.008

[115] Petrů, M., Novák, O., Herák, D., Mašín, I., Lepšík, P., & Hrabě, P. (2014). Finite element method model of the mechanical behaviour of Jatropha curcas L. bulk seeds under compression loading: Study and 2D modelling of the damage to seeds. *Biosystems Engineering*, *127*(1), 50–66. doi:10.1016/j.biosystemseng.2014.08.011

[116] Cundall, P. A., & Strack, O. D. L. (1979). A discrete numerical model for granular assemblies. *Géotechnique*, *29*(1), 47–65. doi:10.1680/geot.1979.29.1.47

[117] Raji, A. O., & Favier, J. F. (2004). Model for the deformation in agricultural and food particulate materials under bulk compressive loading using discrete element method. I: Theory, model development and validation. *Journal of Food Engineering*, *64*(3), 359–371. doi:10.1016/j.jfoodeng.2003.11.004

[118] McBride, W., & Cleary, P. W. (2009). An investigation and optimization of the "OLDS" elevator using Discrete Element Modeling. *Powder Technology*, *193*(3), 216–234. doi:10.1016/j.powtec.2009.03.014

[119] Patwa, A., Ambrose, R. P. K., & Casada, M. E. (2016). Discrete element method as an approach to model the wheat milling process. *Powder Technology*, *302*, 350–356. doi:10.1016/j.powtec.2016.08.052

[120] Topin, V., Radjaï, F., Delenne, J. Y., & Mabille, F. (2009). Mechanical modeling of wheat hardness and fragmentation. *Powder Technology*, *190*(1–2), 215–220. doi:10.1016/j.powtec.2008.04.070

[121] Chichti, E., Lullien-Pellerin, V., George, M., Radjai, F., Affès, R., & Delenne, J. Y. (2016). Bottom-up model for understanding the effects of wheat endosperm microstructure on its mechanical strength. *Journal of Food Engineering*, *190*, 40–47. doi:10.1016/j.jfoodeng.2016.06.009

[122] Rozenblat, Y., Grant, E., Levy, A., Kalman, H., & Tomas, J. (2012). Selection and breakage functions of particles under impact loads. *Chemical Engineering Science*, *71*, 56–66. doi:10.1016/j.ces.2011.12.012

[123] Petukhov, Y., & Kalman, H. (2004). Empirical breakage ratio of particles due to impact. *Powder Technology*, *143–144*, 160–169. doi:10.1016/j.powtec.2004.04.009

[124] Djamarani, K. M., & Clark, I. M. (1997). Characterization of particle size based on fine and coarse fractions. *Powder Technology*, *93*(2), 101–108. doi:10.1016/S0032-5910(97)03233-6

[125] Kapur, P. C., Pande, D., & Fuerstenau, D. W. (1997). Analysis of single-particle breakage by impact grinding. *International Journal of Mineral Processing*, *49*(3–4), 223–236. doi:10.1016/S0301-7516(96)00008-7

[126] Salman, A. D., Biggs, C. A., Fu, J., Angyal, I., Szabó, M., & Hounslow, M. J. (2002). An experimental investigation of particle fragmentation using single particle impact studies. *Powder Technology*, *128*(1), 36–46. doi:10.1016/S0032-5910(02)00151-1

[127] Cheong, Y. S., Reynolds, G. K., Salman, A. D., & Hounslow, M. J. (2004). Modelling fragment size distribution using two-parameter Weibull equation. *International Journal of Mineral Processing*, *74S*, S227–S237. doi:10.1016/j.minpro.2004.07.012

[128] Pocock, J., Veasey, T. J., Tavares, L. M., & King, R. P. (1998). The effect of heating and quenching on grinding characteristics of quartzite. *Powder Technology*, *95*(2), 137–142. doi:10.1016/S0032-5910(97)03333-0

[129] Duo, W., Boerefijn, R., & Ghadiri, M. (1996). Impact attrition of fluid cracking catalyst. In *Proceedings of the 5th International Conference on Multiphase Flow*. Nürnberg, Germany.

[130] Ghadiri, M., & Zhang, Z. (2002). Impact attrition of particulate solids. Part 1: A theoretical model of chipping. *Chemical Engineering Science*, *57*(17), 3659–3669. doi:10.1016/S0009-2509(02)00240-3

[131] Zhang, Z., & Ghadiri, M. (2002). Impact attrition of particulate solids. Part 2: Experimental work. *Chemical Engineering Science*, *57*(17), 3671–3686. doi:10.1016/S0009-2509(02)00241-5

[132] Vogel, L., & Peukert, W. (2005). From single particle impact behaviour to modelling of impact mills. *Chemical Engineering Science*, *60*(18), 5164–5176. doi:10.1016/j.ces.2005.03.064

[133] Marktscheffel, M., & Schönert, K. (1986). Liberation of composite particles by single particle compression, shear and impact loading. In *Proceedings, 6th European Symposium on Comminution, Nuremberg*.

[134] Shi, F., & Kojovic, T. (2007). Validation of a model for impact breakage incorporating particle size effect. *International Journal of Mineral Processing*, *82*(3), 156–163. doi:10.1016/j.minpro.2006.09.006

[135] Banini, G. A. (2000). *An integrated description of rock breakage in comminution machines*. University of Queensland.

[136] Ouwerkerk, C. E. D. (1991). A micro-mechanical connection between the single-particle strength and the bulk strength of random packings of spherical particles. *Powder Technology*, *65*(1–3), 125–138. doi:10.1016/0032-5910(91)80175-I

[137] Bemrose, C. R., & Bridgwater, J. (1987). A review of attrition and attrition test methods. *Powder Technology*, *49*(2), 97–126. doi:10.1016/0032-5910(87)80054-2

[138] Meng, H., & Ludema, K. (1995). Wear models and predictive: their form and content. *Wear*, *181–183*, 443–457. doi:https://doi.org/10.1016/0043-1648(95)90158-2

[139] Zmitrowicz, A. (2006). Wear patterns and laws of wear – a review. *Journal of Theoretical and Applied Mechanics*, *44*(2), 219–253.

[140] Archard, J. F. (1953). Contact and rubbing of flat surface. *Journal of Applied Physics*, *24*(8), 981–988. doi:10.1063/1.1721447

[141] Archard, J. F., & Hirst, W. (1956). The Wear of Metals under Unlubricated Conditions. *Proceedings of the Royal Society A: Mathematical, Physical and Engineering Sciences*, *236*(1206), 397–410. doi:10.1098/rspa.1956.0144

[142] ASTM. (2010). *G99 - Standard Test Method for Wear Testing with a Pin-on-Disk Apparatus*. West Conshohocken, PA. doi:10.1520/G0099-05R10

[143] Gwyn, J. E. (1969). On the particle size distribution function and the attrition of cracking catalysts. *AIChE Journal*, *15*(1), 35–39. doi:10.1002/aic.690150112

[144] Bridgwater, J. (2007). Chapter 3 Particle Breakage due to Bulk Shear. *Handbook of Powder Technology*. doi:10.1016/S0167-3785(07)12006-6

[145] Ghadiri, M., Ning, Z., Kenter, S. J., & Puik, E. (2000). Attrition of granular solids in a shear cell. *Chemical Engineering Science*, *55*(22), 5445–5456. doi:10.1016/S0009-2509(00)00168-8

[146] Neil, A. U., & Bridgwater, J. (1999). Towards a parameter characterising attrition. *Powder Technology*, *106*(1–2), 37–44. doi:10.1016/S0032-5910(99)00064-9

[147] Bridgwater, J., Utsumi, R., Zhang, Z., & Tuladhar, T. (2003). Particle attrition due to shearing-the effects of stress, strain and particle shape. *Chemical Engineering Science*, *58*(20), 4649–4665. doi:10.1016/j.ces.2003.07.007

[148] Jensen, R. P., Plesha, M. E., Edil, T. B., Bosscher, P. J., & Kahla, N. Ben. (2001). DEM Simulation of Particle Damage in Granular Media—Structure Interfaces. *International Journal of Geomechanics*, *1*(1), 21–39. doi:10.1061/(ASCE)1532-3641(2001)1

[149] Hoteit, N. (1990). *Contribution a l'Etude du Comportment d'Interface Sable Inclusion at Application au Frottement Apparent*. Institut National Polytechnique de Grenoble.

[150] Delaney, G. W., Cleary, P. W., Morrison, R. D., Cummins, S., & Loveday, B. (2013). Predicting breakage and the evolution of rock size and shape distributions in Ag and SAG mills using DEM. *Minerals Engineering*, *50–51*, 132–139. doi:10.1016/j.mineng.2013.01.007

[151] Capece, M., Bilgili, E., & Dave, R. N. (2014). Formulation of a Physically Motivated Specific Breakage Rate Parameter for Ball Milling via the Discrete Element Method. *AIChE Journal*, *60*(7), 2404–2415. doi:10.1002/aic

[152] Tavares, L. M. (2009). Analysis of particle fracture by repeated stressing as damage accumulation. *Powder Technology*, *190*(3), 327–339. doi:10.1016/j.powtec.2008.08.011

[153] Rozenblat, Y., Levy, A., Kalman, H., Peyron, I., & Ricard, F. (2013). A model for particle fatigue due to impact loads. *Powder Technology*, *239*, 199–207. doi:10.1016/j.powtec.2013.01.059

[154] Sarig, Y. (1991). Review: Impact loading associated with agricultural products. *International Journal of Impact Engineering*, *11*(3), 251–275. doi:10.1016/0734-743X(91)90038-H

3. MEASUREMENTS OF GRAIN KERNEL FRICTION COEFFICIENTS USING A RECIPROCATING-PIN TRIBOMETER

3.1 Introduction and Background

The coefficient of friction (COF) is the ratio of the friction force to the normal force between two objects. There are two types of coefficient of friction: the static COF (calculated from the frictional force before two objects start moving relative to each other) and the dynamic COF (less than or equal to the static COF, calculated from the friction force when two objects are moving relative to each other). The COF has a significant effect on grain flow and storage behavior; thus, it is an important property to consider when designing agricultural production machinery and equipment [1]. Applications of the COF in the design of material handling and storage devices include determining the allowable inclination angle for belt conveying, determining the angle of the chute that provides consistent flow (critical chute angle), predicting grain load and pressure distribution in storage bins, and determining the required strength of bin walls [2]. In addition, the COF is a critical input parameter for discrete element method (DEM) computer simulations, which model the dynamics of individual particles in a larger system.

The parameters that affect the COF have been discussed in detail by previous researchers [3]. Moisture content and contact material are two parameters that have a significant influence on the COF, while kernel orientation, sliding velocity, normal pressure, and the grain variety have minor effects [4]. In most of the published literature, the COF is reported to increase with an increase in moisture content since the adhesion force between the grain and the opposing surface is large at high moisture contents [5]. In addition, kernels soften at high moisture contents and, thus deform more significantly, producing larger contact areas and stronger bonds [4]. Some researchers have argued that there is a nonlinear relationship between the COF and moisture content, i.e., the COF first decreases then increases with an increase in moisture content [6]. The decrease in the COF with an increase in moisture content is explained by the surface moisture of the grain acting as a lubricant against the contact surface [7]. The roughness of the contact surface greatly impacts the COF, with rougher surfaces resulting in larger COFs. The COF has been mostly measured for grain contacting structural materials used in postharvest processes such as rubber (conveyor belt), concrete (ground), plywood (storage device), and galvanized metal (storage device, harvest and handling machinery) [8–10].

The COFs of various types of grain kernels have been measured in numerous studies as summarized in Table 3.1. Due to the difficulty in measuring the COF between individual grain kernels, the COF for kernel-kernel contact is usually estimated via bulk material experiments. Different methods for measuring the COF of grain kernels are found in the literature with no widely agreed upon standard method. The most commonly used tests are the tilting table test [11], the flat surface sliding test [12], the direct shear test [13], and the rotating disc test [14]. Each of these tests is discussed in the following paragraphs.

Table 3.1 Selected previous studies on measuring COF of grain kernels

Type of grain	**Type of COF**	**Type of surface**	**COF range**	**MC Range[a]**	**Test method**	**Reference**
Soybeans	Static	Wood, concrete, and galvanized steel	0.164-0.571	8-16 d.b.	Flat sliding (surface move)	[15]
Wheat	Dynamic	Stainless steel, aluminum, mild steel	0.35-0.6	9.8-17.8 w.b.	Flat sliding (surface move)	[12]
Corn	Static	Compressed plastic, plywood, and galvanized iron sheet	0.36-0.67	5.15-22 d.b.	Tilt sliding	[16]
Rice	Static, dynamic	Steel, wood, concrete	0.13-0.41	12 w.b.	Jenike shear cell tester	[13]
Legume seeds	Static, dynamic	galvanized metal, chipboard, mild steel, plywood, and rubber	0.2-0.7	5.66-13.25 w.b.	Flat sliding (box move)	[1]
Neem Nut	Static	plywood, galvanized iron sheet, mild steel, and glass	0.4-0.6	7.16-17.88 w.b.	Flat sliding (box move)	[17]
Pigeon pea	Static	Galvanized steel, plywood, teak wood	0.26-0.60	6.4-28.5 d.b.	Tilt sliding	[11]
Gram	Static	Galvanized steel, plywood, teak wood	0.384-0.651	9.95-31.9 d.b.	Tilt sliding	[18]
Green gram	Static	rubber, plywood, mild steel, galvanized iron, aluminum, and stainless steel sheet	0.344-0.625	8.39-33.40 d.b.	Tilt sliding	[5]
Fababeans Tick beans	Static	Plywood, galvanized steel	0.28-0.55	8.5-21.6 w.b.	Tilt sliding	[19]
Karingda seeds	Static	Plywood, mild steel, galvanized steel	0.23-0.91	5-22 d.b.	Tilt sliding	[9]
Lentil seeds	Static, dynamic	galvanized sheet metal, plywood and rubber surfaces	0.275-0.532	6.5-32.6 d.b.	Rotating disc	[20]
Lentil seeds	Static, dynamic	Galvanized iron, plywood, smooth concrete, glass sheets	0.368-0.490	10.33-21 w.b.	Flat sliding (box move)	[21]
Soybeans, red kidney beans unshelled peanuts	Static, dynamic	galvanized sheet metal, plywood and rubber surfaces	Dynamic 0.283-0.347 0.273-0.360 0.290-0.427	8-13 w.b. 10.4-15.1 w.b. 2.5-15.2 w.b.	Rotating disc	[22]
Sunflowers seeds	Static	Mild steel and galvanized iron	0.4-0.81	4-20 d.b.	Tilt sliding	[23]
Barly Corn	Dynamic	Steel, plywood	0.36-0.42 0.22-0.31	10-23 w.b. 10-24 w.b	Flat sliding (surface move)	[24]
Millet	Static	Plywood, mild steel and galvanized iron	0.36-0.79	5-22.5 d.b.	Tilt sliding	[25]
Cumin seed	Static	Mild steel, galvanized iron, stainless steel	0.37-0.70	7-22 d.b.	Tilt sliding	[26]
Cottonseed	Static	Stainless steel, galvanized iron, plywood, rubber	0.27-0.44	8.33-13.78 d.b.	Tilt sliding	[8]
Okra seed	Static	Aluminum, Bakelite, galvanized iron, mild steel	0.345-0.493	8.16-87.57 d.b.	Tilt sliding	[27]
Fenugreek (Trigonella foenum-graceum L.) seeds	Static, dynamic	Plywood, mild steel and galvanized metal	0.343-0.567	8.9-20.1 d.b.	Flat sliding (box move)	[28]
White Lupin	Static, dynamic	Galvanized steel, rubber	0.39-0.48	8.3-19.2 d.b.	Rotating disc	[29]
Safflower (var. Darab) seeds	Static	Compressed plastic, plywood, galvanized iron	0.34-0.57	4-22 d.b.	Tilt sliding	[30]
Hemp seed	Static, dynamic	Rubber, plywood, galvanized metal	0.27-0.49	8.62-20.88 d.b.	Flat sliding (box move)	[31]
Monogerm sugarbeet (Befa vulgaris var. altissima) seeds	Static, dynamic	Plywood, mild steel, galvanized metal	0.306-0.719 0.362-0.753	8.55-17.14 d.b. 6.88-19.28 d.b.	Flat sliding (box move)	[32]
Rough rice (Sorkheh and Sazandegi)	Static	Plywood, glass, concrete, galvanized iron	0.082-0.432	12-16 w.b.	Tilt sliding	[33]

[a] d.b. stands for dry basis moisture content; w.b stands for wet basis moisture content.

The tilting table or inclined plane test is one of the most commonly used methods for measuring the COF of bulk grain kernels on a surface. As shown in Fig. 3.1(a), a bottomless box filled with the grain sample is placed on an adjustable tilting surface comprised of the opposing material [5]. The frame of the box is raised slightly so it is not touching this material. The surface is tilted gradually until the box just starts to slide down the surface, which occurs when the component of the filled box's weight parallel to the surface just exceeds the friction force. The tilting angle is measured, and the static COF is calculated as,

$$\mu_s = tan\phi \tag{3.1}$$

where μ_s is the static COF and ϕ is the tilting angle.

The disadvantages of this method are that: 1. the test can only measure the static COF; 2. the COF is measured for kernels in bulk rather than for individual kernels; and 3. the kernels are not fixed in place and so there may be some inter-kernel movement that could affect the accuracy of the result. Several modified test systems have been developed by researchers to make up for these shortcomings. One system includes two light sensors at the two ends of the tilting surface to measure the sliding time over the sliding distance (distance between the sensors) [34].

The dynamic COF is calculated as,

$$\mu_d = tan\phi - \frac{2s}{gt^2cos\phi} \tag{3.2}$$

where μ_d is the dynamic COF, g is the acceleration due to gravity, t is the sliding time, and s is the sliding distance.

The kernels are still not fixed in this system and, thus, may roll against the surface. Another modified system, shown in Fig. 3.1(b), fixes three kernels on the bottom surface of a plate in a triangular arrangement and places the plate on top of the surface for which the COF is to be measured [35]. The tilt angle is recorded when the plate begins to slide. Though this method eliminates the effect of particle rolling, it is difficult to ensure that the plate is parallel to the bottom surface. Thus, the tilting angle could be different from what is measured.

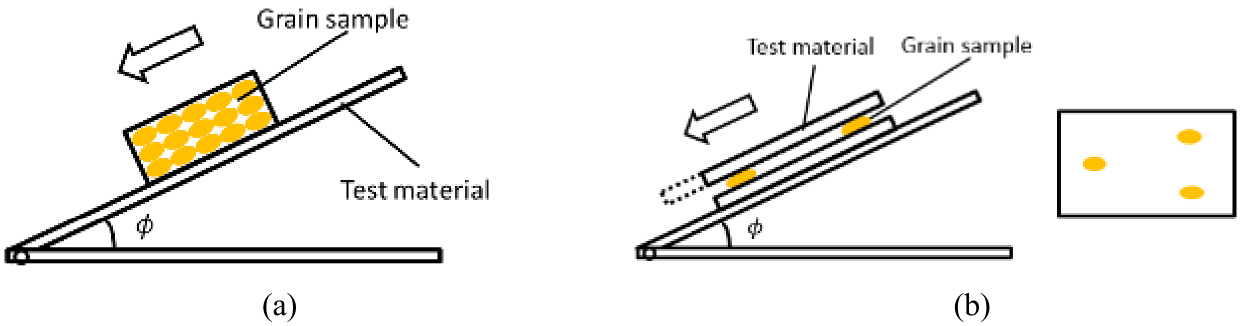

Fig. 3.1 Inclined surface test setup schematics. (a) Traditional setup; (b) Modified setup [35]; left: Side view of the test setup; right: Top view of the bottom surface

The flat surface sliding test is another widely used method [7, 17, 36]. A schematic of the test system is shown in Fig. 3.2(a). Similar to the tilting table test, the flat surface sliding test also uses a bottomless box containing a grain sample on a flat surface of the test material. An additional normal load can be applied to the top of the grain by adding weights on the loading pan. Either the box or the bottom surface is fixed and the other component is pulled horizontally by a mechanical driving unit at a constant rate. Using a similar setup, a Jenike shear cell (direct shear test) is the recommended test apparatus in Eurocode 1, Part 4 [37] for measuring the particle-wall friction coefficient. In this test, the friction force, which equals the horizontal pulling force, is measured using a data acquisition system [13, 38, 39]. The total normal force is the sum of the grain weight and applied normal load. The maximum value of the friction force (the static friction force) is acquired when the box and the surface just start to move relative to each other. The dynamic friction force is obtained after the components move relative to each other at a constant speed. The static and dynamic COF are calculated as,

$$\mu_s = \frac{f_s}{N}, \quad \mu_d = \frac{f_d}{N} \tag{3.3}$$

where f_s is static friction force, f_d is the dynamic friction force, and N is the normal force.

This method is able to measure both static and dynamic COFs; however, the disadvantage of the method is that the grain kernels are not fixed and could potentially roll during testing. A modified version of the flat surface sliding test device (Fig. 3.2(b)) was developed to measure the COF of a single kernel. In this device, the surface material slides between two fixed grain kernels [40]. However, during the pulling process, it is hard to keep the test material exactly vertical due to the irregular shape of the kernels.

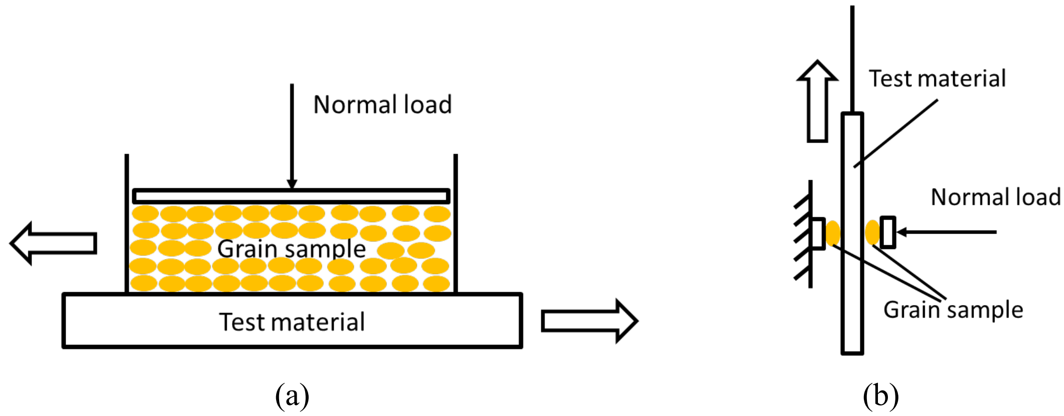

Fig. 3.2 Flat surface sliding test setup schematics. (a) Traditional setup; (b) Modified setup (side view) [40]

The rotating disc test system developed by Tsang-Mui-Chung et al. [14] and further improved by Chung and Verma [22] has been adopted by several studies to measure COFs. The device consists of a stationary sample box with baffles and a rotating disc with a driving unit (Fig. 3.3(a)). The grain kernels are placed on the rotating disc running at a constant speed. The torque on the driving shaft is measured using a data acquisition system. Similar to the flat surface sliding test, the static COF can be calculated from the maximum value of the torque and the dynamic COF can be calculated from the average value of the torque as the grain and disc slide against each other,

$$\mu_s = \frac{T_s}{pW}, \mu_d = \frac{T_d}{pW} \tag{3.4}$$

where T_s is the maximum value of the torque, T_m is the average value of the torque, p is the torque arm length, and W is the sample weight. The drawback of the system is that the friction between the grain and baffles causes overestimation of the COF. Moreover, the kernels may roll on the disc when the rotation speed exceeds a certain level [20]. Another rotational type of friction measurement device (Fig. 3.3(b)) was developed by Lawton [6]. An annular friction plate made of the test material is pressed on top of the grain kernels inside a cylinder. During the test, a torque is gradually applied to the plate using a torque wrench. The normal load and the torque that lead to relative motion between the plate and the kernels is recorded. The friction between the cylinder wall and the grain kernels and potential rolling of kernels can reduce the accuracy of the result.

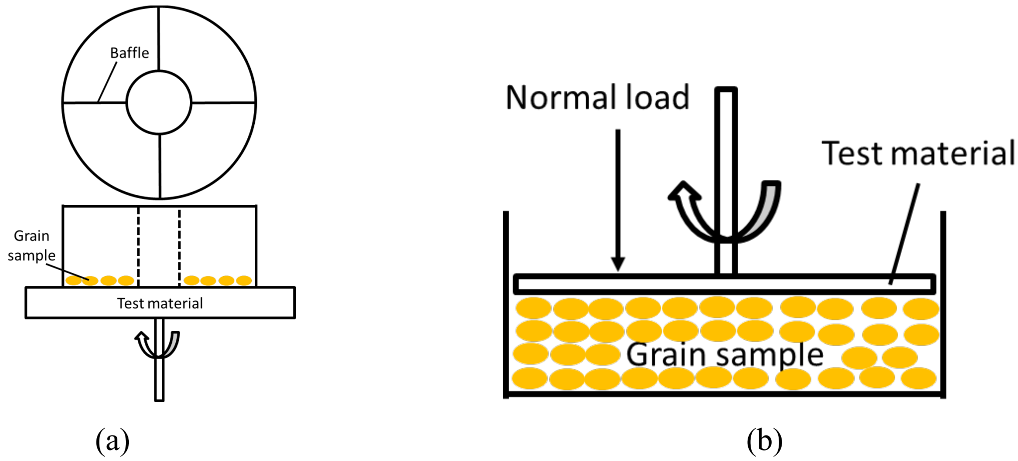

Fig. 3.3 Rotating disc test setup schematics. (a) Tsang-Mui-Chung et al. [14]; (b) Lawton [6]

Other apparatuses and methods for measuring the frictional properties of materials are listed by the American Society for Testing and Materials (ASTM) [41]. One widely used device for measuring the COF is the tribometer. The main advantages of this device are that it has a high data acquisition rate and provides highly accurate measurements. Various tribometer configurations can be used depending on the type of contact (conforming and nonconforming contact). The commonly used configurations include pin/ball-on-disk (Fig. 3.4(a)), reciprocating pin/ball (Fig. 3.4(b)), and block-on-ring (Fig. 3.4(c)). A tribometer is suitable for measuring the COFs of inorganic material, e.g., metals [42] and ceramics [43], which can be easily manufactured into standard shapes like a sphere, cuboid, or cylinder for testing. The authors could find no previous studies in which a tribometer has been used to measure grain kernel COFs. The reason may be due to the difficulty in affixing irregular kernel shapes onto the tribometer and also methods for analyzing the tribometer data when irregular shapes are used.

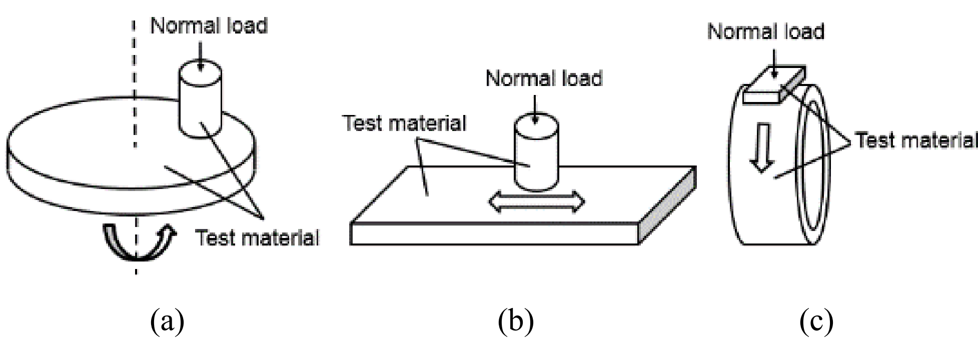

Fig. 3.4 Tribometer setup schematics. (a) Pin-on-disk; (b) Reciprocating pin; (c) Block-on-ring

A review of the literature demonstrates that a variety of friction test methods have been proposed, but these primarily utilize bulk grain which has the potential to roll during testing and affect the measurements. There are no methods that have been reported for measuring the friction coefficients between individual grain kernels. The objective of this study was to explore the use of a reciprocating pin tribometer for measuring the static and dynamic COFs of grain kernels. This paper describes the test equipment, methodology, and measurement data for particle-wall COFs (corn and wheat kernels on steel and acrylic surfaces) and inter-particle COFs (corn on corn and wheat on wheat).

3.2 Materials and Methods

In this study, the COFs for corn and wheat were measured. The corn and wheat samples were acquired from a farm located near Covington, Indiana. The moisture contents of the samples were determined using the oven dry method [44] to be 14.7% and 13.9% wet basis for corn and wheat, respectively. Before the test, the grain kernel samples were preserved in plastic bags to prevent the change of moisture contents. Low carbon steel and acrylic were selected for the boundary materials since they are common in harvesting, postharvest handling, and storage and laboratory testing systems. The materials were purchased in the form of flat sheets and then machined into circular disks of 2.75 in. diameter.

The static and dynamic COFs of grain were measured using a tribometer (UMT TriboLab) with a reciprocating friction test setup developed by Bruker Corporation (Billerica, MA). The reciprocating pin friction test has been widely used for COF measurements and a standard test procedure is given by ASTM [45]. The test setup has five main components: 1. the top sample holder with the sample; 2. the bottom sample holder with the sample; 3. the driving units; 4. the load cell; and 5. the data acquisition system (DAS). Photographs and schematics of the particle-wall and inter-particle friction test setups are shown in Fig. 3.5 and 3.6, respectively.

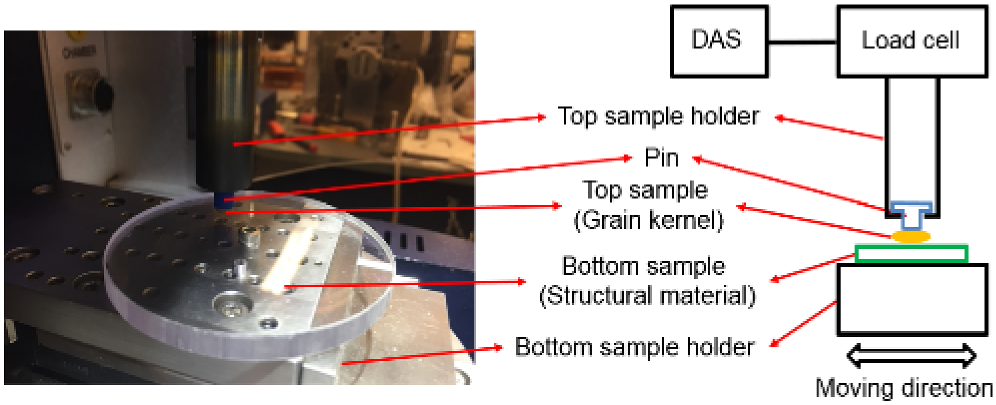

(a) (b)

Fig. 3.5 Particle-wall friction test setup. (a) Photograph; (b) Schematic.

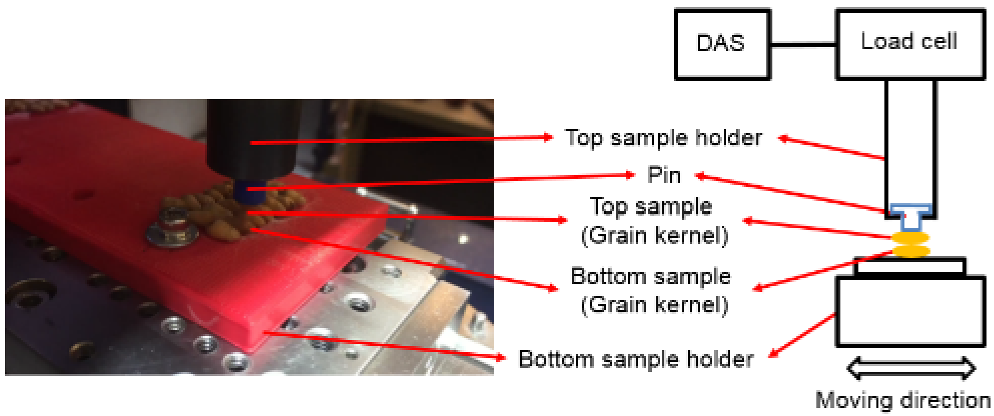

(a) (b)

Fig. 3.6 Inter-particle friction test setup. (a) Photograph; (b) Schematic

The standard test setup requires that the specimen be manufactured into a specific shape, such as a small cylinder or sphere. However, biological materials such as grain kernels cannot be manufactured into such shapes and, thus, specially designed top and bottom sample holders were made. A top sample holder pin was designed for holding a corn or wheat kernel on one end and attaching the other end to the load cell. Multiple pins were 3D-printed, so that a new pin would be used when a new sample kernel was tested. A single grain kernel was carefully superglued onto the pin. In order to provide a smooth contact surface, the germ side of the corn kernel and the crease side of the wheat kernel were glued onto the pin. The bottom setup varied depending on the type of friction test to be performed. For the particle-wall friction test, the test material was a circular disk that was directly affixed to the bottom sample holder with a screw. For the inter-particle friction test, multiple grain kernels were glued onto a 3D-printed plate. As with the top setup, the germ side of the corn kernel and the crease side of the wheat kernel were glued onto the plate. The 3D-printed plate was then fixed onto the bottom sample holder with a screw. The positions of the top and bottom samples were controlled by two driving units. The load cell and top sample holder were attached to the upper driving unit moving in the vertical direction while the bottom sample holder was attached to the bottom driving unit moving in the horizontal direction.

Before the test, the top and bottom samples were cleaned with isopropyl alcohol and lens cleaning tissue paper. The top sample was then lowered vertically until it came into contact with the bottom sample. The downward movement of the top sample stopped when the normal force measured by the load cell reached a specified level (2 N was used for the current study). The bottom sample was then moved horizontally via the driving unit. During the test, the normal force and tangential force applied to the top sample were measured by the load cell and recorded by the DAS with a data acquisition rate of 200 Hz. In addition, the top sample vertical position and the bottom sample horizontal position were measured as functions of time. For particle-wall measurements, the COF at a specific time, *t,* was calculated as,

$$\mu(t) = \frac{F_x(t)}{F_z(t)} \tag{3.5}$$

where $\mu(t)$ is COF at time *t*, $F_x(t)$ is the tangential force measured by the load cell at time *t*, and $F_z(t)$ is the normal force measured by the load cell at time *t*. For the inter-particle measurements, because the kernels are not flat, a coordinate transformation is required when calculating the COF. This topic is discussed in an upcoming paragraph.

The major device settings that affected the test results include the normal load, bottom driving unit speed, sliding distance, test run time, and ambient environmental conditions (temperature and relative humidity). The ambient environmental conditions were controlled between 20-25°C for temperature and 40-50% for relative humidity. To ensure other settings were chosen appropriately, preliminary tests were conducted at different loads, speeds, sliding distances, and run times. The study conducted by Hancock et al. [46] suggested that varying the normal force in the range of 1 N to 10 N has little influence on the dynamic COF values. In addition, other researchers have reported that a “skipping” was evident at low normal force and high velocity conditions, which affects the accuracy of the test [46]. For the current study, a low normal load of 2 N was used to prevent the kernel detaching from the pin and plate. A low driving unit speed of five cycles per minute (a cycle is defined as the bottom sample moving forward and then backward to the starting position) was used to avoid skipping. The horizontal sliding distance of the bottom sample holder was maintained between 600 to 800 μm per cycle. In the kernel-kernel friction tests, the contact surface between the kernels was curved. The small sliding distance was used to avoid drastically changing the vertical level of the top sample. A detailed discussion on the kernel-kernel friction test will be presented in section 3.3.2. As for sliding time, each test was run for one minute to acquire multiple sliding cycles with steady-state force measurements.

For each type of grain, three different kernels were randomly selected and used as the top sample. Nine reciprocating friction tests were conducted on each top sample for both the corn and wheat. The top sample was first slid against three randomly selected locations on the acrylic plate, then against three randomly selected kernels glued onto the 3D-printed plate, and finally three randomly selected locations on the steel plate. The test sequence was arranged based on the surface roughness of the test material to minimize wear damage to the sample. The preliminary tests indicated that the COF value did not change significantly after the kernel (top sample) was slid against the test material (bottom sample) for 15 minutes under the test conditions specified previously. Thus, the assumption was made that the surface roughness of the kernel did not change significantly throughout the test.

3.3 Results and Discussion

3.3.1 Particle-wall COF

A typical COF versus time plot from a particle-wall friction test is shown in Fig. 3.7. The value of the COF varied depending on the direction of movement of the bottom driving unit. A large "breakaway" tangential force was recorded when the samples just started to move relative to each other. The COF calculated from this breakaway force was considered to be the static COF. Though there was a small fluctuation due to the unevenness of the contacting surfaces, the COF value remained at a nearly constant value during steady state sliding. After a few seconds of sliding at a constant speed, the driving unit speed decreased quickly to zero. As the relative motion between the upper and lower sample stopped, the tangential force dropped to zero and the corresponding COF also dropped to zero. A “start-stop” period can be rendered as the time between the COF reaching the local peak value and dropping to zero. Within a one-minute test run, there were approximately eight to nine full start-stop periods. Only data from full start-stop periods were used when calculating COF results. Another phenomenon worth mentioning in Fig. 3.7 is that the COFs vary slightly depending on the direction of travel. The shape of the curve and the level of the COF values are similar for every other “start-stop” period, but slightly different for two neighboring “start-stop” periods. A small tilt in the plate may be one possible explanation of this phenomenon, which is discussed in detail in the next section (inter-particle COF). In addition, the surface texture of the kernel may also be a factor that leads to different COF values when the kernel travels in different directions.

A script was written in MATLAB to calculate the static and dynamic COFs. The static COF was calculated by averaging the peak values, which have been identified and circled in blue in Fig. 3.7. The dynamic COF was calculated by averaging the values generated during steady state sliding, which are identified in yellow in Fig. 3.7. The COF of a contact pair (e.g., corn-steel) was calculated by taking the average value of the nine replication tests. The results of the static and dynamic COFs measured for grain kernels against the two surfaces being tested are shown in Table 3.2.

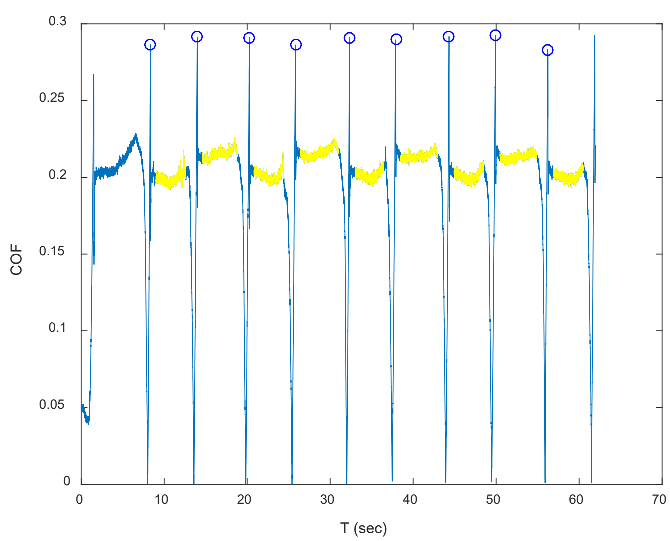

Fig. 3.7 Typical COF versus time plot of a particle-wall friction test (wheat-acrylic)

As expected, the static friction coefficient is larger than the dynamic friction coefficient, which is consistent for all test conditions. The COFs of a corn-wall combination is smaller than the corresponding wheat-wall combination (Table 3.2). This finding is consistent with expectations since the pericarp of the wheat kernel, which contains creases and bumps on the surface, is rougher than the pericarp of the corn kernel. The data indicates that for the same type of grain, the COFs for grain-steel measurements are larger than for grain-acrylic measurements.

Table 3.2 Static and dynamic COFs measured for grain kernels sliding against equipment surfaces

Type of grain kernel	**Moisture content[a]**	**Type of equipment surface**	**Type of COF**	**Mean**	**Standard Deviation**
Corn	14.7	Low carbon steel	Static	0.24	0.05
			Dynamic	0.22	0.06
Corn	14.7	Acrylic	Static	0.22	0.03
			Dynamic	0.16	0.01
Wheat	13.9	Low carbon steel	Static	0.32	0.02
			Dynamic	0.30	0.02
Wheat	13.9	Acrylic	Static	0.29	0.03
			Dynamic	0.20	0.02

[a] Moisture contents in wet basis.

The static and dynamic COFs of corn and wheat kernels sliding against a steel/iron plate have been reported in numerous studies as shown in Table 3.3. The measured COF values of different studies varied greatly even for the same material combination. It seems likely that the differences were caused by the differences in the surface finishes of the materials. For the corn-steel/iron combination, the static COF values range between 0.34 and 0.49. Only one reported a dynamic COF value, which was 0.25. For the wheat-steel/iron combination, the static COF values range between 0.42 and 0.64, and the dynamic COFs range from 0.19 to 0.51. It is found that the static COFs measured in the current study are smaller than the static COFs reported by previous studies that used the tilting table method. One possible explanation of the higher static COFs in previous studies is that the tilting angle at which the box just starts to slide is determined subjectively by the operator. The operator may tend to overestimate the tilting angle since it is challenging to accurately identify the incipient movement of the box and stop increasing the tilting angle immediately. The dynamic COFs measured in the current study show good agreement with the dynamic COFs reported in literature.

Table 3.3 Static and dynamic COFs of corn and wheat reported by previous studies

Type of grain kernel	Type of equipment surface	Type of COF	Mean	Moisture content[a]	Test method	Reference
Corn	Galvanized steel	Dynamic	0.25	16	Flat surface sliding	[47]
Corn	Galvanized iron Stainless steel	Static	0.34 0.33	13.8	Tilting table	[48]
Corn	Galvanized iron	Static	0.45	13.8	Tilting table	[16]
Corn	Galvanized iron	Static	0.49	12	Tilting table	[49]
Wheat	Stainless steel Low carbon steel	Dynamic Dynamic	0.34 0.31	14.0	Flat surface sliding	[12]
Wheat	Galvanized iron	Static	0.42	12	Tilting table	[50]
Wheat	Galvanized steel	Static	0.56	12.5	Tilting table	[51]
Wheat	Stainless steel	Dynamic	0.19	14.5	Flat surface sliding	[52]
Wheat	Galvanized steel	Static Dynamic	0.64 0.51	14.7	Tilting table Flat surface sliding	[53]

[a] Moisture contents in wet basis.

3.3.2 Inter-particle COF

A typical plot of the pin tangential force to normal force ratio as a function of time from an inter-particle friction test is shown in Fig. 3.8. Note that this is not a plot of the inter-particle COF since the pin tangential and normal forces are not the same as the tangential and normal contact forces between the particles due to the irregular particle shapes. Senetakis and Coop (2014) noted this same point when measuring the COFs of soil and mineral particles. The most notable feature in the plot is that the ratio of pin forces changes significantly depending on the direction of horizontal movement of the bottom driving unit during testing. This change in force ratio is due to the fact that the pin on which the load cells are mounted is moving up and down at an angle during testing. The analysis accounting for this motion is described in the following paragraphs.

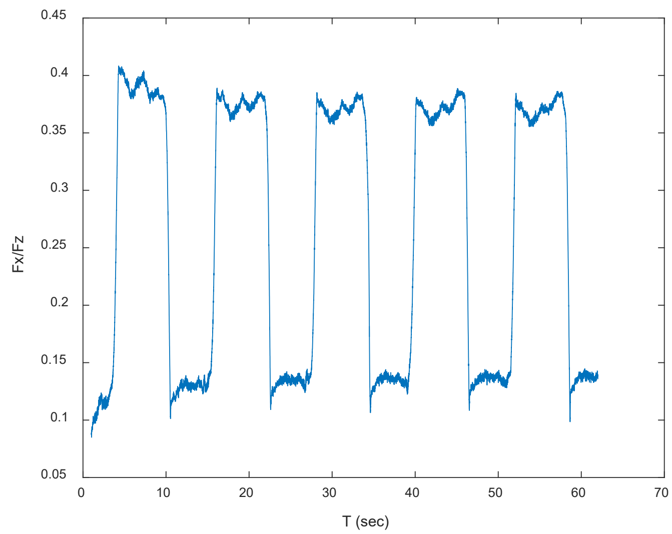

Fig. 3.8 Typical plot of pin tangential-to-normal force ratio as a function of time for an inter-particle friction test

To calculate the inter-particle COF, a force analysis for the two particles sliding against each other was performed using the free body diagrams shown in Fig. 3.9. The COF is found to be a function of the pin tangential force, the pin vertical force, and the contact angle. When the pin moves downward, the direction of the horizontal component of the normal contact force is the same as the direction of movement. However, when the pin moves upward, the direction of the horizontal component of the normal contact force is opposed to the direction of movement. This change in sign warrants the use of different equations for calculating the COF.

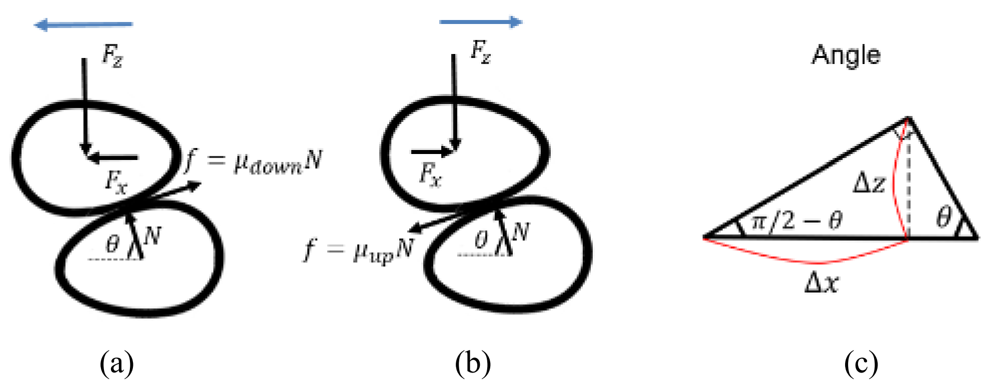

Fig. 3.9 Free body diagrams of two particles sliding against each other. (a) The upper particle moves downward; (b) The upper particle moves upward; (c) An illustration on the angle θ presented in (a) and (b)

When the upper particle moves downwards, the COF calculated from force balances is,

$$F_z = N sin\theta + \mu_{down} N cos\theta \tag{3.6}$$

$$F_x = \mu_{down} N sin\theta - N cos\theta \tag{3.7}$$

$$\mu_{down} = \frac{F_x sin\theta + F_z cos\theta}{F_z sin\theta - F_x cos\theta}. \tag{3.8}$$

When the upper particle moves upwards, the COF is,

$$F_z = N sin\theta - \mu_{up} N cos\theta \tag{3.9}$$

$$F_x = \mu_{up} N sin\theta + N cos\theta \tag{3.10}$$

$$\mu_{up} = \frac{F_x sin\theta - F_z cos\theta}{F_x cos\theta + F_z sin\theta} \tag{3.11}$$

where μ_{down} is the COF when the upper particle moves downwards, μ_{up} is the COF when the upper particle moves upwards, F_x is the horizontal force measured by the load cell, F_z is the vertical force measured by the load cell, *N* is the contact force normal to the inclined contact surface, *f* is the friction force parallel to the inclined contact surface, and θ is the contact angle, i.e., the angle between the normal contact force and the horizontal plane.

The contact angle changes as the relative position between the two particles changes. Since the vertical position of the upper kernel (*z*) and the horizontal position of the lower kernel (*x*) were recorded by the device at every time step, the contact angle could be calculated at all positions. An example of a *z* versus *x* plot is shown in Fig. 3.10(a), which shows the contact point trajectory. The contact angle at time *t*, can be estimated as (refer to Fig. 3.9(c)),

$$\theta(t) = \frac{\pi}{2} - arctan\left(\frac{\Delta z(t)}{\Delta x(t)}\right) \tag{3.12}$$

$$\Delta z(t) = |z(t + 0.5\ s) - z(t - 0.5\ s)| \tag{3.13}$$

$$\Delta x(t) = |x(t + 0.5\ s) - x(t - 0.5\ s)| \tag{3.14}$$

where $\theta(t)$ is the contact angle at time *t*, $z(t)$ is the vertical position of the upper kernel at time t, $x(t)$ is the horizontal position of the lower kernel at time *t*, $\Delta z(t)$ is the change in the vertical position of the upper kernel in a short time duration, and $\Delta x(t)$ is the change in the horizontal position of the lower kernel in a short time duration.

The central difference method was used when calculating $\Delta z(t)$ and $\Delta x(t)$. The time difference used to calculate the position change was chosen to be one second in order to generate smoothed data after the transformation by equations 3.8 and 3.11. An example of a contact angle versus time plot calculated using equations 3.12, 3.13, and 3.14 are shown in Fig. 3.10(b). Though the ratio of the change in the vertical/horizontal position in one second to the range of the vertical/horizontal position, i.e., $\frac{\Delta x(t)}{x_{max}-x_{min}}$ and $\frac{\Delta z(t)}{z_{max}-z_{min}}$, is relatively large (generally ranges from 0.25 to 0.3), equation 3.12 was able to give a good estimation of the contact angle when the rate of change in the contact angle is small. To exclude the timesteps where the rate of change in the contact angle is larger, a filter was applied to the data. After applying the filter, only the timesteps colored in red in Fig. 3.10(b) were kept. In addition, the sign of Δz(t) was used to determine whether the upward or downward condition was occurring, i.e., whether equation 3.8 should be used to calculate the COF or equation 3.11.

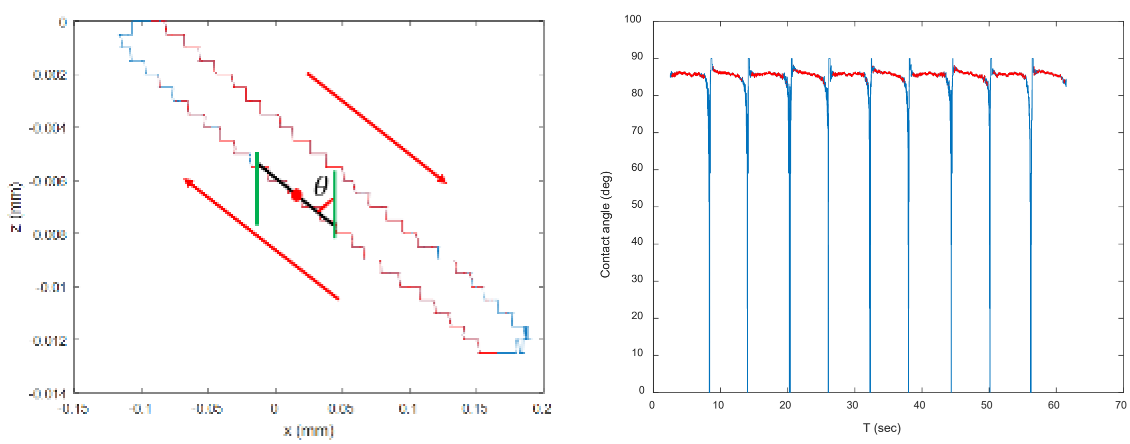

(a) (b)

Fig. 3.10 (a) Contact point trajectory of movement (clockwise motion); (b) Calculated contact angle as a function of time. The parts of the curve colored in red indicate the timesteps used for data analysis

A MATLAB script was developed to process the original data and calculate the dynamic COF. To validate the correctness of the script, a flat surface friction test was conducted before the inter-particle friction test. The flat surface friction test is a simplified case of the inter-particle friction test since a sliding particle on a flat surface has a constant contact angle θ. For the test, the forces were first measured for a steel sphere sliding against a flat steel surface parallel to the ground. Next, the flat steel surface was tilted slightly to form an angle less than 10° relative to the ground. The steel ball was tested on this tilted surface and the forces were measured and analyzed. For the case of the ball sliding against the surface parallel to the ground (condition *a*), the COF between the steel ball and the flat surface was calculated directly from the measured normal and tangential force (refer to eq. (5)). For the case of the ball sliding against the tilted surface (condition *b*), the COF was calculated using equations 3.8 and 3.11. The results of the two test conditions are shown in Fig. 3.10. The COF at condition *a* was 0.12, which is the average of COF values colored in red in Fig. 3.11(a). The COF at condition *b* was 0.10, which is the average of COF values colored in blue in Fig. 3.11(b). Though the relative error was 13%, the absolute difference between the two measurements is only 0.015. This test indicates that the COF value acquired using the force balance analysis gives a good estimation of the inter-particle COF.

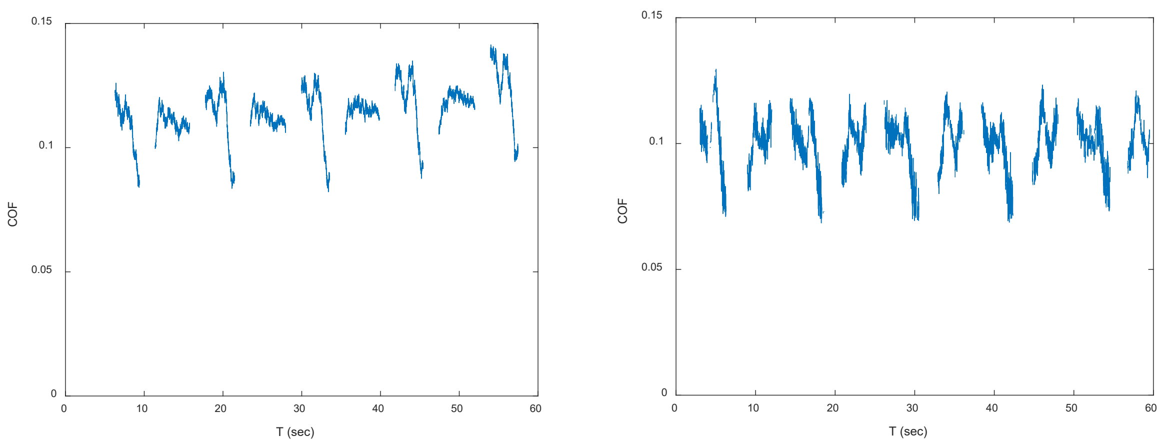

(a) (b)

Fig. 3.11 COF versus time plots of a steel sphere sliding on a flat steel surface. (a) Steel surface parallel to the ground; (b) A constant angle between the steel surface and the ground

Fig. 3.12 shows a typical COF versus time plot for contact between two corn kernels. The COF value of a test replicate was calculated by taking the average of the COF values at the selected time steps. The average values of the test replicates are presented in Table 3.4 with standard deviations. The dynamic COF of corn on corn is 0.09 ± 0.02 while the COF of wheat on wheat is 0.18 ± 0.04. The results are consistent with the findings obtained from the particle-wall friction test with corn having a lower value than wheat. This is consistent with the corn kernel having a smoother surface than the wheat kernel. It was found that the corn-corn COF has a smaller standard deviation than the wheat-wheat COF. This difference in standard deviation can be explained by the fact that the corn kernels have a relatively flatter contact surface, which provides more consistent measurements when compared with wheat kernels. No literature was found to report the values of inter-particle COF at the particle level for corn and wheat. Shear cell tests have been used to measure the bulk coefficient of internal friction of grain. Molenda and Horabik [3] measured the bulk coefficient of internal friction of corn to be 0.62 ± 0.01 and that of wheat to be 0.49 ± 0.01. The bulk coefficient of internal friction is much higher than the inter-particle COF because of the mechanical interlock between the particles that occurs during the shear cell test.

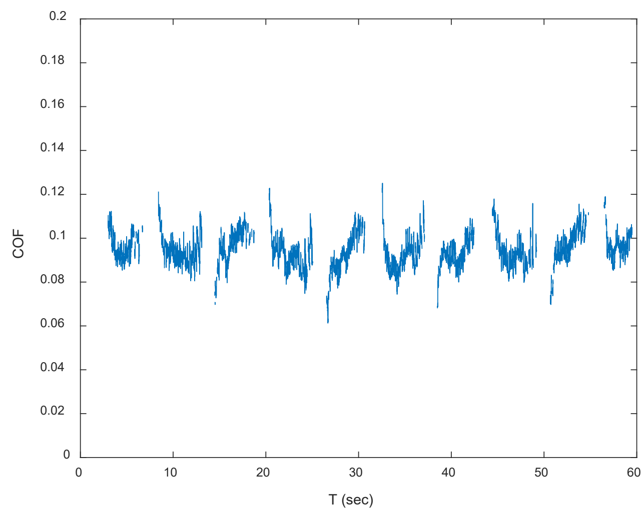

Fig. 3.12 Typical COF versus time plot for an inter-particle friction test for corn-on-corn

Table 3.4 Dynamic COFs measured for kernel on kernel contact

Type of grain kernel	Mean	Standard Deviation
Corn	0.09	0.02
Wheat	0.18	0.04

3.4 Summary

Particle-wall and inter-particle static and dynamic COFs of corn and wheat kernels were measured using a reciprocating-pin tribometer. The test setup and procedures were adjusted to accommodate testing of irregularly-shaped grain kernels. A force balance analysis was used to calculate the dynamic COFs when the contact surfaces were not aligned with the direction of movement of the bottom sample holder. The measured static COFs of corn-steel, corn-acrylic, wheat-steel, and wheat-acrylic were 0.24±0.05, 0.22±0.03, 0.32±0.02, and 0.29±0.03, respectively. The measured dynamic COFs of corn-steel, corn-acrylic, corn-corn, wheat-steel, wheat-acrylic, and wheat-wheat were 0.22±0.06, 0.16±0.01, 0.09±0.02, 0.30±0.02, 0.20±0.02, and 0.18±0.04, respectively.

This study demonstrates the feasibility of using a reciprocating-pin tribometer to measure particle-wall and inter-particle COFs of corn and wheat kernels. The test methodology developed could be used to measure the particle-wall and inter-particle COFs of other types of particulate materials with relatively smooth surfaces. Future research should investigate the effects of grain moisture content, contact location, and sliding orientation on the COFs. In particular, in these tests the contact location for corn was on the surface opposite to the germ side while for wheat the contact location was on the surface opposite to the crease side. It may be that different locations on the kernel, e.g., tip side, germ side, crown side, and crease side, have different COFs. In addition, scanning electron microscopy could be used to examine the kernel surface textures that may help to explain the influence of direction of travel on measurement of COFs with tribometer.

3.5 References

[1] Altuntas, E., & Demirtola, H. (2007). Effect of moisture content on physical properties of some grain legume seeds. *New Zealand Journal of Crop and Horticultural Science*, *35*(4), 423–433. doi:10.1080/01140670709510210

[2] Schwab, C. V., Ross, I. J., White, G. M., & Colliver, D. G. (1994). Wheat Loads and Vertical Pressure Distribution in a Full-scale Bin Part I - Filling. *Transactions of the ASAE*, *37*(5), 1613–1619. doi:10.13031/2013.28248

[3] Molenda, M., & Horabik, J. (2005). *Mechanical Properties of Granular Agro-Materials and Food Powders for Industrial Practice. Part I : Characterization of mechanical properties of particulate solids for storage and handling* (180 copies.). Lublin, Poland: Institute of Agrophysics PAS. doi:10.13140/2.1.2810.1447

[4] Horabik, J., & Molenda, M. (2016). Parameters and contact models for DEM simulations of agricultural granular materials: A review. *Biosystems Engineering*, *147*, 206–225. doi:10.1016/j.biosystemseng.2016.02.017

[5] Nimkar, P. M., & Chattopadhyay, P. K. (2001). Some physical properties of green gram. *Journal of Agricultural and Engineering Research*, *80*(2), 183–189. doi:10.1006/jaer.2000.0664

[6] Lawton, P. J. (1980). Coefficients of friction between cereal grain and various silo wall materials. *Journal of Agricultural Engineering Research*, *25*(1), 75–86. doi:10.1016/0021-8634(80)90049-9

[7] Brubaker, J. E., & Pos, J. (1965). Determining Static Coefficients of Friction of Grains on Structural Surfaces. *Transactions of the ASAE*, *8*(1), 53–55. Retrieved from https://elibrary.asabe.org/azdez.asp?AID=40423&T=2

[8] Özarslan, C. (2002). Physical properties of cotton seed. *Biosystems Engineering*, *83*(2), 169–174. doi:10.1006/bioe.2002.0105

[9] Suthar, S. H., & Das, S. K. (1996). Some physical properties of Karingda [Citrullus lanatus (thumb) mansf] seeds. *Journal of Agricultural and Engineering Research*, *65*(1), 15–22. doi:10.1006/jaer.1996.0075

[10] Reza, A. (2010). Moisture-Dependent Physical Properties of Sunflower Seed (SHF8190). *Modern Applied Science*, *4*(7), 135–143. doi:10.5539/mas.v4n7p135

[11] Shepherd, H., & Bhardwaj, R. K. (1986). Moisture-dependent physical properties of pigeon pea. *Journal of Agricultural Engineering Research*, *35*(4), 227–234. doi:10.1016/S0021-8634(86)80060-9

[12] Snyder, L. H., Roller, W. L., & Hall, G. E. (1967). Coefficients of Kinetic Friction of Wheat on Various Metal Surfaces. *Transactions of the ASAE*, *10*(3), 411–413. Retrieved from https://elibrary.asabe.org/azdez.asp?AID=39686&t=2

[13] Corrêa, P. C., Schwanz Da Silva, F., Jaren, C., Afonso Ju´nior, P. C., & Arana, I. (2007). Physical and mechanical properties in rice processing. *Journal of Food Engineering*, *79*(1), 137–142. doi:10.1016/j.jfoodeng.2006.01.037

[14] Tsang-Mui-Chung, M., Verma, L. R., & Wright, M. E. (1984). A Device for Friction Measurement of Grains. *Transactions of the ASAE*, *27*(6), 1938–1944.

[15] Kibar, H., & Öztürk, T. (2008). Physical and mechanical properties of soybean. *International Agrophysics*, *22*(3), 239–244.

[16] Tarighi, J., Mahmoudi, A., & Alavi, N. (2011). Some mechanical and physical properties of corn seed (Var. DCC 370). *African Journal of Agricultural Research*, *6*(16), 3691–3699. doi:10.5897/AJAR10.521

[17] Visvanathan, R., Palanisamy, P. T., Gothandapani, L., & Sreenarayanan, V. V. (1996). Physical Properties of Neem Nut. *Journal of Agricultural Engineering Research*, *63*(1), 19–25. doi:10.1006/jaer.1996.0003

[18] Dutta, S. K., Nema, V. K., & Bhardwaj, R. K. (1988). Physical properties of gram. *Journal of Agricultural Engineering Research*, *39*(4), 259–268. doi:10.1016/0021-8634(88)90147-3

[19] Fraser, B. M., Verma, S. S., & Muir, W. E. (1978). Some physical properties of fababeans. *Journal of Agricultural Engineering Research*, *23*(1), 53–57. doi:10.1016/0021-8634(78)90079-3

[20] Çarman, K. (1996). Some physical properties of lentil seeds. *Journal of Agricultural and Engineering Research*, *63*(2), 87–92. doi:10.1006/jaer.1996.0010

[21] Amin, M. N., Ahammed, S., Roy, K. C., & Hossain, M. A. (2005). Coefficient of Friction of Pulse Grains on Various Surfaces at Different Moisture Content. *International Journal of Food Properties*, *8*(1), 61–67. doi:10.1081/JFP-200048092

[22] Chung, J. H., & Verma, L. R. (1989). Determination of friction coefficients of beans and peanuts. *Transactions of the ASAE*, *32*(2), 745–750. doi:10.13031/2013.31064

[23] Gupta, R. K., & Das, S. K. (1997). Physical properties of sunflower seeds. *Journal of Agricultural and Engineering Research*, *66*(1), 1–8. doi:10.1006/jaer.1996.0111

[24] Bickert, W. G., & Buelow, F. H. (1966). Kinetic Friction of Grains on Surfaces. *Transactions of the ASAE*, *9*(1), 129–131. Retrieved from https://elibrary.asabe.org/azdez.asp?search=0&JID=3&AID=39897&CID=t1966&v=9&i=1&T=2

[25] Baryeh, E. A. (2002). Physical properties of millet. *Journal of Food Engineering*, *51*(1), 39–46. Retrieved from www.elsevier.com/locate/jfoodeng

[26] Singh, K. K., & Goswami, T. K. (1998). Mechanical properties of cumin seed (Cuminum cyminum Linn.) under compressive loading. *Journal of Food Engineering*, *36*(3), 311–321. doi:10.1016/S0260-8774(98)00056-9

[27] Sahoo, P. K., & Srivastava, A. P. (2002). Physical properties of okra seed. *Biosystems Engineering*, *83*(4), 441–448. doi:10.1006/bioe.2002.0129

[28] Altuntas, E., & Özkan, Y. (2008). Physical and mechanical properties of some walnut (Juglans regia L.) cultivars. *International Journal of Food Engineering*, *4*(4), Article 10. doi:10.2202/1556-3758.1349

[29] Ogut, H. (1998). Some Physical Properties of White Lupin. *Journal of Agricultural Engineering Research*, *69*(3), 273–277. doi:https://doi.org/10.1006/jaer.1997.0252

[30] Tarighi, J., Mohtasebi, S. S., Mahmoudi, A., Rastilantie, M.-, & Mahmoodi, A. (2005). Effect of moisture content on some physical properties of safflower (var. Darab) seeds. *Agriculture & Environment*, *8*(4), 602–606.

[31] Sacilik, K., Öztürk, R., & Keskin, R. (2003). Some Physical Properties of Hemp Seed. *Biosystems Engineering*, *86*(2), 191–198. doi:10.1016/S1537-5110(03)00130-2

[32] Kasap, A., & Altuntas, E. (2006). Physical properties of monogerm sugarbeet (Befa vulgaris var. altissima) seeds. *New Zealand Journal of Crop and Horticultural Science*, *34*(4), 311–318. doi:10.1080/01140671.2006.9514421

[33] Araghi, H. A., Sadeghi, M., & Hemmat, A. (2010). Physical properties of two rough rice varieties affected by moisture content. *International Agrophysics*, *24*(2), 205–207. Retrieved from www.international-agrophysics.org

[34] Kaliniewicz, Z. (2013). Analysis of frictional properties of cereal seeds. *African Journal of Agricultural Research*, *8*(45), 5611–5621. doi:10.5897/AJAR2013.7361

[35] González-Montellano, C., Fuentes, J. M., Ayuga-Téllez, E., & Ayuga, F. (2012). Determination of the mechanical properties of maize grains and olives required for use in DEM simulations. In *2011 ASABE Annual International Meeting* (pp. 553–562). doi:10.1016/j.jfoodeng.2012.03.017

[36] Kingsly, A. R. P., Singh, D. B., Manikantan, M. R., & Jain, R. K. (2006). Moisture dependent physical properties of dried pomegranate seeds (Anardana). *Journal of Food Engineering*, *75*(4), 492–496. doi:10.1016/j.jfoodeng.2005.04.033

[37] European Standard. (2006). *Eurocode 1 - Actions on structures - Part 4: Silos and tanks*. Retrieved from https://www.phd.eng.br/wp-content/uploads/2015/12/en.1991.4.2006.pdf

[38] Rusinek, R., & Molenda, M. (2007). Static and kinetic friction of rapeseed. *Research in Agricultural Engineering*, *53*(1), 14–19.

[39] Kibar, H., & Esen, B. (2010). The effect of moisture content on physical and mechanical properties of rice (Oryza sativa L.). *Spanish Journal of Agricultural Research*, *8*(3), 741–749.

[40] Horabik, & Molenda, M. (1988). Force and contact area of wheat grain in friction. *Journal of Agricultural Engineering Research*, *41*(1), 33–42. doi:10.1016/0021-8634(88)90201-6

[41] ASTM. (2018). *G115-10: Standard Guide for Measuring and Reporting Friction Coefficients*. West Conshohocken, PA: ASTM Int. doi:10.1520/G0115-10R18

[42] Eyre, T. S., & Maynard, D. (1971). Surface aspects of unlubricated metal-to-metal wear. *Wear*, *18*(4), 301–310. doi:10.1016/0043-1648(71)90073-1

[43] Andersson, P. (1992). Water-lubricated pin-on-disc tests with ceramics. *Wear*, *154*(1), 37–47. Retrieved from https://ac.els-cdn.com/004316489290241Y/1-s2.0-004316489290241Y-main.pdf?_tid=858db15f-9977-467d-aa84-076ca551bb13&acdnat=1551064405_542e851f45e89bdae2dd8e0bed45cce6

[44] ASABE Standard. (2017). *S352.2: Moisture Measurement-Unground Grain and Seeds*. St. Joseph, MI: ASABE. Retrieved from https://elibrary.asabe.org/azdez.asp?JID=2&AID=24272&CID=s2000&T=2

[45] ASTM. (2010). *G133−05: Standard Test Method for Linearly Reciprocating Ball-on-Flat Sliding Wear*. West Conshohocken, PA: ASTM Int. doi:10.1520/G0133-05R10.2

[46] Hancock, B. C., Mojica, N., St.John-Green, K., Elliott, J. A., & Bharadwaj, R. (2010). An investigation into the kinetic (sliding) friction of some tablets and capsules. *International Journal of Pharmaceutics*, *384*(1–2), 39–45. doi:10.1016/j.ijpharm.2009.09.038

[47] Bucklin, R. A., Thompson, S. A., Ross, I. J., & Bigss, R. H. (1993). Apparent dynamic coefficient of friction of corn on galvanized steel bin wall material. *Transactions of the ASAE*, *36*(6), 1915–1918. Retrieved from http://cat.inist.fr/?aModele=afficheN&cpsidt=3966529

[48] Isik, E., & Izli, N. (2007). Moisture Dependent Physical and Mechanical Properties of Dent Corn (Zea mays var. indentata Sturt.) Seeds (Ada-523). *American Journal of Food Technology*, *2*(5), 342–353.

[49] Seifi, M. R., & Alimardani, R. (2014). The Moisture Content Effect on Some Physical and Mechanical Properties of Corn (Sc 704). *Journal of Agricultural Science*, *2*(4), 125–134. doi:10.5539/jas.v2n4p125

[50] Karimi, M., Kheiralipour, K., Tabatabaeefar, A., Khoubakht, G. M., Naderi, M., & Heidarbeigi, K. (2009). The Effect of Moisture Content on Physical Properties of Wheat. *Pakistan Journal of Nutrition*, *8*(1), 90–95. doi:10.3923/pjn.2009.90.95

[51] Zaalouk, A. K., & Zabady, F. I. (2009). Effect of Moisture Content on Angle of Repose and Friction Coefficient of Wheat Grain. *Misr Journal for Agricultural Engineering*, *26*(1), 418–427.

[52] Kalkan, F., & Kara, M. (2011). Handling, frictional and technological properties of wheat as affected by moisture content and cultivar. *Powder Technology*, *213*(1), 116–122. doi:10.1016/j.powtec.2011.07.015

[53] Shafaei, S. M., & Kamgar, S. (2017). A comprehensive investigation on static and dynamic friction coefficients of wheat grain with the adoption of statistical analysis. *Journal of Advanced Research*, *8*(4), 351–361. doi:10.1016/j.jare.2017.04.003

[54] Senetakis, K., & Coop, M. (2014). The development of a new micro-mechanical inter-particle loading apparatus. *Geotechnical Testing Journal*, *37*(6), 1028–1039. doi:10.1520/GTJ20120187

4. DETERMINATION OF THE MATERIAL AND INTERACTION PROPERTIES OF CORN AND WHEAT KERNELS FOR DEM SIMULATIONS

4.1 Introduction and Background

DEM developed by Cundall and Strack [1] is a predictive tool to model movement of granular material. This method has been widely used in the mineral, pharmaceutical, and chemical industries. In recent years, an increasing number of studies have applied DEM to simulate grain motion in agricultural production, processing and transportation, e.g. sowing [2], harvesting [3], conveying [4], milling [5], drying [6], and storage [7]. One critical step when modeling grain with DEM is accurately determining the model input parameters, i.e. the material and interaction properties of the grain kernels, since the simulation will be greatly influenced by these parameters. However, there are no standard procedures to determine these parameters and various approaches have been proposed [8]. The common methods of parameter determination can be summarized as follows, 1. using values reported in the literature; 2. directly measuring the single-particle properties; 3 calibrating one or several parameters with bulk material test(s), i.e. changing the model parameters iteratively until the simulated bulk response of the particles matches the experimental result [8]. Each approach has its strengths and weaknesses, and selection of method depended on the material property to be measured and the application.

Material and interaction properties of different types of grain have been studied and measured by numerous studies before the development of DEM. Recently, two review articles [9, 10] have summarized the material and interaction properties of grains reported in the literature specifically for DEM simulations. However, it is worth noting that the literature values can only be used as a rough estimation of the actual values. This is because the moisture content, variety, and other conditions of the grain, which are hardly the same as the values in the published study, can drastically affect grain properties. Thus, direct measurement of properties is preferred over using literature values, though it can be time-consuming to conduct tests. Nevertheless, not all the properties can be easily and accurately measured experimentally. It is still a challenging task to estimate the particle-particle interaction properties for DEM simulations, such as the sliding COF, rolling COF, COR, and cohesion, due to the irregular shape of the kernel and the heterogeneity of the biological materials. These hard-to-measure parameters were commonly acquired through the bulk calibration approach [4, 11]. However, one problem of this approach is that the parameters may be calibrated to the calibration experiment instead of the material [12], which could result in inaccurate predictions of the bulk behavior of the material [13].

To accurately and efficiently determine the parameters for DEM, a strategy was developed using a combination of the above-mentioned approaches [14, 15]. The general procedure is to first identify the parameters that have a significant effect on the simulation result based on experience or sensitivity analysis. Then, these critical parameters are either measured or calibrated. The parameters that are not critical can be estimated based on the values reported in literature. Before using the adapted parameters in complex large-scale applications, several simple small-scale experiments should be conducted and modeled. The parameters are considered to be estimated properly if the simulation models the bulk behavior of the material accurately.

This chapter aims to determine the material and interaction properties of corn and wheat kernels for DEM simulation using the strategy as described in the previous paragraph. The Young's modulus, Poisson's ratio, and inter-particle coefficient of restitution (COR) values were adopted from literature. The particle shape, mass, particle-wall, and inter-particle COFs were experimentally measured. The particle-wall COR was estimated using the calibration method. To validate the parameter values, the measured parameters were used to model the bulk density test and the angle of repose test.

4.2 Materials and Methods

4.2.1 Simulation Software and Contact Model

The software used to conduct the DEM simulation in this study was EDEM 2019 (DEM Solutions Ltd, Edinburgh, UK). The Hertz-Mindlin no-slip model [16] was used as the contact force model for all the simulations, which is shown schematically in Fig. 4.1.

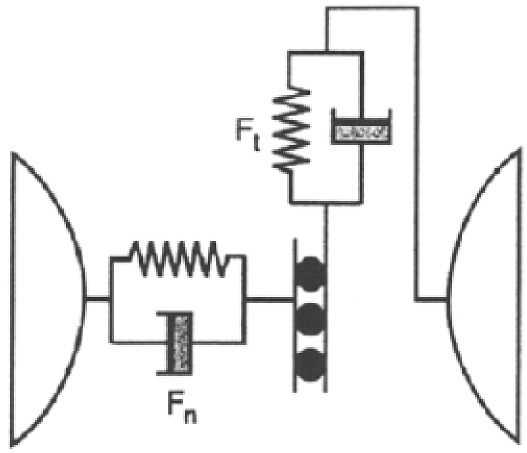

Fig. 4.1 Schematic of Hertz-Mindlin contact model [17]

The normal contact between two contact elements is simulated as a non-linearly damped Hertzian spring. The normal contact force, F_n, is the sum of the normal spring force and normal damping force given by,

$$F_n = k_n \delta_n^{3/2} + c_n \delta_n^{1/4} v_n^{rel} \tag{4.1}$$

where k_n is normal spring stiffness, c_n is the normal damping coefficient, δ_n is the normal overlap between two contact elements, and v_n^{rel} is the normal relative velocity between two contact elements.

Similar to the normal contact, the tangential contact between two contact elements is also modeled as a non-linearly damped spring with a different spring stiffness and a damping coefficient. Nevertheless, the tangential contact force is limited by Coulomb's law of friction, i.e. the tangential force would not be larger than the friction force predicted by Coulomb's low. The tangential contact force, F_t, is calculated as,

$$F_t = min\{k_t \delta_n^{1/2} \delta_t + c_t \delta_n^{1/4} v_t^{rel}, \mu_s F_n\} \tag{4.2}$$

where k_t is tangential spring stiffness, c_t is the tangential damping coefficient, δ_t is the tangential overlap between two contact elements, v_t^{rel} is the tangential relative velocity between two contact elements, and μ_s is the sliding COF between two contact elements.

The spring stiffness and damping coefficients are functions of material properties, which are defined in Table 4.1.

Table 4.1 Spring stiffness and damping coefficients in Hertz-Mindlin contact model

	Normal component	**Tangential component**
Spring stiffness	$k_n = \frac{4}{3}E^*\sqrt{R^*}$	$k_t = 8G^*\sqrt{R^*}$
Damping coefficient	$c_n = \frac{\ln e}{\sqrt{\ln^2 e + \pi^2}}\sqrt{5m^* k_n}$	$c_t = \frac{\ln e}{\sqrt{\ln^2 e + \pi^2}}\sqrt{\frac{10}{3}m^* k_t}$

R^*: equivalent radius, $\frac{1}{R^*} = \frac{1}{R_i} + \frac{1}{R_j}$

R_i, R_j: Radius of contact components

m^*: equivalent mass, $\frac{1}{m^*} = \frac{1}{m_i} + \frac{1}{m_j}$

m_i, m_j: mass of contact components

E^*: equivalent Young's modulus, $\frac{1}{E^*} = \frac{(1-v_i^2)}{E_i} + \frac{(1-v_i^2)}{E_j}$

E_i, E_j: Young's modulus of contact components

v_i, v_j: Poisson's ratio of contact components

G^*: equivalent shear modulus, $\frac{1}{G^*} = \frac{(2-v_i)}{G_i} + \frac{(2-v_j)}{G_j}$

G_i, G_j: shear modulus of contact components

e: coefficient of restitution

4.2.2 Test Material

The corn and wheat samples used in this study were collected from a farm located near Covington, Indiana. The moisture content of the samples determined using the whole kernel oven method [18] were 14.7% and 13.9% wet basis for corn and wheat, respectively. Sieves, 16/64-inch round-hole sieve for corn and 0.0064×3/8-inch oblong-hole sieve for wheat, were used to separate out broken kernels and fine material. Foreign material and broken kernels with sizes similar to the size of grain kernels were manually separated from the sieved sample. Low carbon steel and acrylic were selected as the representative equipment materials since they are common in agricultural production and laboratory testing systems. The materials were purchased in the form of flat sheets and then machined into circular disks.

4.2.3 Material and Interaction Properties Determination

The material and interaction properties that are considered to have a critical effect on particle flow behavior were experimentally measured. The measured or calibrated properties included the particle shape, mass, COF, and COR. Previous studies indicated that Young's modulus had a minor effect on the flow behavior when the material was not highly compressed [19]. In those cases, Young's modulus can be reduced to speed up the simulations [20, 21]. Literature values were used for the Young's modulus and Poisson's ratio. The rolling COF is often used as a calibrated parameter to account for the rolling resistance when the particle is modeled as a single sphere. In the current study, the particle shape was modeled as glued-sphere clumps, thus the rolling COR was set to zero in the simulations.

4.2.3.1 Particle Shape and Mass

To acquire an accurate representation of the particle shape, an X-ray micro-CT scanner was used to generate three-dimensional (3D) models of the grain kernels. A Skyscan 1272 (Bruker, Billerica, MA), as shown in Fig. 4.2, was used to scan the test samples. The device uses X-rays to produce tomography projection images by scanning the object at different angles and then reconstructing a 3D model based on the images with the aid of computer programs. Though the resolution of the scanner can reach 0.4 μm, a resolution of 21.7 μm was used as it was high enough to generate an accurate shape representation of the kernels. Based on the 3D model output from the scanner, an approximate shape model using spheres was generated by the Automatic Sphere-clump Generator (ASG) software (Cogency, Cape Town, South Africa). An optimization algorithm was implemented in the software to minimize the distance between the surface of the approximate shape model and the surface of the original 3D model [22]. The optimized diameters and relative positions of the spheres were input into the DEM simulation to construct the glued-sphere clumps.

For each type of grain, six kernels were randomly selected from the sample. Before scanning, the mass of each kernel was measured with an electronic balance. The kernels were then scanned, and the corresponding glued-sphere clumps were created in the DEM simulation. The mass of each glued-sphere clump was manually input into the simulation based on the measurement. In most of the previous studies, the mass of the particle was calculated based on the density of the particle. However, as the kernel mass was a direct input parameter, it was not necessary to measure the particle density for the current study.

Fig. 4.2 High-resolution 3D X-ray micro-CT scanner: Bruker Skyscan 1272

4.2.3.2 Coefficient of Friction

The particle-wall (corn-steel, corn-acrylic, wheat-steel, and wheat-acrylic) and inter-particle (corn-corn and wheat-wheat) COFs were measured using a reciprocating pin tribometer (Bruker UMT TriboLab, Billerica, MA). A detailed description of the test setup and procedure can be found in section 3.2. In this section, only a brief introduction of the test setup and procedure is given. The device setup was adapted to make measurements for irregular shape particles. The modified test setup consists of five main components, i.e. the top sample holder with the top sample, the driving units, the bottom sample holder with the bottom sample, the load cell, and the data acquisition system (DAS). Photographs and schematics of the particle-wall and inter-particle friction test setups are shown in Fig. 4.3.

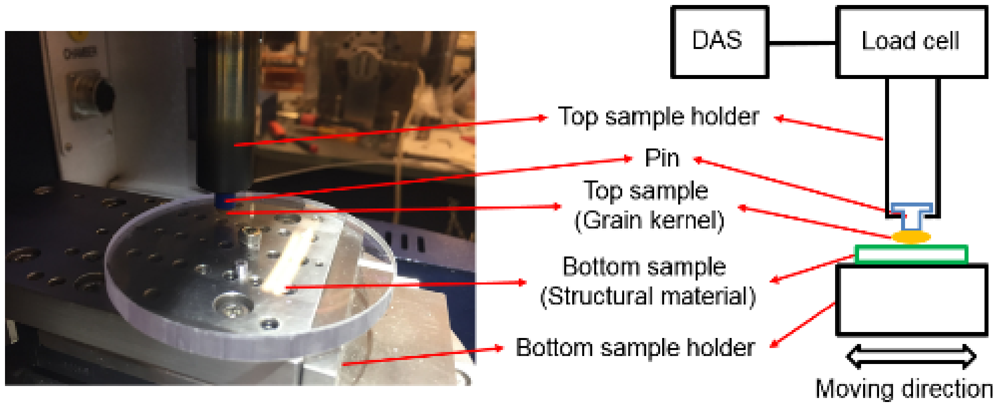

(a)

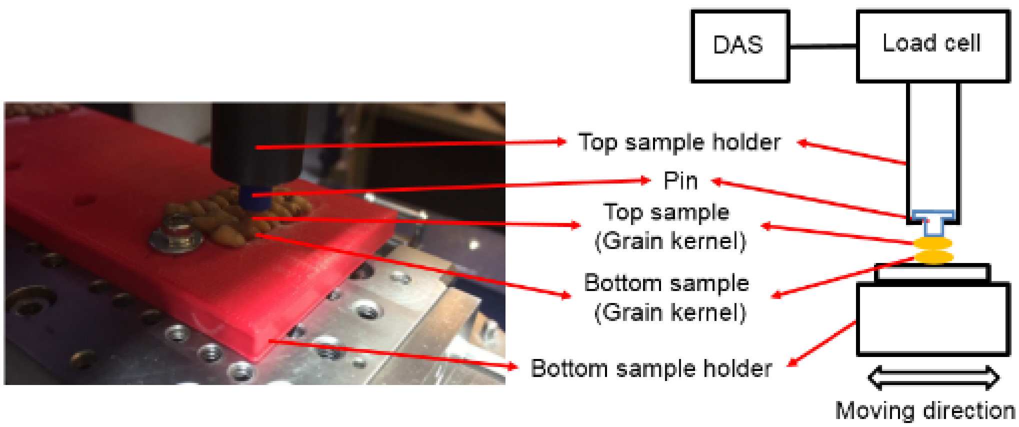

(b)

Fig. 4.3 Friction test setups. (a) Particle-wall; (b) Inter-particle. Photographs are shown on the left, and schematic are shown on the right

The measurement procedure was adapted from the standard test procedure developed by ASTM [23]. The top and bottom samples were first cleaned with isopropyl alcohol and lens cleaning tissues and then fixed on the sample holders. The top sample was lowered vertically till it came in contact with the bottom sample. The motion of lowering stopped when the normal force measured by the load cell reached a specified force level. The bottom sample was then moved horizontally by the driving unit at a specified speed level. During the test, the normal force (F_z) and tangential force (F_x) applied to the top sample were measured by the load cell and recorded by the DAS. For particle-wall measurements, the COF (μ) can be calculated as,

$$\mu = \frac{F_x}{F_z} \tag{4.3}$$

For the inter-particle measurements, because the kernels are not flat, a coordinate transformation was required when calculating the COF. The procedure used for the transformation and the data analysis process are discussed in detail in section 3.3.

4.2.3.3 Coefficient of Restitution

The particle-wall COR was calibrated using a test setup designed by the author, as shown in Fig. 4.4(a). The setup consists of three parts, a releasing box, a receiving box, and an impact plate. The advantage of this setup is that it is simple and its main components can be easily 3D printed. The impact plate was fabricated from the test material, either steel or acrylic. The receiving box was divided into a certain number of bins by inserting cardboard partitions into the slots provided in the wall. The size of the bin can be adjusted by changing the position of the partitions to accommodate the size of the grain kernels being tested.

For each type of grain, 300 kernels were randomly selected and dropped from the releasing box one at a time. The height of the releasing box was adjusted so that the speed of the kernel when it collided with the surface was 1.3 m/s. The kernels were placed in the releasing box in random orientation and were slowly pushed toward the bottom opening of the releasing box one by one. After bouncing off of the impact surface, the kernels were collected in separate bins of the receiving box. The number of kernels in each bin was counted to form a frequency distribution of number of kernels in different bins. To replicate the experimental test setup in DEM simulations, the dimension of the receiving box, the relative position of the releasing box, impact surface, and releasing box were measured with a digital caliper. The angle of the impact surface relative to the ground was measured with a protractor. The DEM simulation was set up as shown in Fig. 4.4(b).

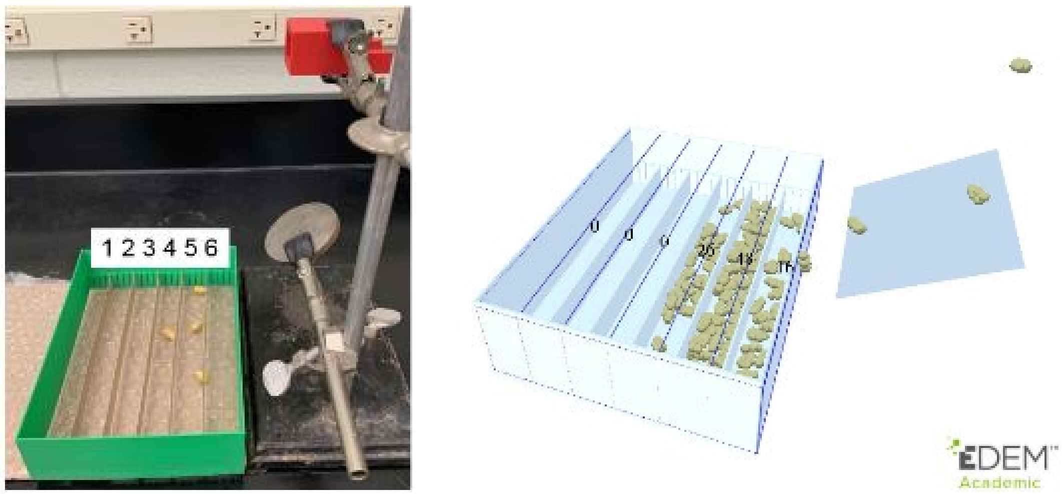

(a) (b)

Fig. 4.4 Particle-wall COR test setup. (a) Experiment setup and (b) simulation setup

To quantitatively compare the experimental results with the simulation results, an average bin number was calculated. The average bin number ($\bar{\imath}$) is defined as follow:

$$\bar{\imath} = \frac{1}{N_{total}} \sum_{i=1}^{n} (i \times N_i) \tag{4.4}$$

where i is the bin number, n is the total number of the bins, N_i is the number of kernels that fell into bin i, and N_{total} is the total number of kernels used in the test. As illustrated in Fig. 4.4(a), the bins in the receiving box were labeled as one to n from left to right. To compare the variability of the data, the standard deviation of the bin numbers (s_i) was also calculated as follows,

$$s_i = \sqrt{\frac{1}{N_{total} - 1} \sum_{i=1}^{n} N_i \cdot (i - \bar{\imath})^2} \tag{4.5}$$

The material and interaction properties used in the simulation except the particle-wall COR were either measured directly with the methods described in sections 3.2.1. and 3.2.2. or acquired from the literature. Simulations with different values of particle-wall COR were run and the average bin numbers were recorded. The COR value that minimizes the difference between the average bin numbers of the simulation and the experiment was determined.

4.2.4 Bulk Material Tests

The bulk behavior of the grains was studied with the bulk density test and the angle of repose test [9, 12]. The test setups and procedures were replicated in DEM simulations. The input parameters used in DEM simulations were determined using the methods reported in section 3.2. The accuracy of the material and interaction properties measurements was evaluated based on the relative difference between the simulation results and experimental measurements.

4.2.4.1 Bulk Density

The bulk density of the grain was measured using a Winchester cup setup (Seedburo Equipment Co., Des Plaines, IL) as shown in Fig. 4.5(a). Grain was placed in a funnel which has a slide gate at the bottom. The gate was opened, and the grain was poured into a cup of known volume (one-pint dry measure, 0.00057 m^3). A sufficient amount of grain (around 600 gram) was placed in the funnel to ensure the cup overflowed. Grain above the cup was leveled off using a wooden striker. The striker was moved in a zig-zag motion when sweeping over the cup to avoid compaction of grain kernels. The edge of the striker always made contact with the top edge of the cup when it was moved across the top of the cup. The mass of the empty cup (m_0) and the mass of the cup with the grain (m_1) were measured with an electronic balance. The bulk density ρ_b was determined by dividing the mass of the grain in the cup ($m_1 - m_0$) by the volume of the cup (V),

$$\rho_b = \frac{m_1 - m_0}{V} \tag{4.6}$$

This test was repeated three times for both corn and wheat samples.

The test setup, e.g. the height of the hopper and the sample size, can affect the measurement [24]. Thus, it is important to keep the experiment and simulation test setup the same to have comparable results. With the same dimension and relative position of the funnel and cup, the test setup was reproduced in a DEM simulation, as shown in Fig. 4.5(b). The motion of the slide gate and wooden striker in the simulation also mimicked the procedure used in the experiment. At the end of the simulation, the bulk density of the grain was calculated directly by the software.

(a)

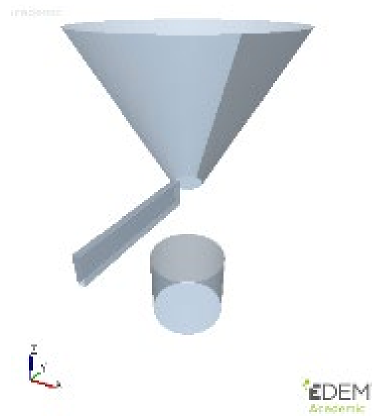

(b)

Fig. 4.5 Bulk density test setup. (a) Experiment setup and (b) simulation setup

4.2.4.2 Angle of Repose

The angle of repose test was set up with a pan placed under a funnel (Fig. 4.6(a)). The position of the funnel outlet was adjusted right above the center of the pan. A 1200-gram grain sample was poured into the funnel which had the bottom outlet closed. The outlet was opened, and the grain was discharged from the funnel. Sufficient grain was used to fill the pan and have the pan overflow. After the funnel fully discharged, a pile of grain was formed above the pan. A camera was used to take a picture of the grain pile. To have a correct representation of the pile shape and size in the picture, the camera was placed with its short axis perpendicular to the top of the lab bench at the same level as the pan. The test was repeated three times for both corn and wheat samples. The same test setup and procedure were replicated in a DEM simulation. A screenshot of the pile with the view orientation parallel to the X-Z plane was taken at the last time step of the simulation. The outlines of the pile in the images were identified by processing the images with MATLAB. The qualitative comparison was made between the outlines of the piles acquired from the experiment and simulation. The height of the pile at the middle of the pan was measured based on the outline extracted from the original image. A quantitative comparison was made between the ratio of the pile height to the pan radius acquired from the experiment and simulation.

(a) (b)

Fig. 4.6 Angle of repose test setup. (a) Experiment setup and (b) simulation setup

4.3 Results and Discussion

4.3.1 Material and Interaction Properties Determination

4.3.1.1 Particle Shape

Fig. 4.7(a) shows one of the 3D mesh models output by the X-ray micro-CT scanner in stereolithography (STL) format. Based on the 3D mesh models, ASG software was used to generate the glued-sphere clumps. As shown in Fig. 4.7(b), the glued-sphere clump gives a more accurate shape representation of the original particle when a greater number of spheres is used. However, the trade-off for using a greater number of spheres is that the computational time increases accordingly. A previous study compared the results of simulating the angle of repose test and rotating drum test of iron ore pellets with single-sphere and glued-sphere clumps [14]. It was found that simulating particles with glued-sphere clumps resulted in a better agreement between experimental and simulation results. Though increasing the number of spheres gives a more detailed description of the particle shape, it does not necessarily improve the accuracy of the simulation [25]. As the number of spheres, the simulation accuracy tends to converge to a certain level [26]. It was reported that a small number of spheres, i.e. 5 spheres, can provide reasonable results when simulating corn kernels in a rotary seed coater [27]. Another study stated that the angle of repose and bulk density of corn kernels were accurately simulated when 16 spheres were used [26].

ASG software evaluates the accuracy of the glued-sphere shape representation based on the volume error and average mass distribution error along the principal axes (EIT) error. A detailed description of the error calculation can be found in Price et al. [22] and Lien and Kajiya [28]. Fig. 4.8 is a plot of the volume error and EIT error versus the number of spheres when modeling a selected corn kernel 3D mesh with a glued-sphere clump. The plot indicates that both errors reach low values when the number of spheres is greater than five. Thus, four to five spheres were used to model the shape of the grain kernels. In this way, reasonable shape representations were acquired and the computation times of the simulations were minimized. All twelve glued-sphere clumps used in the DEM simulations are shown in Fig. 4.9. Table 4.2 reports the mean and standard deviation of the error between the 3D mesh models and the glued-sphere clumps. For both corn and wheat kernels, the mean volume errors are less than 3%, while the mean EIT errors are less than 8%. The errors of wheat kernels are greater than the corresponding errors of corn kernels because it is challenging to simultaneously depict both the crease on the one side of the wheat kernel and the smooth surface on the opposite side with a small number of spheres.

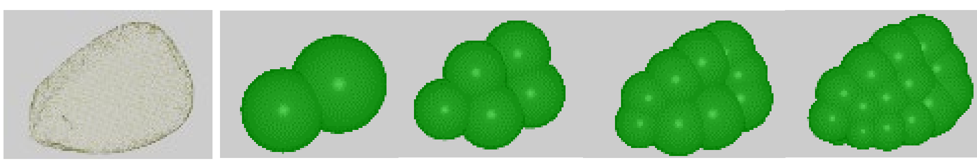

(a) (b)

Fig. 4.7 An example of (a) a 3D mesh model generated by the X-ray micro-CT scanner, (b) glued-sphere clumps generated by ASG software based on the 3D mesh model. From left to right: 2 spheres; 5 spheres; 10 spheres; 20 spheres

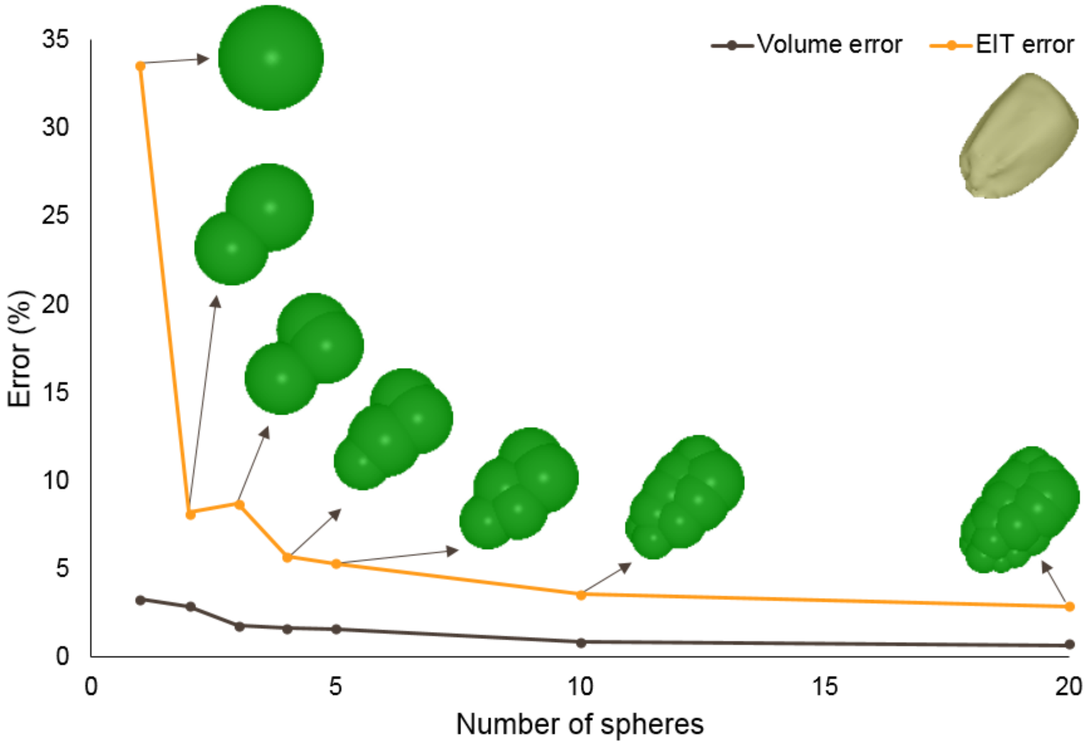

Fig. 4.8 Volume error and EIT error versus the number of spheres in the clump. An image of the 3D model of the kernel is shown in the upper right corner

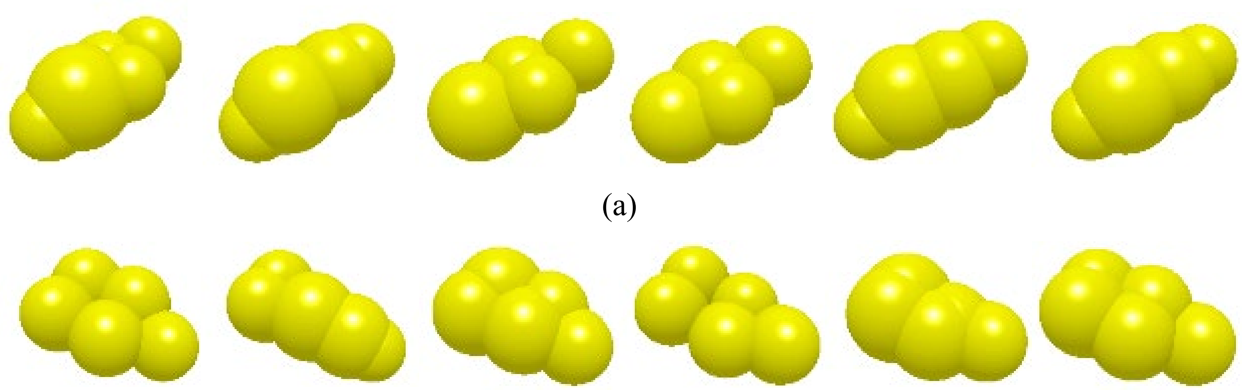

(a)

(b)

Fig. 4.9 Glued-sphere clumps used in DEM simulations. (a) Wheat kernels and (b) corn kernels

Table 4.2 Volume and EIT errors between the 3D mesh models and the glued-sphere clumps

	Volume error (%)[a]	EIT error (%)[a]
Wheat	2.62 (0.36)	7.98 (0.56)
Corn	1.81 (1.19)	5.30 (1.42)

[a] Values in parentheses are standard deviations.

4.3.1.2 Coefficient of Friction

The static COFs of corn-steel, corn-acrylic, wheat-steel, and wheat-acrylic and the dynamic COFs of corn-steel, corn-acrylic, corn-corn, wheat-steel, wheat-acrylic, and wheat-wheat were measured using a reciprocating pin tribometer. A detailed description of the data analysis process is given in section 3.3. In this section, only a summary of the results is presented. Fig. 4.10 shows a typical COF versus time plot from a particle-wall friction test. The static COF was calculated by averaging the peak values circled in blue in Fig. 4.10(a), which represent the COF values when the samples just start to move against each other. The dynamic COF was calculated by averaging the values identified in yellow in Fig. 4.10(a), which represent the COF values during steady-state sliding. The mean and standard deviation of the particle-wall static and dynamic COFs and the inter-particle dynamic COFs are reported in Table 4.3. The values of particle-wall and inter-particle dynamic COFs were used as input parameters for the bulk material test simulations.

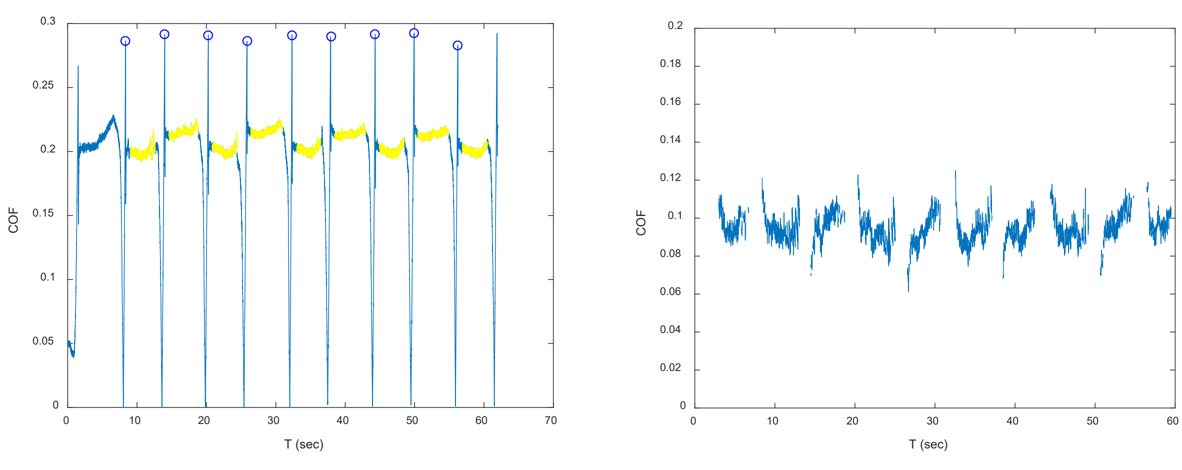

Fig. 4.10 Typical COF versus time plot for (a) a particle-wall friction test of wheat on acrylic, (b) an inter-particle friction test of wheat on wheat

Table 4.3 Static and dynamic COFs measured for grain kernels sliding against different types of materials

Type of grain kernel	Type of contact surface	Type of COF	COF[a]
Corn	Low carbon steel	Static	0.24 (0.05)
		Dynamic	0.22 (0.06)
Corn	Acrylic	Static	0.22 (0.03)
		Dynamic	0.16 (0.01)
Corn	Corn	Dynamic	0.09 (0.02)
Wheat	Low carbon steel	Static	0.32 (0.02)
		Dynamic	0.30 (0.02)
Wheat	Acrylic	Static	0.29 (0.03)
		Dynamic	0.20 (0.02)
Wheat	Wheat	Dynamic	0.18 (0.04)

[a] Values in parentheses are standard deviations.

4.3.1.3 Coefficient of Restitution

Using the glued-sphere clumps generated in section 4.3.1.1, the average bin numbers from the DEM simulations at different particle-wall COR levels were calculated. Fig. 4.11 is a plot of the average bin numbers versus the particle-wall COR. The COR values range from 0.6 to 0.95 with an interval of 0.05. The experimental results for different contact material combinations are summarized in Table 4.4. The COR values that minimized the difference between the average bin numbers from the simulation and the experiment were interpolated based on Fig. 4.11 and are listed in the third row of Table 4.4. DEM simulations were run using these interpolated particle-wall COR levels and the corresponding means and standard deviations of the bin numbers are listed in the second row of Table 4.4. Qualitative comparisons were also made between the simulation and experiment using plots of the cumulative frequency distributions of the number of kernels in different bins as shown in Fig. 4.12.

According to the results, the simulations using the calibrated CORs were able to generate the means, standard deviations, and cumulative frequency distributions that were close to the experimental values. While the mean of the bin numbers is mainly determined by the particle-wall COR, the standard deviation and the cumulative frequency distribution are related to the particle shape representation. For instance, when a single-sphere model with a fixed COR is used in the simulation, all the particles will fall into the same bin. Thus, the standard deviation of the bin numbers is zero for this case. The standard deviation becomes non-zero when the particles are modeled as glued-sphere clumps. The good agreement between the results suggests that not only the particle-wall COR but also the particle shape were estimated adequately.

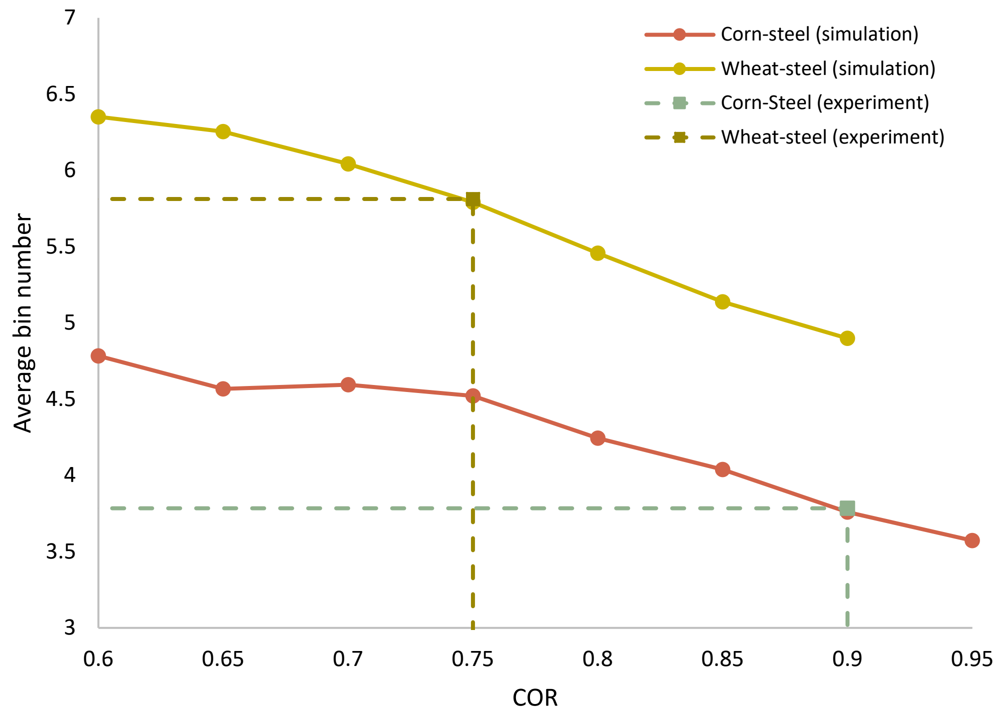

(a)

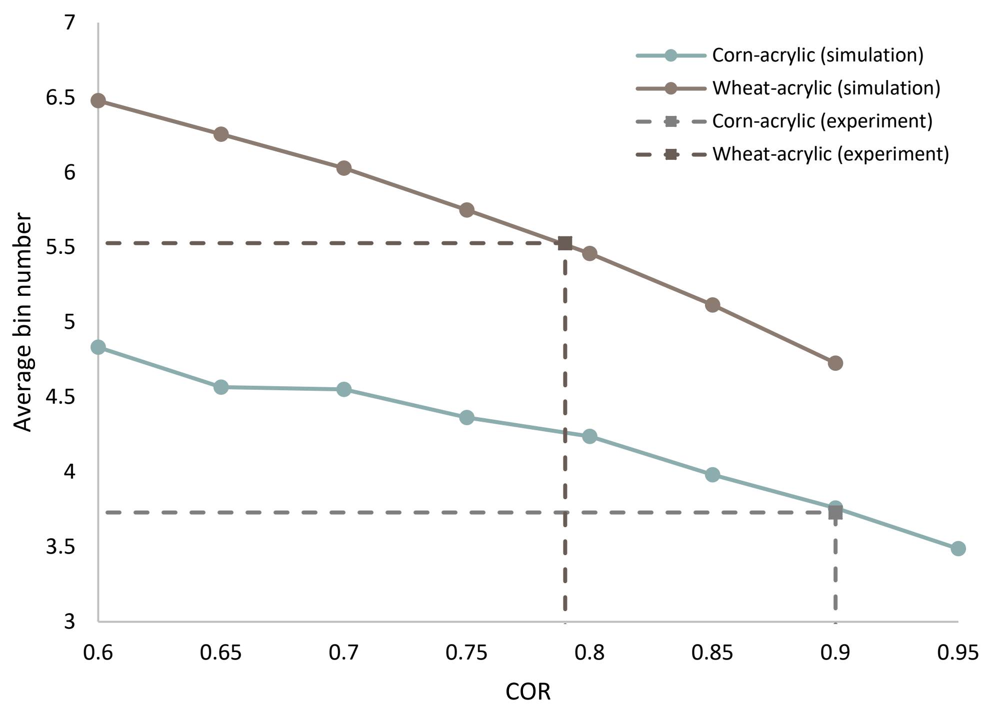

(b)

Fig. 4.11 Average bin numbers for different particle-wall COR levels. (a) Steel as the impact surface; (b) Acrylic as the impact surface

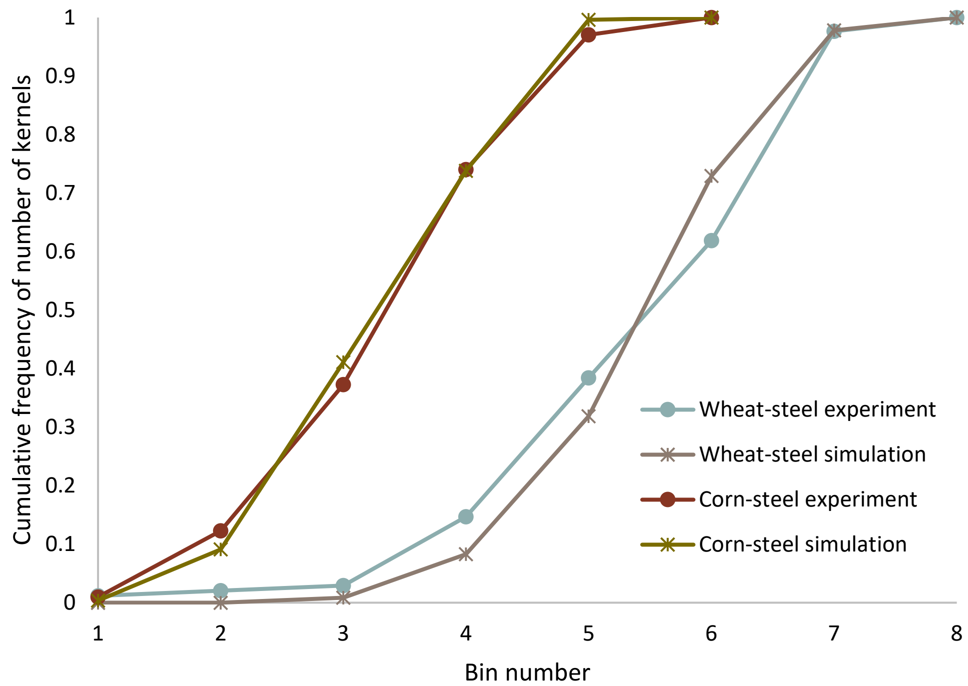

(a)

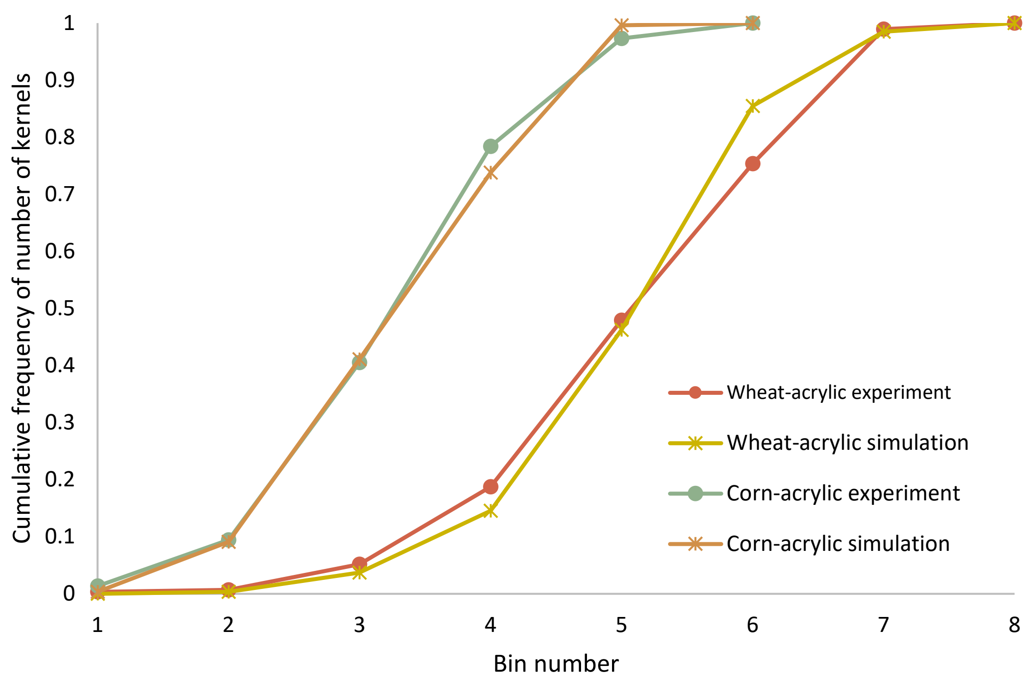

(b)

Fig. 4.12 Cumulative frequency distribution of number of particles in different bins. (a) Steel as the impact surface; (b) Acrylic as the impact surface

Table 4.4 Average bin numbers from experiment and calibrated particle-wall CORs based on simulated results

	Corn-Steel[a]	**Corn-Acrylic**[a]	**Wheat-Steel**[a]	**Wheat-Acrylic**[a]
Average bin number-Experiment	3.78 (1.04)	3.73 (0.99)	5.81 (1.28)	5.53 (1.20)
Average bin number-Simulation	3.76 (0.96)	3.76 (0.96)	5.78 (0.97)	5.51 (1.03)
Particle-wall COR	0.90	0.90	0.75	0.79

[a] Values in parentheses are standard deviations.

4.3.2 Bulk Material Test

Using the methods described in section 4.2, the material and interaction properties of corn and wheat kernels were determined as listed in Table 4.5. The values were used as input for the DEM simulations of bulk material tests.

Table 4.5 The values of the input parameters of the DEM simulations

Input parameters	**Corn**	**Wheat**	**Source**
Particle shape	/	/	X-ray micro-CT test and ASG software
Particle mass	/	/	Electronic balance
Young's modulus (MPa)	26	22	[10]
Poisson's ratio	0.4	0.18	[10]
Coefficients of friction			
Kernel-Kernel	0.09	0.18	Reciprocating pin tribometer
Kernel-Steel	0.22	0.30	Reciprocating pin tribometer
Coefficients of restitution			
Kernel-Kernel	0.25	0.25	[10]
Kernel-Steel	0.90	0.75	Drop kernel test
Coefficient of rolling friction			
Kernel-Kernel	0	0	Assumption
Kernel-Steel	0	0	Assumption

4.3.2.1 Bulk Density

For corn, the bulk densities measured experimentally and predicted by the simulation are 777.5±4.0 g/cm^3 and 787.5 g/cm^3, respectively, with a percentage error of 1.2% (Table 4.6). For wheat, the bulk densities measured in experiment and simulation are 756.6±0.9 g/cm^3 and 764.0 g/cm^3, respectively, with a percentage error of 0.9%. A good agreement between the experimental and simulation results was achieved since the material and interaction properties were accurately measured. The major factors affecting the grain bulk density are the particle size and shape, and the density/mass of an individual particle. The size and shape of the particle were captured by the X-ray micro-CT scanner with a high resolution. Glued-sphere clumps generated by the ASG software gave an acceptable shape representation of the scanned particle with a low volumetric difference and a very similar mass distribution.

Table 4.6 Bulk density values acquired from experiment and simulation

	Experiment (g/cm^3)[a]	**Simulation (g/cm^3)[a]**	**Percentage error (%)**
Corn	777.5 (4.1)	784.3 (2.9)	1.2
Wheat	756.6 (0.9)	765.4 (1.7)	0.9

[a] Values in parentheses are standard deviations.

4.3.2.2 Angle of Repose

The images of the corn and wheat piles taken during the experiment and predicted by the simulation are shown in Fig. 4.13. To make a qualitative comparison between the pile outlines, the images were processed using MATLAB. The pile and the background were separated by converting the original RGB images into binary images, i.e. images with only black and white picture elements, by using color filters. The outlines of the piles can then be easily identified and plotted together for comparison as shown in Fig. 4.14. For the corn piles, the experimental and simulated results agree well as the outlines have similar shapes and approximately the same heights. For the wheat, the size of the pile in the simulation is slightly larger than the size of the pile in the experiment.

In most of the previous studies, the experimental and simulation results of the angle of repose test were quantitatively compared on the basis of the angles of the piles [25, 29]. However, Fraczek et al. [30] stated that the angle measurement could be subjective and biased when the shape of the pile is not a "perfect" cone. Due to the large particle size and irregular shape, grain kernels commonly form a cone with a convex or concave surface. Thus, the pile angle was not used as an indicator of the similarity of two piles in the current study. Instead, the height of the pile was measured based on the outline acquired by MATLAB and normalized by the radius of the pan.

In addition, as the height of the pile was described as a function of the horizontal position, the height difference between the outlines of the piles, ΔH, can be calculated at different horizontal positions. The sum of squares of the height difference, $SS_{\Delta H}$, can be used as a quantitative measurement of the similarity between the two pile shapes. The sum of squares of the height difference is calculated as,

$$SS_{\Delta H} = \sum_{i=1}^{n} \left[H_{sim}(x_i) - H_{exp}(x_i)\right]^2 \tag{4.7}$$

where x_i is the horizontal position, $H_{sim}(x_i)$ is the height of the pile formed in the simulation, $H_{exp}(x_i)$ is the height of the pile formed in the experiment, n is the total number of horizontal positions being used. This sum of squares value is useful when a calibration test is conducted. The input parameters of the DEM simulation can be adjusted to minimize the sum of squares of the height difference, which will lead to a more objective result compared with minimizing the differences between the pile angles.

The ratios of the pile height to the pan radius are presented in Table 4.7. The low percentage error for both corn and wheat tests indicate that the particle shape, inter-particle dynamic COF, and rolling COF were estimated properly since these parameters have significant effects on the shape of the pile formed in the angle of repose test [26, 31]. The percentage error for the wheat test (7.5%) is high compared with the percentage error of corn test (3.4%). One possible reason causing this is that the inter-particle COF of wheat was not measured as accurately as that of corn. As reported by Chen et al. [32], corn kernels have a relatively flat contact surface compared with wheat kernels, which resulted in more consistent COF measurements.

Table 4.7 Ratio of pile height to pan radius acquired from experiment and simulation

	Experiment[a]	**Simulation[a]**	**Percentage error (%)**
Corn	0.41 (0.02)	0.42 (0.01)	3.4
Wheat	0.44 (0.03)	0.47 (0.02)	7.5

[a] Values in parentheses are standard deviations.

(a)

(b)

Fig. 4.13 Images of the grain piles (a) corn piles; (b) wheat piles. The experimental results are shown on the left and simulation results are shown on the right.

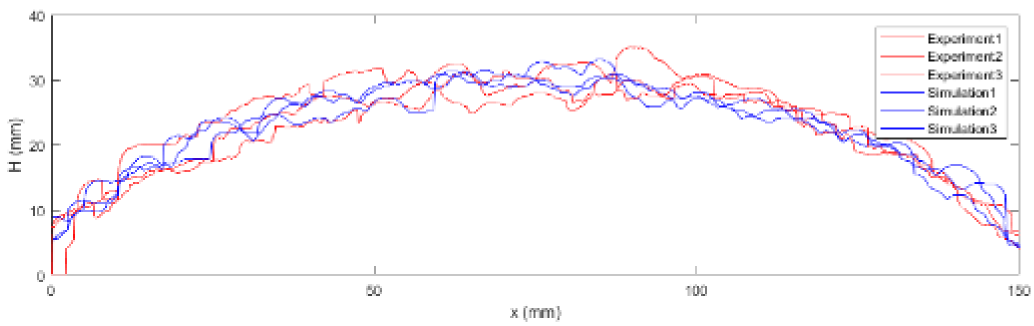

(a)

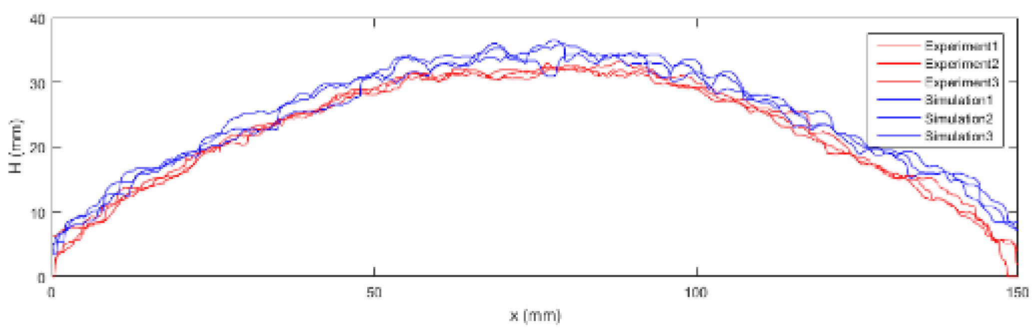

(b)

Fig. 4.14 Outlines of the grain piles extracted by MATLAB from the experimental and simulated results. (a) Corn piles; (b) Wheat piles. Red lines are used for experiments and blue lines are used for simulations

4.4 Summary

The material and interaction properties of corn and wheat kernels for DEM simulations were determined using several different approaches. In particular, the particle shape, mass, particle-wall, and inter-particle COFs were measured on single particles with an X-ray micro-CT scanner, electronic balance, and reciprocating-pin tribometer, respectively; the particle-wall CORs were calibrated using a self-developed test setup. The values of Young's modulus, Poisson's ratio, and inter-particle CORs were estimated by using literature values. The values of these properties were used to simulate a bulk density test and an angle of repose test. The bulk behavior of the particles in the simulation and experiment were compared both qualitatively and quantitatively. Good agreements were found between experimental and simulation results.

The bulk density and angle of repose test used in the current study are mainly influenced by particle shape, mass, inter-particle COF, and rolling COF. The low percentage errors between the experimental and simulation results imply that these parameters were estimated properly. For future work, bulk material tests whose results are sensitive to changes in particle-wall COF, COR and Young's modulus could be identified and then conducted to validate the correctness of the remaining parameters.

4.5 References

[1] Cundall, P. A., & Strack, O. D. L. (1979). A discrete numerical model for granular assemblies. *Géotechnique*, *29*(1), 47–65. doi:10.1680/geot.1979.29.1.47

[2] Lei, X., Liao, Y., & Liao, Q. (2016). Simulation of seed motion in seed feeding device with DEM-CFD coupling approach for rapeseed and wheat. *Computers and Electronics in Agriculture*, *131*, 29–39. doi:10.1016/J.COMPAG.2016.11.006

[3] Yu, Y., Fu, H., & Yu, J. (2015). DEM-based simulation of the corn threshing process. *Advanced Powder Technology*, *26*(5), 1400–1409. doi:10.1016/j.apt.2015.07.015

[4] Mousaviraad, M., Tekeste, M. Z., & Rosentrater, K. A. (2017). Calibration and Validation of a Discrete Element Model of Corn Using Grain Flow Simulation in a Commercial Screw Grain Auger. *Transactions of the ASABE*, *60*(4), 1403–1415. doi:10.13031/trans.12200

[5] Patwa, A., Ambrose, R. P. K., & Casada, M. E. (2016). Discrete element method as an approach to model the wheat milling process. *Powder Technology*, *302*, 350–356. doi:10.1016/j.powtec.2016.08.052

[6] Azmir, J., Hou, Q., & Yu, A. (2019). CFD-DEM simulation of drying of food grains with particle shrinkage. *Powder Technology*, *343*, 792–802. doi:10.1016/J.POWTEC.2018.11.097

[7] Tao, H., Jin, B., Zhong, W., Wang, X., Ren, B., Zhang, Y., & Xiao, R. (2010). Discrete element method modeling of non-spherical granular flow in rectangular hopper. *Chemical Engineering and Processing: Process Intensification*, *49*(2), 151–158. doi:10.1016/j.cep.2010.01.006

[8] Coetzee, C. J. (2017). Review: Calibration of the discrete element method. *Powder Technology*, *310*, 104–142. doi:10.1016/j.powtec.2017.01.015

[9] Boac, J. M., Casada, M. E., Maghirang, R. G., & Harner, J. P. I. (2010). Material and interaction properties of selected grains and oilseeds for modeling discrete particles. *Transactions of the ASABE*, *53*(4), 1201–1216. doi:10.13031/2013.32577

[10] Horabik, J., & Molenda, M. (2016). Parameters and contact models for DEM simulations of agricultural granular materials: A review. *Biosystems Engineering*, *147*, 206–225. doi:10.1016/j.biosystemseng.2016.02.017

[11] Coetzee, C. J., & Els, D. N. J. (2009). Calibration of discrete element parameters and the modelling of silo discharge and bucket filling. *Computers and Electronics in Agriculture*, *65*(2), 198–212. doi:10.1016/j.compag.2008.10.002

[12] Coetzee, C. J. (2016). Calibration of the discrete element method and the effect of particle shape. *Powder Technology*, *297*, 50–70. doi:10.1016/j.powtec.2016.04.003

[13] Benvenuti, L., Kloss, C., & Pirker, S. (2016). Identification of DEM simulation parameters by Artificial Neural Networks and bulk experiments. *Powder Technology*, *291*, 456–465. doi:10.1016/j.powtec.2016.01.003

[14] Barrios, G. K. P., Carvalho, R. M. de, Kwade, A., & Tavares, L. M. (2013). Contact parameter estimation for DEM simulation of iron ore pellet handling. *Powder Technology*, *248*, 84–93. doi:10.1016/j.powtec.2013.01.063

[15] Elskamp, F., Kruggel-Emden, H., Hennig, M., & Teipel, U. (2017). A strategy to determine DEM parameters for spherical and non-spherical particles. *Granular Matter*, *19*(3), 46. doi:10.1007/s10035-017-0710-0

[16] DEM Solutions Ltd. (2016). EDEM 2.6 Theory Reference Guide.

[17] Cleary, P. W. (2001). Recent advances in DEM modelling of tumbling mills. *Minerals Engineering*, *14*(10), 1295–1319. doi:10.1016/S0892-6875(01)00145-5

[18] ASABE Standard. (2017). *S352.2: Moisture Measurement-Unground Grain and Seeds*. St. Joseph, MI: ASABE. Retrieved from https://elibrary.asabe.org/azdez.asp?JID=2&AID=24272&CID=s2000&T=2

[19] Lommen, S., Schott, D., & Lodewijks, G. (2014). DEM speedup: Stiffness effects on behavior of bulk material. *Particuology*, *12*, 107–112. doi:10.1016/j.partic.2013.03.006

[20] Härtl, J., & Ooi, J. Y. (2008). Experiments and simulations of direct shear tests: porosity, contact friction and bulk friction. *Granular Matter*, *10*(4), 263–271. doi:10.1007/s10035-008-0085-3

[21] Xu, Y., Kafui, K. D., Thornton, C., & Lian, G. (2002). Effects of material properties on granular flow in a silo using DEM simulation. *Particulate Science and Technology*, *20*(2), 109–124. doi:10.1080/02726350215338

[22] Price, M., Murariu, V., & Morrison, G. (2007). Sphere clump generation and trajectory comparison for real particles. In *Proceedings of Discrete Element Modelling 2007*.

[23] ASTM. (2010). *G133−05: Standard Test Method for Linearly Reciprocating Ball-on-Flat Sliding Wear*. West Conshohocken, PA: ASTM Int. doi:10.1520/G0133-05R10.2

[24] Stroshine, R. (2008). *Physical properties of agricultural materials and food products*.

[25] Chen, Z., Yu, J., Xue, D., Wang, Y., Zhang, Q., & Ren, L. (2018). An approach to and validation of maize-seed-assembly modelling based on the discrete element method. *Powder Technology*, *328*, 167–183. doi:10.1016/j.powtec.2017.12.007

[26] Wang, X., Yu, J., Lv, F., Wang, Y., & Fu, H. (2017). A multi-sphere based modelling method for maize grain assemblies. *Advanced Powder Technology*, *28*(2), 584–595. doi:10.1016/j.apt.2016.10.027

[27] Pasha, M., Hare, C., Ghadiri, M., Gunadi, A., & Piccione, P. M. (2016). Effect of particle shape on flow in discrete element method simulation of a rotary batch seed coater. *Powder Technology*, *296*, 29–36. doi:10.1016/j.powtec.2015.10.055

[28] Lien, S., & Kajiya, J. T. (2013). A symbolic method for calculating the integral properties of arbitrary nonconvex polyhedra. *IEEE Computer Graphics and Applications*, *4*(10), 35–42. doi:10.1109/mcg.1984.6429334

[29] Kanakabandi, C. K., & Goswami, T. K. (2019). Determination of properties of black pepper to use in discrete element modeling. *Journal of Food Engineering*, *246*, 111–118. doi:10.1016/J.JFOODENG.2018.11.005

[30] Fraczek, J., Złobecki, A., & Zemanek, J. (2007). Assessment of angle of repose of granular plant material using computer image analysis. *Journal of Food Engineering*, *83*(1), 17–22. doi:10.1016/j.jfoodeng.2006.11.028

[31] Derakhshani, S. M., Schott, D. L., & Lodewijks, G. (2015). Micro–macro properties of quartz sand: Experimental investigation and DEM simulation. *Powder Technology*, *269*, 127–138. doi:10.1016/J.POWTEC.2014.08.072

[32] Chen, Z., Wassgren, C., & Ambrose, R. P. K. (2019). Measurements of grain kernel friction coefficients using a reciprocating pin tribometer. *Transaction of the ASABE*. [in review]

5. DAMAGE RESISTANCE OF CORN AND WHEAT KERNELS TO COMPRESSION, FRICTION, AND REPEATED IMPACTS

5.1 Introduction and Background

Grain kernel damage is one of the common problems associated with harvesting and handling, as grain kernels are subject to a combination of compression, impact and friction loads during these operations [1]. Damage resistance is an important mechanical property of the grain kernel. It describes the relationship between the external loads and the resulting damage to the kernel. The information is useful for optimizing the equipment design and adjusting operational settings, thereby minimizing the grain kernel damage.

Damage caused by a compression load is common in harvesting and handling. One typical example is kernels jamming between machine components. Though compression damage is normally undesirable, some operations, such as dehulling [2], milling [3], and oil extraction [4], are specifically designed to damage the structure of the grain kernel using compression. The compression loading behavior of different types of grain, including corn [5, 6], wheat [7, 8], soybeans [9, 10], rice [11], and barley [12], has been widely studied by researchers. The most common test device to measure the compression resistance of the grain kernel is the universal testing machine. During the test, an individual kernel is compressed between two parallel plates. The force applied to the kernel and the kernel deformation are recorded by the device and force-deformation curves are plotted. The compression resistance is quantified either as the peak force or the energy absorbed by the kernel when the damage occurs [13]. For the same type of grain, the compression resistance is affected by the testing conditions and grain kernel material properties. The influence of different factors, including moisture content [14], composition [15], loading orientation [16], and loading rate [17] have been investigated.

Impact is one of the major mechanisms that lead to grain kernel damage. The damage can be significant when kernels are impacted by machine components moving at a high velocity, such as when passing through combine harvester [18] or bucket elevator [19]. In addition, the kernels are subject to damage when they are accelerated to high velocity and impact on a hard surface, e.g. when conveying by pneumatic conveyor [20] and free falling from a high elevation [21]. Various lab devices have been developed for impact damage testing including the centrifugal impactor [22], the rotary hammer impactor [23], the drop bar impactor [24], and the pneumatic projector

[25]. Though the features of these devices are different, the basic principle of the tests is to subject the kernels to impact at specified velocities. The degree of impact damage is correlated with the impact velocity and/or impact energy. The major factors affecting the degree of impact damage are moisture content [26], impact velocity [27], orientation of loading [28], impact surface [21], and angle of impact [29].

Little research has been conducted to investigate the grain damage caused by the frictional forces, and wear damage to the kernels is not specifically mentioned in the grain inspection handbook published by the United States Department of Agriculture [30]. The reason for this may be that wear damage is not as serious as compression and impact damage. One mechanical property related to the grain wear resistance is the abrasive hardness index (AHI), which is defined as the time to abrade 1% of the kernel as fines [31]. The kernel with a higher AHI value is tougher and it is more difficult to abrade using frictional forces. AHI was determined with a tangential abrasive dehulling device (TADD) developed by Oomah, Reichert, and Youngs in [32]. During the test, several grams of grain sample were placed in bottomless cups and wear on a rotating disk was determined. It is worth noticing that the AHI is measured at the bulk material level. No test was found that quantified the grain wear damage at the single particle level. For inorganic material, the pin-on-disk test is a conventional method to determine wear [33]. For this test, the sample material is manufactured in a standard shape and exposed to a rotating disk. The amount of wear is quantified by the change of sample weight or dimension, which can be correlated with the amount of work done by the frictional force.

As the damage mechanism of different types of loading is different, previous individual studies usually only investigated one type of loading. The objective of the current study is to quantify the damage resistance of corn and wheat kernels to compression, friction, and repeated impacts and describe the results with statistical models.

5.2 Materials and Methods

5.2.1 Test Material

Corn and wheat samples were acquired from a local farm (Covington, IN). The moisture contents of the samples were measured using the whole kernel oven method described in ASABE standard S352.2 [34]. The moisture content of corn was 14.7% wet basis and the moisture content of wheat was 13.9% wet basis. For the tests, only the whole kernels, i.e. the fully intact kernels with no external cracks or kernel pieces chipped away [35], were used. The broken kernels and fine material were separated from the sample using sieves. The 16/64-inch round-hole sieve was used for corn and the 0.0064×3/8-inch oblong-hole sieve was used for wheat. The broken kernel pieces that were similar in size to whole kernels were handpicked out and discarded from the sieved sample.

5.2.2 Compression Test

The fracture resistance of the corn and wheat sample to compressive loading was measured with a universal testing machine (MTS Criterion Model 43, Eden Prairie, MN) as shown in Fig. 5.1. Quasi-static compression tests were performed to acquire the fracture force and fracture energy of the grain kernels following the test procedure described in ASAE S368.4 [36]. For each type of grain, 100 kernels were randomly selected from the sample. The individual kernel was placed between two parallel plates in its most stable orientation at which the kernel would not tend to fall down or roll. For wheat, the crease faced the bottom plate; for corn, the germ faced the bottom plate. The kernel was compressed at a constant loading rate of 1.25 mm/min. During the test, the displacement of the top plate and the compressive force were recorded at a data acquisition rate of 100 Hz. The test was stopped right after the initial fracture of the kernel. The fracture force was determined as the maximum force each test. The fracture energy was equal to the area under the force-displacement curve between the initial contact point and the fracture point. The fracture energy (E_{comp}) was estimated as,

$$E_{comp} = \sum_{i=1}^{n} F(t_i) \cdot [x(t_i) - x(t_{i-1})] \tag{5.1}$$

where $F(t)$ is the compressive force measured at the time t, $x(t)$ is the displacement of the top plate at the time t, t_0 is the time that the top plate is just in contact with the kernel, t_n is the time that the kernel fractures.

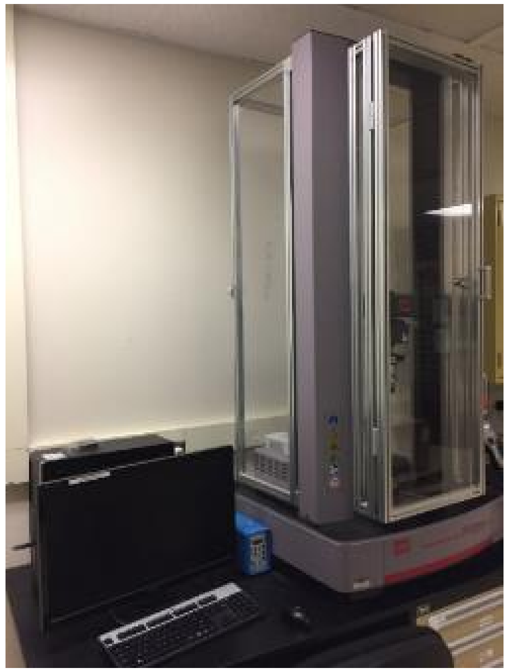

Fig. 5.1 Universal Testing Machine (MTS Criterion Model 43)

5.2.3 Repeated Impact Test

Single and repeated impacts test were conducted using a modified Wisconsin breakage tester (Fig. 5.2) to study the relationship between the impact energy and the damage probability of the grain kernels. A detailed description of the device configuration can be found in Lyon, Schmitt, Bern, and Hurburgh [37]. The main difference between the modified and original tester is that modified tester incorporates a variable frequency drive. In this way, the rotational speed of the impeller is adjustable, and the kernel can be impacted using different rotational speeds.

Fig. 5.2 Wisconsin breakage tester setup

Before the test began, subsamples with a sample size of 100 grams for corn and 25 grams for wheat were prepared using a Boerner divider. For both corn and wheat, the number of kernels in a subsample was around 300, which was high enough to generate results with low standards deviation according to a preliminary test. The test procedure for the single impact test followed the one developed by Singh and Finner [22]. At first, the tester was run empty until the desired speed level was reached. The sample was then fed into the impeller using a vibratory feeder. The kernels were spread out by the impellor and impacted on the cylinder wall. After the impact, the kernels were collected in a receiving box. The damaged kernels were separated from the whole kernel following the procedure described in section 3.1. The damage fraction (*DF*) of the subsample is calculated as,

$$DF = \frac{m_d}{m_0} \tag{5.2}$$

where m_d is the mass of the damaged kernels, and m_0 is the total mass of the subsample. For a specific speed level, the damage fractions of three replicate subsamples were assessed.

As for the repeated impacts test, the subsamples were impacted at the specified impellor rotational speeds for multiple times. After each impact, the kernels were manually inspected. The damaged kernels were weighed and excluded from the subsample. The undamaged kernels were fed into the tester again until all the kernels in the subsample were damaged or the number of impacts reached 10. The cumulative fraction of damage after a given number of impacts (n) can be calculated as,

$$DF = \frac{\sum_{i=1}^{n} m_{d,i}}{m_0} \tag{5.3}$$

Due to the complexity of the repeated impact test, only one subsample was tested for a specified speed level.

To establish damage probability curves for the corn and wheat, single impact and repeated impact tests were conducted at various impeller rotational speeds. The speeds were chosen based on the preliminary test to ensure that the damage fraction ranged approximately from 0% to 100%. A summary of the test speeds for different test configurations is given in Table 5.1. It is worth noticing that the speeds mentioned in the table are the target values, the actual rotational speed of the impeller during the test was measured with a tachometer.

Table 5.1 Impeller rotational speeds

Type of grain	**Type of test**	**Target speed level (rpm)**
Corn	Single impact	500, 900, 1400, 1800, 2200
	Repeated impacts	800, 1000, 1200
	High-speed camera	100, 2200, 2600
Wheat	Single impact	1400, 1800, 2200, 2600, 3000, 3400
	Repeated impacts	1800, 2000, 2200
	High-speed camera	100, 2200, 2600

As the gap between the impellor and the impact wall was small, it was assumed that the impact speed was equivalent to the linear speed of the kernel when it was discharged from the impellor. The impact speed, v_{imp}, was estimated based on the equation derived by Patterson and Reece [38],

$$v_{imp} = \sqrt{\left(\left[-\mu \pm \sqrt{\mu^2 + 1}\right] r\omega\right)^2 + (r\omega)^2} \tag{5.4}$$

where μ is the coefficient of friction between the impellor and the kernel, r is the radius of the impellor, and ω is the rotational speed of the impellor. The impellor was made of acrylic, and the impellor-kernel coefficients of friction were acquired from Chen, Ambrose, and Wassgren [39]. The mass-specific impact energy of the impact event i, $E_{m,imp,i}$, can be calculated using the impact velocity, $v_{imp,i}$.

$$E_{m,imp,i} = \frac{1}{2} v_{imp,i}^2 \qquad (5.5)$$

In this paper, a convention is used to denote a mass-specific energy as an energy symbol, E, with a subscript, m, i.e. E_m.

To validate the speeds calculated based on the equation 5.4, slow-motion videos were taken by a high-speed camera (Photron, San Diego, CA). The impact speed of the kernels in the videos was estimated using the image processing toolbox in MATLAB. For both corn and wheat, the impact speeds were measured at five different impellor speeds. For each impellor speed, the average impact speed of three replicate measurements was calculated and compared to the one calculated using equation 5.4.

5.2.4 Friction Test

The wear resistance of the grain was evaluated with a pin-on-disk tribometer (Bruker UMT TriboLab, Bilerica, MA). As shown in Fig. 5.3, the test system consists of top and bottom samples, top and bottom sample holders, a load cell, a driving unit, and a data acquisition system (DAQ). The conventional materials tested with this device are inorganics, like metals and alloys [40, 41], which can be fabricated into standard shapes like a disk or a sphere for testing. However, the grain kernels tested in the current study cannot be easily machined into a standard shape. Alternately, an intact kernel (top sample) was carefully superglued onto a 3D-printed pin, which was held by the top sample holder. The germ side of the corn kernel and the crease side of the wheat kernel were stuck onto the pin using superglue to ensure the surface in contact with the bottom sample was smooth. The representative structural materials used as the bottom sample were acrylic and low carbon steel because they are common in agricultural production and laboratory testing systems. The material was purchased in the form of flat plates of 0.25-inch thickness and then machined into circular disks of 2.75 in. diameter with a hole in the center. The disk was fixed onto the bottom sample holder with a screw.

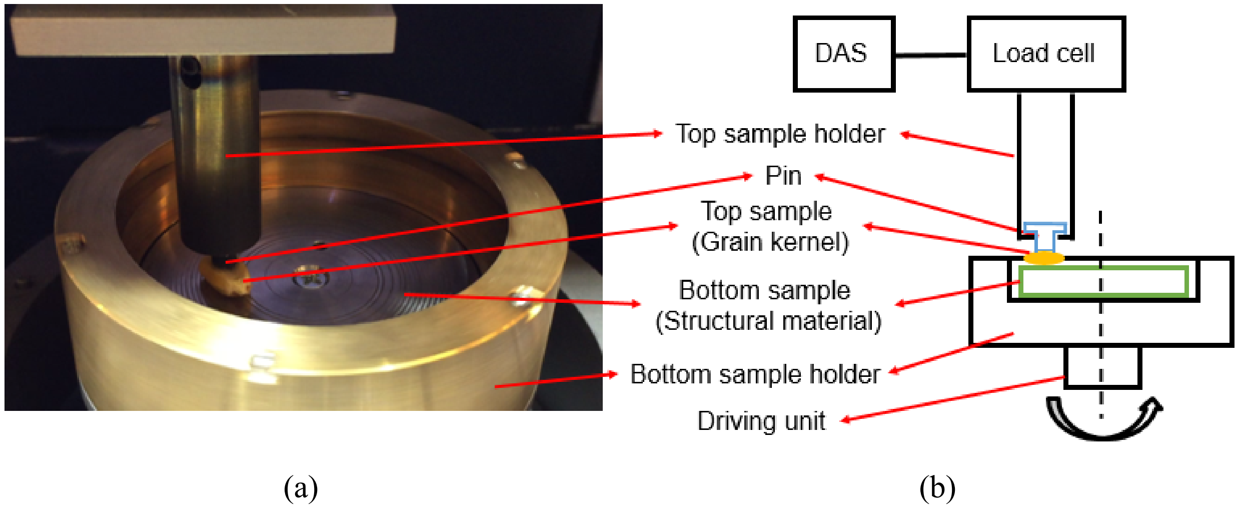

Fig. 5.3 Pin-on-disk setup. (a)Photograph; (b) schematic.

The standard test method for wear measurement with a pin-on-disk setup is described in ASTM G99 [33]. Immediately prior to the test, the contact surfaces of the top and bottom samples were cleaned with isopropyl alcohol and dried with lens cleaning tissue paper. The top sample was lowered vertically and pressed against the bottom sample. The normal force applied to the top sample was measured by the load cell and controlled at a specified level. The bottom sample then started to revolve about the disk center at a constant speed driven by the driving unit. With a data acquisition rate of 200 Hz, the tangential forces measured by the load cell were recorded by the DAS during the test. The appropriate test parameters, including the normal load and the disk rotational speed, were determined on the basis of preliminary tests. To prevent the large tangential force from causing the kernel to detach from the pin, a low normal load of 2 N and a low rotational speed of 20 rpm were used. The atmospheric conditions surrounding the device were controlled at a temperature level between 20-25°C and a relative humidity level between 40-50%.

The objective of the test was to quantify the amount of work that causes wear damage to the kernel. No previous studies were found to explicitly define the wear damage of grain kernels. In the current study, the kernel was classified as wear damaged when the pericarp was worn off and the endosperm was exposed to the environment. The exposed white endosperm can be easily identified because of the contrast with the yellow/brown pericarp. For the test, the kernel was first abraded with the disk for one minute and visually inspected. If the endosperm was not exposed, the previous procedure was repeated until the kernel was classified as wear damaged. With the tangential force data, the work done by the friction force can be calculated as the sum of the work done in each time step,

$$W_f = \sum_{i=0}^{n} F_{tang}(t_i) \cdot \Delta l = 2\pi r \cdot \omega \cdot \Delta t \cdot \sum_{i=0}^{n} F_{tang}(t_i) \tag{5.6}$$

where, $F_{tang}(t_i)$ is the tangential force at time t_i, Δl is the sliding distance within a time step, r is the distance between the kernel center and the disk center, ω is the disk rotational speed, Δt is the time step, t_o is the time that the test starts, and t_n is the time that the test stops. For each type of grain, the test was performed on 5 kernels which were randomly selected from the sample.

5.3 Results and Discussion

5.3.1 Compression Test

The fracture force and energy of 100 corn kernels and 100 wheat kernels was recorded and the average values were calculated. As reported in Table 5.2, the average values are 309.4 ± 107.1 N for the fracture force of corn, 83.4 ± 23.8 N for the fracture force of wheat, 48.7 ± 27.1 mJ for the fracture energy of corn, and 28.7 ± 13.5 mJ for the fracture energy of wheat. The higher average fracture force and energy of the corn indicates that the corn is more resistant to compression loading than the wheat. The literature that measured the compression resistance of the grains at similar moisture content as the current study was reviewed. Although there are variation among the result of different studies, overall the values measured in the current study agree with the measurements of the former studies. Difference in sample size, variety, and moisture content are the main causes that lead to variations in results. Besides, former studies considered that the area under the force-displacement curve, i.e. fracture energy, was equivalent to the area of a triangular area defined by the following equation [15, 42],

$$E_{comp} = \frac{1}{2} F_{frac} D_{frac} \tag{5.7}$$

where F_{frac} is the fracture force, and D_{frac} is the deformation at the fracture force. Though the calculation is simpler using equation 5.7, the result is less accurate compared to the calculation given by equation 5.1 which was used in the current study.

Table 5.2 Average fracture force and energy of corn and wheat kernels[a]

Type of grain	Moisture content (%)[b]	Variety	Fracture force (N)[c]	Fracture energy (mJ)[d]	Source
Corn	14.7	/	309.4 (107.1)	48.7 (27.1)	Current study
	13.7	DCC 370	228.5	95.8	[42]
	13.7	SC 704	188.4	57.7	[43]
	14.8 14.3 13.6	NS 6010 NS 4015 ZP 677	330 410 405	/	[6][c]
Wheat	13.9	SRW9606	83.4 (23.8)	28.7 (13.5)	Current study
	11.1	Kunduru 1149 Daphan Nenehatun Doğu 88 Lancer	131.8 (24.7) 80.5 (12.8) 96.6 (17.6) 114.9 (30.2) 122.2 (11.7)	34.3 (11.4) 19.6 (5.2) 23.0 (8.3) 32.5 (15.0) 33.1 (10.7)	[15]
	15	Shiroody	80.3	22.9	[7]

[a] Previous studies listed in the table used similar test procedure as the current study, i.e. a whole kernel was slowly compressed between two parallel plates with the germ side (corn) or crease side (wheat) facing the plate.
[b] Moisture content in wet basis.
[c] Values in parentheses are standard deviations.
[d] Values were estimated from figures.

The coefficients of variation defined as the ratio of the standard deviation to the mean were 35%, 29%, 55%, and 47% for corn fracture force, wheat fracture force, corn fracture energy, and wheat fracture energy, respectively. The large coefficients of variation indicate that the dispersion of the measurement is large. To better describe the data, frequency distributions and cumulative probability distributions were plotted as shown in Fig. 5.4 and 5.5. Different types of statistical distributions were fit to the empirical distribution using MATLAB. The goodness of fit was evaluated based on the Akaike information criterion (AIC) and Bayesian information criterion (BIC). It was found that the lognormal distribution described the empirical distributions of both fracture force and fracture energy well. The cumulative distribution function of the lognormal distribution, $F(x)$, can be expressed as,

$$F(x) = \Phi\left(\frac{\ln x - \mu}{\sigma}\right) \tag{5.8}$$

where Φ is the cumulative distribution function of the standard normal distribution, x is the value of the random variable, and μ and σ are two distribution parameters. The parameter μ represents the mean of the random variable's natural logarithm; while the parameter σ represents the standard deviation of the random variable's natural logarithm. The parameter values of the fitted lognormal distributions were listed in Table 5.3. The fitted parameters for corn are larger than the corresponding parameters for wheat, which aligns with the larger mean and standard deviation of the corn comparing to that of wheat.

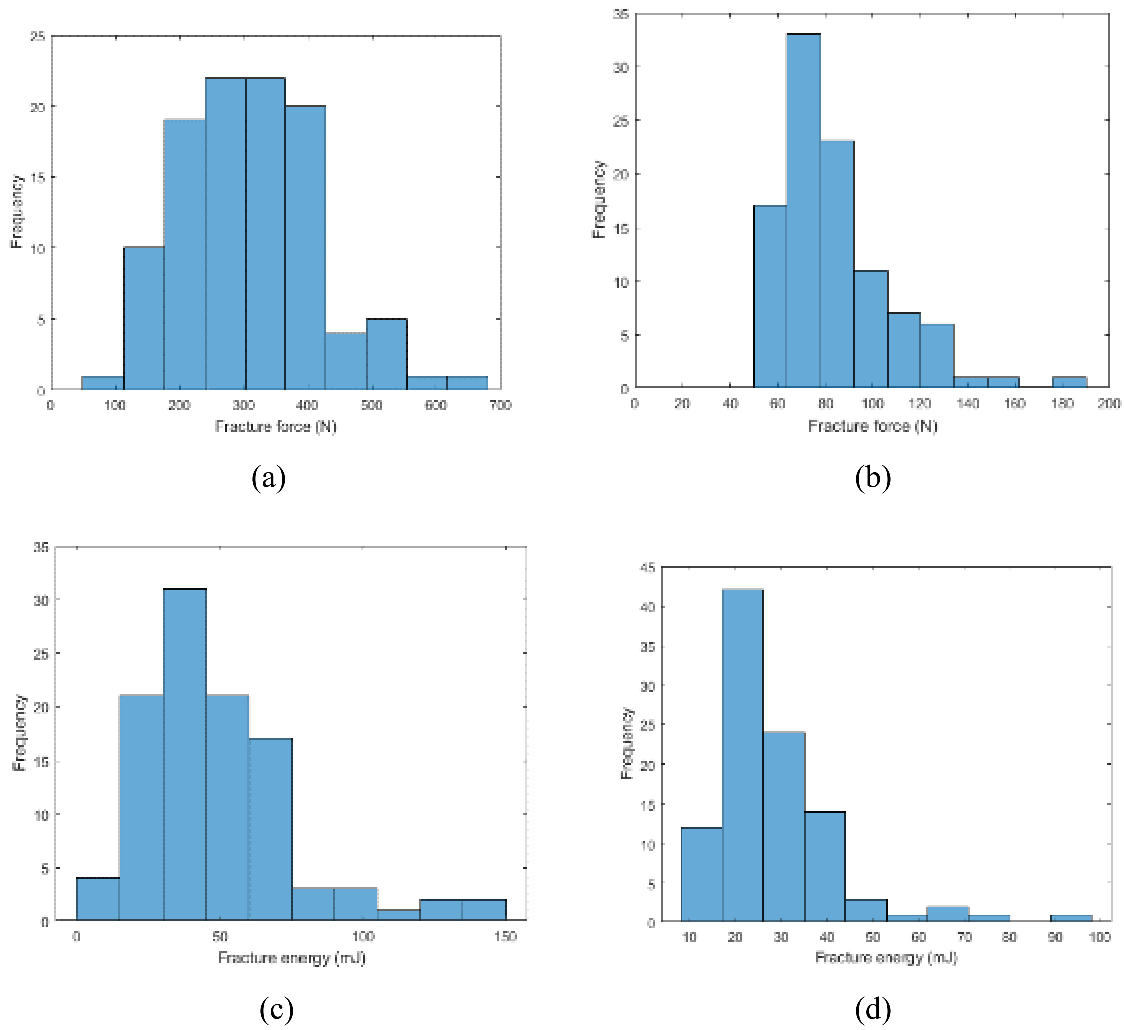

Fig. 5.4 Frequency distributions of (a) corn fracture force; (b) wheat fracture force; (c) corn fracture energy; (d) wheat fracture energy.

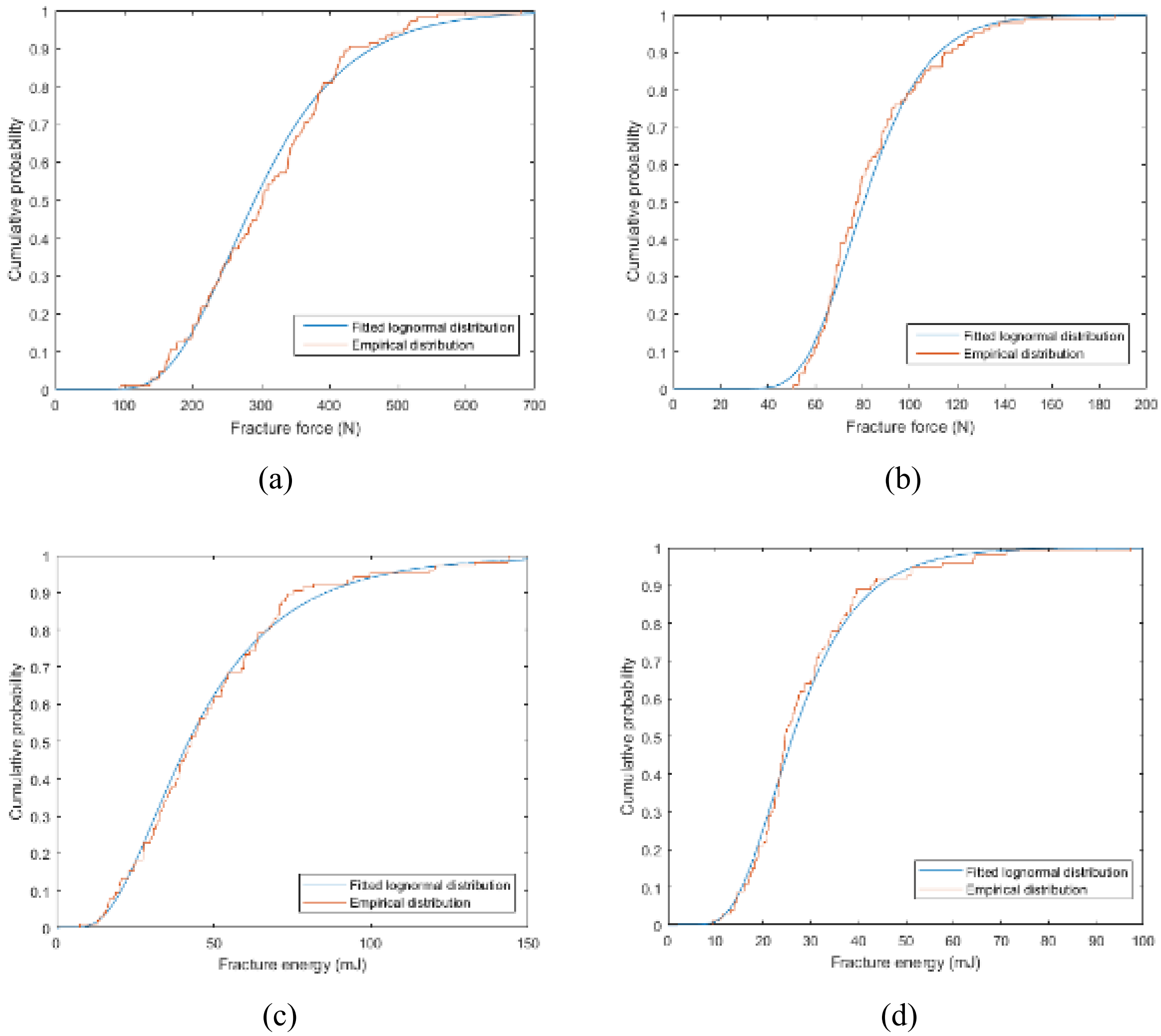

Fig. 5.5 Cumulative probability distributions of (a) corn fracture force; (b) wheat fracture force; (c) corn fracture energy; (d) wheat fracture energy.

Table 5.3 Parameters of the fitted lognormal distributions

Properties	μ	σ
Corn fracture force	5.67	0.36
Corn fracture energy	3.74	0.56
Wheat fracture force	4.39	0.26
Wheat fracture energy	3.27	0.41

5.3.2 Repeated Impact Test

The theoretical impact speed calculated using equation 5.4 was compared with the impact speed measured experimentally at three different rotational speeds as shown in Table 5.4. The standard deviations of the experimental measurements are small, which indicates that the kernel impact speed is consistent at a specific impellor speed level. It was found that equation 5.4 was able to predict the impact speed accurately with error rates less than 4%. Later in the test, at other speeds, only the impellor rotational speed was measured. The impact speed, as well as the impact energy, were estimated from the impellor rotational speed using equation 5.4.

Table 5.4 Theoretical impact speed and the experimentally measured impact speed

Type of grain	Impeller speed (rpm)	Impact speed (m/s)		Percentage error (%)
		Experimental values[a]	**Theoretical values**	
Corn	973	17.49 (0.40)	17.09	2.29
	2230	38.67 (0.26)	39.14	1.24
	2628	46.35 (0.70)	46.13	0.45
Wheat	979	17.13 (0.30)	16.58	3.22
	2276	39.84 (1.76)	38.545	3.25
	2667	46.98 (0.06)	45.167	3.85

[a] Experimental values are the average of three replicate measurements.

In repeated impact test, the impact velocity was controlled to be the same for all the impact events when the tester was operated at a specific impellor rotational speed. The cumulative mass-specific impact energy, $E_{m,imp,cum}$, can be calculated as,

$$E_{m,imp,cum} = \frac{1}{2} k v_{imp}^2 \tag{5.9}$$

where v_{imp} is impact velocity, and k is the number of impacts. For each type of grain, the damage fraction produced by a single impact test and repeated impact tests was plotted against the cumulative mass-specific impact energy in one figure as displayed in Fig. 5.6(a) and Fig. 6(b). As expected, the damage fraction increases with the impact energy. For a specific test condition, e.g. the single impact test or a repeated impact test at a certain speed, the data can be well modeled with linear regression. However, the sum of squared errors becomes large when a straight line is used to model both the single impact and repeated impact test data.

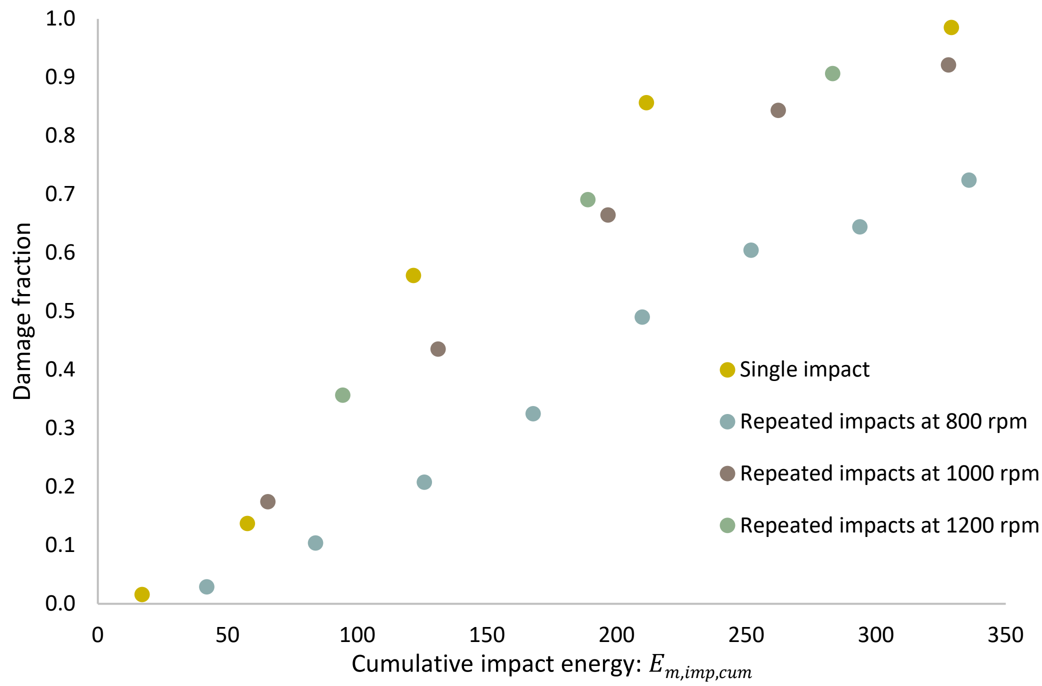

(a)

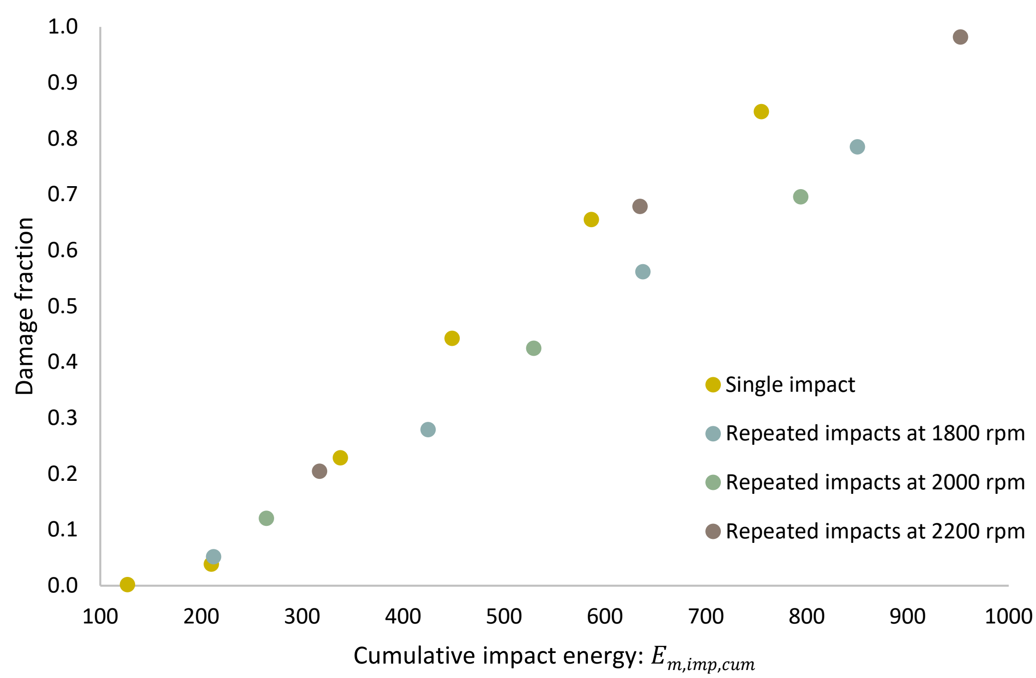

(b)

Fig. 5.6 Damage fraction versus cumulative impact energy. (a) Corn; (b) wheat.

To select a suitable model, the authors reviewed various studies on impact damage of grain kernels and other types of granular material [44]. It was found that the impact damage models developed for grain kernels were empirical models derived from experimental data using regression analyses. In addition, in most of the studies only single impact test were conducted with the exception of a study conducted in 2008 which included the number of impacts as a model parameter [45]. As for other types of granular material, the damage model developed by Vogel and Peukert [46] has been widely used in simulating the rock milling process [47–49]. The model was derived from dimensional analysis and a fracture mechanics model based on Weibull distribution and was validated experimentally with drop weight tests [50].

To model the fatigue damage due to the multiple impacts, mass-specific threshold energy, $E_{m,min}$, is introduced. The threshold energy is a material parameter acquired from a characterization experiment or simulation. It is assumed that the damage will only be generated when the impact energy of a contact event is larger the threshold energy. The portion of the energy that exceeds the threshold energy will be accumulated. When the impact energy is smaller than the threshold energy, no energy will be accumulated. Based on the description above, equation 5.10 describes the calculation of $E_{m,eff,i}$, the effective energy that can be accumulated as a result of impact event i. Finally, the cumulative effective impact energy of a particle, $E_{m,eff,cum}$, is computed by summing the $E_{m,eff,i}$ of all the impact events that the particles have experienced, as shown in equation 5.11.

$$E_{m,eff,i} = \begin{cases} 0\,, & E_{m,imp,i} \le E_{m,min} \\ E_{m,imp,i} - E_{m,min}\,, & E_{m,imp,i} > E_{m,min} \end{cases} \tag{5.10}$$

$$E_{m,eff,cum} = \sum_i E_{m,eff,i} \tag{5.11}$$

According to the model, a relationship was found between $E_{m,eff,cum}$ and the damage probability of particles, P_D, which can be expressed as,

$$P_D = 1 - \exp\{-f_{Mat.} x E_{m,eff,cum}\} \tag{5.12}$$

where x is the particle diameter; k is the number of impacts; $f_{Mat.}$ is the material damage property. When the impact velocity was controlled to be the same for all the impact events, the damage probability can be calculated as,

$$P_D = 1 - \exp\{-f_{Mat.} x k (E_{m,imp,i} - E_{m,min})\} \tag{5.13}$$

As mentioned earlier, the Vogel and Peukert model was based on a Weibull distribution, which has a cumulative distribution function as follows,

$$F(x) = 1 - \exp\left\{-\left(\frac{x-\theta}{\beta}\right)^{\alpha}\right\} \tag{5.14}$$

where x is the value of the random variable, and θ, α, and β are distribution parameters. Comparing the damage probability function with the cumulative distribution function of the Weibull statistic, θ is equivalent to the threshold energy, $E_{m,min}$; β is equivalent to $1/f_{Mat.}x$. The value of α was assumed to be 1 in the Vogel and Peukert model.

The Vogel and Peukert model was adopted to model the single and repeated impact tests data acquired in the current study with a minor modification. As the material being modeled was sieved grain, the sizes of the kernels were assumed to all be the same. Thus, the parameter that takes into account the shape effect, x, was dropped. Preliminary study found that the model did not provide a good fit to the data when α was assumed as 1. It was speculated that the value of α was related to the material property. Since the property of the biomaterial used in the current study (corn and wheat kernels) is greatly different from the properties of the inorganic materials (polymers, ore, and rock) used in the previous study, the α was included in the model as a fitted parameter. Considering the damage probability of a single particle as the damage fraction of particles in bulk, the modified Vogel and Peukert model can be written as,

$$DF = 1 - \exp\{-f_{Mat.}k(E_{m,imp,i} - E_{m,min})\}^{\alpha} \tag{5.15}$$

The model parameters, $f_{Mat.}$, $E_{m,min}$, and, α, can be acquired by fitting the data using the Excel Solver add-in and the least square error method.

The fitted model curves along with the experimental data points are plotted together in Fig. 5.7. The values of the model parameters are summarized in Table 5.5. As shown in the plot, the model fits the data well with R squared values over 0.99. Though $f_{Mat.}$, $E_{m,min}$, and, α are fitted parameters, they have physical meanings which reflect the material properties. $E_{m,min}$, the location parameter of the distribution is the minimum energy that initiates damage to a kernel. Wheat has a higher $E_{m,min}$ value than corn, meaning that wheat is more resistant to impact damage. This aligns with the findings of the previous studies [21, 51]. Drop tests were conducted by Fiscus, Foster, and Kaufmann [21], during which corn and wheat kernels were dropped from 100 ft. and impacted on a concrete surface with the grains at similar moisture content level. It was found that

12% of the corn was damaged while less than 1% of wheat was damaged. The scale parameter, $f_{Mat.}$, indicates the amount of dispersion of the distribution. When $f_{Mat.}$ is small, the distribution is stretched; while when $f_{Mat.}$ is large, the distribution is squeezed. The corn has a higher $f_{Mat.}$ value compared to the wheat; thus, the corn was damaged in a narrower range of impact energy. The shape parameter, α, controls the shape of the distribution curve. With α values both larger than one, the cumulative distributions of corn and wheat data were modeled with an "S"-shape curve.

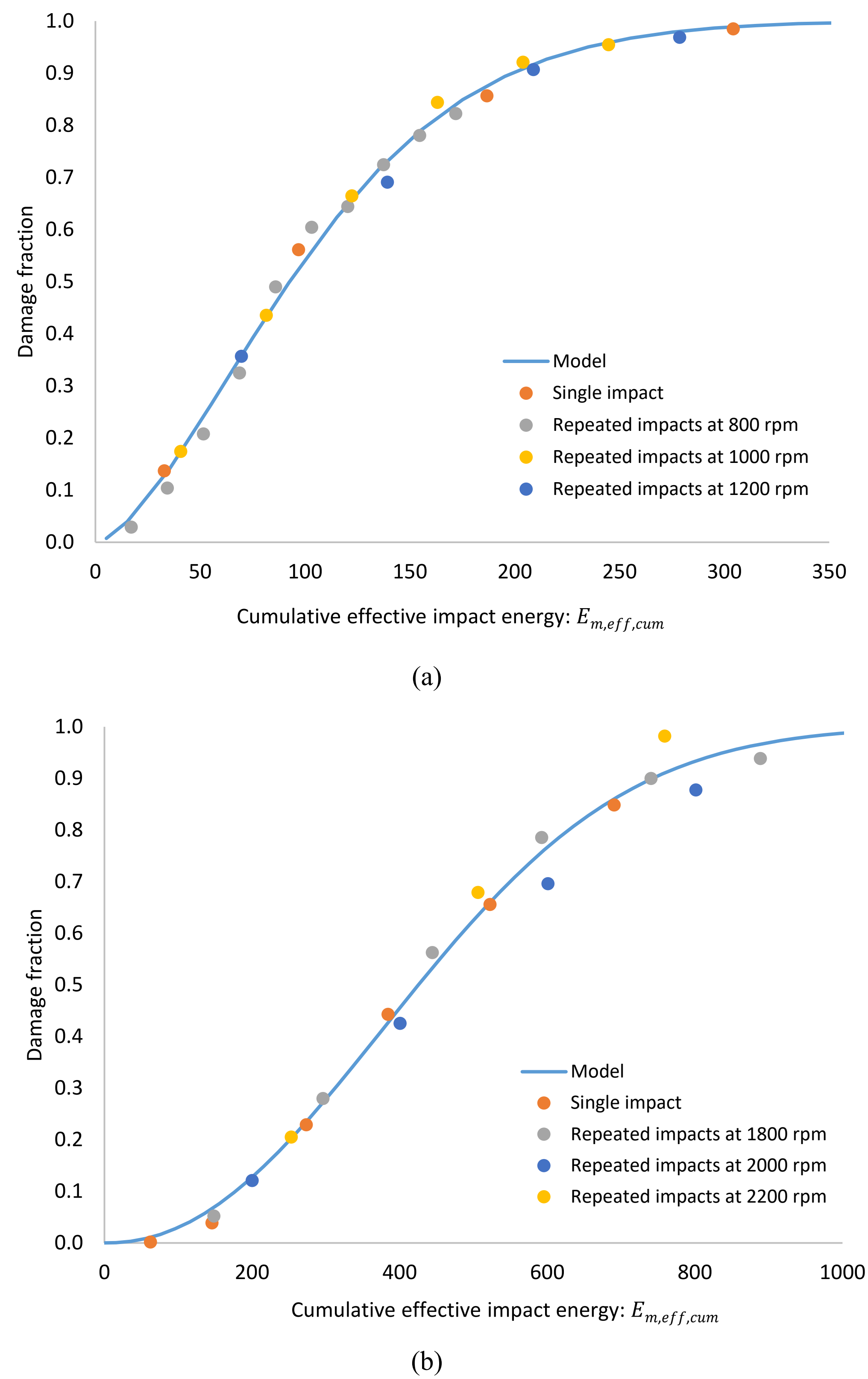

Fig. 5.7 Damage fraction modeled with a three-parameter Weibull distribution. (a) Corn; (b) wheat.

Table 5.5 Parameters of the fitted Weibull distributions

Type of grain	$f_{Mat.}$	$E_{m,min}$	α
Corn	0.0085	24.8	1.58
Wheat	0.0020	64.4	2.15

5.3.3 Friction test

A preliminary test was conducted with corn and wheat kernels sliding against steel and acrylic surfaces for 30 minutes. For corn-acrylic, corn-steel, and wheat-acrylic tests, no significant pericarp damage was identified after the test. The wear damage of the above-mentioned contact pairs was low because the contact surface of corn and acrylic was smooth with low coefficients of friction [39]. Besides, the pericarp of the corn kernel was hard at the low moisture content. It was observed that the acrylic surface was abraded after sliding against the corn kernel. Therefore, only the wear resistance of wheat on steel was quantified. Fig. 5.8 shows the wear damaged wheat kernels after sliding against the steel surface.

Fig. 5.8 Wear damaged wheat kernels after sliding against steel surface.

For wheat-steel tests, wheat kernels were commonly damaged after three to five minutes of sliding. The average work done by the friction force when the wear damage occurred, W_f, is 3.85 J, with a standard deviation of 1.50 J. It is worth noticing that the magnitude of W_f is much larger than E_{comp} or E_{imp}, meaning that the energy required to cause wear damage is much larger than the energy required to cause compression or impact damage. This may be the reason why wear damage is not a major concern during the grain handling process.

The current test only provided a rough estimation for the wear resistance since the kernel was checked for damage every one minute. Though slight variations existed among different test runs, the work done by the frictional force in one minute was around 1 J. Thus, the resolution of the measurements was limited to 1 J approximately. To acquire measurements with higher resolution, the frequency of damage checking should be increased. In addition, the wear resistance of the corn kernel could be measured by increasing the normal load and extending the sliding time until significant damage is observed. In that case, a safer connection method between the kernel and pin should be adopted. There is a concern that the kernel may detach from the pin when sliding for a long period of time under high normal load.

5.4 Conclusions

The fracture force and fracture energy under compression were 309.4 $\pm$ 107.1 N and 48.7$\pm$27.1 mJ for corn; and 83.4$\pm$23.8 N and 28.7$\pm$13.5 mJ for wheat. It was also demonstrated that the compression test data can be well modeled with the lognormal distribution. No significant pericarp damage was observed for corn-acrylic, corn-steel, and wheat-acrylic wear tests. The average work done to cause wear damage was 3.85$\pm$1.50 J for wheat sliding against a steel surface. A three-parameter Weibull distribution was used to model the single and repeated impact test data. The model provided a good fit to the experimental data with R square values over 0.99. It was found that corn kernels were more susceptible to impact loading, while wheat kernels were more susceptible to compression loading. Compared to the energy required to cause impact and compression damage, much higher energy was required to cause wear damage in wheat. No wear damage was observed for the corn kernels under a low normal load.

5.5 References

[1] Srivastava, A. K., Herum, F. L., & Stevens, K. K. (1976). Impact Parameters Related to Physical Damage to Corn Kernel. *Transactions of the ASAE*, *19*(6), 1147–1151.

[2] Das, S. K. (2000). Fracture resistance of sunflower seed and kernel to compressive loading. *Journal of Food Engineering*, *46*(1), 1–8. doi:10.1016/S0260-8774(00)00061-3

[3] Patwa, A., Ambrose, R. P. K., & Casada, M. E. (2016). Discrete element method as an approach to model the wheat milling process. *Powder Technology*, *302*, 350–356. doi:10.1016/j.powtec.2016.08.052

[4] Kabutey, A., Herak, D., Chotěborský, R., Dajbych, O., DiviŠova, M., & Boatri, W. E. (2013). Linear pressing analysis of Jatropha curcas L. seeds using different pressing vessel diameters and seed pressing heights. *Biosystems Engineering*, *115*(1), 43–49. doi:10.1016/j.biosystemseng.2012.12.016

[5] Tarighi, J., Mohtasebi, S. S., Mahmoudi, A., Rastilantie, M.-, & Mahmoodi, A. (2005). Effect of moisture content on some physical properties of safflower (var. Darab) seeds. *Agriculture & Environment*, *8*(4), 602–606.

[6] Babic, L. J., Radojein, M., Pavkov, I., Babic, M., Turan, J., Zoranovic, M., & Stanisic, S. (2013). Physical properties and compression loading behaviour of corn seed. *International Agrophysics*, *27*(2), 119–126. doi:10.2478/v10247-012-0076-9

[7] Gorji, A., Rajabipour, A., & Tavakoli, H. (2010). Fracture resistance of wheat grain as a function of moisture content, loading rate and grain orientation. *Australian Journal of Crop Science*, *4*(6), 448–452.

[8] Babić, L., Babić, M., Turan, J., Matić-Kekić, S., Radojčin, M., Mehandžić-Stanišić, S., … Zoranović, M. (2011). Physical and stress-strain properties of wheat (Triticum aestivum) kernel. *Journal of the Science of Food and Agriculture*, *91*(7), 1236–1243. doi:10.1002/jsfa.4305

[9] Liu, M., Haghighi, K., Stroshine, R. L., & Ting, E. C. (1990). Mechanical-properties of the soybean cotyledon and failure strength of soybean kernels. *Transactions of the ASAE*, *33*(2), 559–566.

[10] Paulsen, M. R. (1978). Fracture resistance of soybeans to compressive loading. *Transaction of The ASAE*, *21*(6), 1210–1216.

[11] Bagheri, I., & Dehpour, M. B. (2011). Effect of Moisture Content and Loading Rate on Mechanical Strength of Brown Rice Varieties, *5*(10), 1385–1391.

[12] Tavakoli, M., Tavakoli, H., Rajabipour, A., Ahmadi, H., & Gharib-Zahedi, S. M. T. (2009). Moisture-dependent physical properties of barley grains. *International Journal of Agricultural and Biological Engineering*, *2*(4), 84–91. doi:10.3965/j.issn.1934-6344.2009.04.084-091

[13] Selvam, T. A., Manikantan, M. R., Chand, T., Sharma, R., & Seerangurayar, T. (2014). Compression loading behaviour of sunflower seeds and kernels. *International Agrophysics*, *28*(4), 543–548. doi:10.2478/intag-2014-0045

[14] Putri, R. E., Yahya, A., Adam, N. M., & Aziz, S. A. (2015). Related Fracture Resistance with Moisture Content in Different Grain Orientation of Paddy Grain. *Journal of Biology, Agriculture and Healthcare*, *5*(11).

[15] Başlar, M., Kalkan, F., Kara, M., & Ertugay, M. F. (2012). Correlation between the protein content and mechanical properties of wheat. *Turkish Journal of Agriculture and Forestry*, *36*(5), 601–607. doi:10.3906/tar-1112-51

[16] Singh, K. K., & Goswami, T. K. (1996). Physical Properties of Cumin Seed. *Journal of Agricultural Engineering Research*, *64*, 93–98. doi:10.1016/S0260-8774(00)00049-2

[17] Saiedirad, M. H., Tabatabaeefar, A., Borghei, A., Mirsalehi, M., Badii, F., & Ghasemi-Varnamkhasti, M. (2008). Effects of moisture content, seed size, loading rate and seed orientation on force and energy required for fracturing cumin seed (Cuminum cyminum Linn.) under quasi-static loading. *Journal of Food Engineering*, *86*(4), 565–572. doi:10.1016/j.jfoodeng.2007.11.021

[18] Quick, G. R. (2003). Combine "sweet spot": integrating harvested yield, grain damage and losses. In *Proceedings of the International Conference on Crop Harvesting*. Louisville, Kentucky.

[19] Hall, G. E. (1974). Damage during handling of shelled corn and soybeans. *Transactions of the ASAE*, *17*(2), 335–338.

[20] Magee, K. J., Stroshine, R. L., Foster, G. H., & Baker, K. D. (1983). Nature and extent of grain damage caused by pneumatic conveying systems. In *Winter Meeting American Society of Agricultural Engineers American Society of Agricultural Engineers*.

[21] Fiscus, D. E., Foster, G. H., & Kaufmann, H. H. (1971). Physical Damage of Grain Caused by Various Handling Techniques. *Transactions of the ASAE*, *14*(3), 480–485.

[22] Singh, S. S., & Finner, M. F. (1983). A Centrifugal Impacter for Damage Susceptibility Evaluation of Shelled Corn. *Transactions of the ASAE*, *26*(6), 1858–1863.

[23] Khazaei, J. (2009). Influence of Impact Velocity and Moisture on Mechanical Damage in Beans Influence of Impact Velocity and Moisture Content on Mechanical Damages of White Kidney Beans Under Loadings. *Cercetări Agronomice în Moldova*, *42*(1(137)), 5–18.

[24] Shahbazi, F., Valizade, S., & Dowlatshah, A. (2017). Mechanical damage to green and red lentil seeds. *Food Science and Nutrition*, *5*(4), 943–947. doi:10.1002/fsn3.480

[25] Kirk, I. W., & McLeod, H. E. (1967). Cottonseed Rupture from Static Energy and Impact Velocity. *Transactions of the ASAE*, *10*(2), 217–219.

[26] Shahbazi, F., Saffar, A., & Analooei, M. (2011). Mechanical damage to navy beans as affected by moisture content, impact velocity and seed orientation. *Quality Assurance and Safety of Crops and Foods*, *3*, 205–211. doi:10.1111/j.1757-837X.2011.00114.x

[27] Ajayi, O. A., & Clarke, B. (1997). High velocity impact of Maize Kernels. *Journal of Agricultural and Engineering Research*, *67*(2), 97–104. doi:10.1006/jaer.1997.0156

[28] Bilanski, W. (1966). Damage resistance of seed grains. *Transactions of the ASAE*, *9*(3), 360–363.

[29] Keller, D. L., Converse, H. H., Hodges, T. O., & Chung, D. S. (1972). Corn Kernel Damage Due to High Velocity Impact. *Transactions of the ASAE*, *15*(2), 330–332.

[30] USDA. (2013). *Grain Inspection Handbook: Book II Grain Grading Procedures*. Washington, D.C. Retrieved from https://www.ams.usda.gov/sites/default/files/media/Book2.pdf

[31] Reicher, R. D., Oomah, B. D., & Youngs, C. G. (1984). Factors Affecting the Efficiency of Abrasive‐Type Dehulling of Grain Legumes Investigated with a New Intermediate‐Sized, Batch Dehuller. *Journal of Food Science*, *49*(1), 267–272. doi:10.1111/j.1365-2621.1984.tb13723.x

[32] Oomah, B. ., Reichert, R. D., & Youngs, C. G. (1981). A Novel, Multi-Sample, Tangential Abrasive Dehulling Device (TADD). *Cereal Chemistry*, *28*(5), 392–395. doi:10.1016/s0315-5463(81)72811-6

[33] ASTM. (2010). *G99 - Standard Test Method for Wear Testing with a Pin-on-Disk Apparatus*. West Conshohocken, PA. doi:10.1520/G0099-05R10

[34] ASABE Standard. (2017). *S352.2: Moisture Measurement-Unground Grain and Seeds*. St. Joseph, MI: ASABE. Retrieved from https://elibrary.asabe.org/azdez.asp?JID=2&AID=24272&CID=s2000&T=2

[35] U.S. Grains Council. (2017). *Corn harvest quality report*.

[36] ASAE Standard. (2012). *S368.3: Compression test of food materials of convex shape*. *American Society of Agricultural Engineering*.

[37] Lyon, H. J., Schmitt, S. G., Bern, C. J., & Hurburgh Jr., C. R. (1988). Characteristics of a modified Wisconsin breakage tester. *Transactions of the American Society of Agricultural Engineers*, *31*(6). Retrieved from http://lib.dr.iastate.edu/abe_eng_pubs

[38] Patterson, D. E., & Reece, A. R. (1962). The theory of the centrifugal distributor. I: Motion on the disc, near-centre feed. *Journal of Agricultural Engineering Research*, *7*(3), 232–240.

[39] Chen, Z., Wassgren, C., & Kingsly, A. R. P. (2019). Measurements of grain kernel friction coefficients using a reciprocating pin tribometer. *Transaction of the ASABE*. [in review]

[40] Deuis, R. L., Subramanian, C., & Yellup, J. M. (1996). Abrasive wear of aluminium composites - A review. *Wear*, *201*(1–2), 132–144. doi:10.1016/S0043-1648(96)07228-6

[41] Misra, A., & Finnie, I. (2009). A Review of the Abrasive Wear of Metals. *Journal of Engineering Materials and Technology*, *104*(2), 94. doi:10.1115/1.3225058

[42] Tarighi, J., Mahmoudi, A., & Alavi, N. (2011). Some mechanical and physical properties of corn seed (Var. DCC 370). *African Journal of Agricultural Research*, *6*(16), 3691–3699. doi:10.5897/AJAR10.521

[43] Seifi, M. R., & Alimardani, R. (2014). The Moisture Content Effect on Some Physical and Mechanical Properties of Corn (Sc 704). *Journal of Agricultural Science*, *2*(4), 125–134. doi:10.5539/jas.v2n4p125

[44] Chen, Z., Ambrose, R. P. K., & Wassgren, C. (2019). A Review of Grain Kernel Damage: Mechanisms, Modeling, and Testing Procedures. *Food Engineering Reviews*. [in review]

[45] Khazaei, J., Shahbazi, F., Massah, J., Nikravesh, M., & Kianmehr, M. H. (2008). Evaluation and modeling of physical and physiological damage to wheat seeds under successive impact loadings: Mathematical and neural networks modeling. *Crop Science*, *48*(4), 1532–1544. doi:10.2135/cropsci2007.04.0187

[46] Vogel, L., & Peukert, W. (2003). Breakage behaviour of different materials - Construction of a mastercurve for the breakage probability. *Powder Technology*, *129*(1–3), 101–110. doi:10.1016/S0032-5910(02)00217-6

[47] Morrison, R. D., Shi, F., & Whyte, R. (2007). Modelling of incremental rock breakage by impact - For use in DEM models. *Minerals Engineering*, *20*(3), 303–309. doi:10.1016/j.mineng.2006.10.015

[48] Bonfils, B., Ballantyne, G. R., & Powell, M. S. (2016). Developments in incremental rock breakage testing methodologies and modelling. *International Journal of Mineral Processing*, *152*, 16–25. doi:10.1016/j.minpro.2016.04.010

[49] Vogel, L., & Peukert, W. (2005). From single particle impact behaviour to modelling of impact mills. *Chemical Engineering Science*, *60*(18), 5164–5176. doi:10.1016/j.ces.2005.03.064

[50] Shi, F., & Kojovic, T. (2007). Validation of a model for impact breakage incorporating particle size effect. *International Journal of Mineral Processing*, *82*(3), 156–163. doi:10.1016/j.minpro.2006.09.006

[51] W. K. Bilanski. (1966). Damage Resistance of Seed Grains. *Transactions of the ASAE*, *9*(3), 360–363. doi:10.13031/2013.39978

6. DEVELOPMENT AND VALIDATION OF A MODEL FOR PREDICTING GRAIN IMPACT DAMAGE USING DEM

6.1 Introduction and Background

During the agricultural production process, the grain is subjected to a combination of impact, shear, and/or compression loading [1]. With poorly designed equipment or improper use of the equipment setting, a significant amount of grain kernels can be damaged by the high mechanical forces. Impact loading is one of the most common mechanisms that cause damage to the grain during harvesting and handling. For instance, the grain is impacted by the cylinder bar and the concave when being threshed inside a combine harvester; the grain impacts on the metal head covering when being discharged from a bucket elevator; and the grain is subject to impact when falling in a grain stream onto a hard surface from a significant height.

In previous studies, researchers have identified the factors that influence impact damage, including harvest and handling operational settings (e.g. concave clearance [2], cylinder speed [3], and conveying speed [4]), physical and mechanical properties of the grain (e.g. moisture content [5] and size [6]), and stressing conditions (e.g. impact velocity [7], impact angle [8], and kernel orientation [9]). Many efforts have been made to build regression models with the factors mentioned above to predict the damage level [7, 10–17]. However, these models have been derived purely from experimental data. Therefore, each of the models is only applicable to one specific type of gain processed by a specific device. This means that these models cannot be generalized and used for other materials and test systems.

Though there is a lack of understanding in the damage mechanism of grain, the damage mechanism of solid materials, like rock, mineral, and ceramic, has been investigated extensively by the science of comminution. Several models [18–20] have been derived based on fracture mechanics to describe the damage/breakage behavior of particulate materials under repetitive impact loading. Among these models, Vogel and Peukert's damage model [19] has been widely used in modeling the breakage behavior of various materials [21–23]. The model was also implemented in DEM and used to simulate the rock milling process [24–26].

In this study, the Vogel and Peukert's damage model was modified and used to predict the damage probability of grain caused by impact loading. The model was implemented in DEM and applied to simulate the Stein breakage tester. The simulation results were compared with the experimental results.

6.2 Materials and Methods

6.2.1 Contact Force Model

The Hertz-Mindlin no-slip model [27] was used as the contact force model, which was described in detail in section 4.2.1. The software used to conduct the DEM simulation in this study is EDEM 2019 (DEM Solutions Ltd., Edinburgh, UK). A damage model was implemented with the EDEM Application Programming Interface (API) to calculate and record custom particle properties, i.e. relative normal contact velocity and cumulative mass specific impact energy, and determine particle damage based on a damage probability function. The development and implementation of the damage model will be discussed in detail in the next section.

6.2.2 Damage Model Development and Implementation

The damage model developed by Vogel and Peukert [19] was adapted to predict the impact damage of grain kernels and implemented in the DEM simulation. The workflow of the model is shown in Fig. 6.1. Every time two elements are in contact the model is activated. The mass-specific impact energy, $E_{m,imp}$, is calculated based on the magnitude of the normal relative contact velocity, $|v_{rel,n}|$,

$$|v_{rel,n}| = \boldsymbol{v_{rel}} \cdot \boldsymbol{\hat{n}} \tag{6.1}$$

$$E_{m,imp} = \frac{1}{2}|v_{rel,n}|^2 \tag{6.2}$$

where $\boldsymbol{v_{rel}}$ is the relative velocity, $\boldsymbol{\hat{n}}$ is the unit vector normal to the contact plane. It is worth noticing that the impact energy of a contact event is calculated from the normal relative velocity not the total relative velocity. The reason of using normal relative velocity is that the focus of the current study is body breakage induced by high speed impact. It is common practice to consider that body breakage is controlled by normal energy dissipation while the abrasion is controlled by the tangential energy dissipation [25]. In addition, the impact energy is calculated for the corresponding contact event and needs to be further distributed between the two contact elements. The distribution of the impact energy depends on the type of the two contact elements. If two particles are in contact, half of the total impact energy will be assigned to each particle; while if a particle is in contact with structural material, all the impact energy will be assigned to the particle. This is based on the assumption that the stiffness of the particle is much less than the structural material.

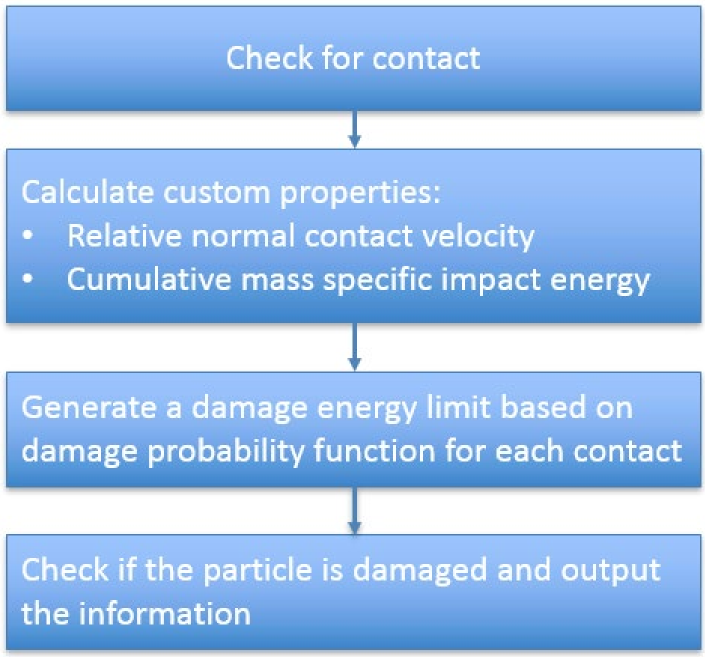

Fig. 6.1 The workflow of the impact damage model

The multiple impact damage model was elaborated in section 5.3.2. The cumulative effective impact energy , $E_{m,eff,cum}$, recorded for each particle can be used to estimate the damage fraction, *DF*. The relationship between the damage fraction and the cumulative effective impact energy was found to follow a Weibull distribution [19],

$$DF = 1 - \exp\{-f_{Mat.}k(E_{m,imp} - E_{m,min})\}^{\alpha} \tag{6.3}$$

where $f_{Mat.}$ and α are material parameters. Details regarding the characterization test used to acquire the parameters $f_{Mat.}$, α, and $E_{m,min}$ were provided in section 5.3.2. The test utilized a Wisconsin Breakage Tester (WBT) that could be adjusted to various rotational speeds, to apply impact loading to corn and wheat kernels.

For each contact event, a damage energy limit is randomly generated according to the damage probability function. For instance, if the damage probability function indicates that the damage probability for a particle with a cumulative effective impact energy of 100 J/kg is 30%, then there will be 30% chance that the damage energy limit is 100 J/kg. At the end of each contact event, the cumulative effective impact energy of the particle is compared with the corresponding damage energy limit. If the cumulative effective impact energy is smaller than the damage energy limit, no action will be taken. However, if the cumulative effective impact energy is larger than the limit, the particle will be marked as damaged and the information of the particle (particle ID, damage time, damage location, cumulative impact energy) will be output into an Excel file.

6.2.3 Validation Experiment

A modified Stein breakage tester (SBT) was used as the system to validate the damage model. A photo of the test stand is displayed in Fig. 6.2. The original usage of the device was to test the breakage susceptibility of the shelled corn kernel samples [28]. In the current study, the device was used to create impact damage to grain kernels. The reason to use the modified SBT instead of the traditional SBT is that radius of the blade of the modified SBT is longer than the blade of the traditional SBT. The longer blade has a higher tip speed and therefore it is able to generate more damage in a short time period.

The corn and wheat sample used in the tests were acquired from a local farm (Wright Agri Group, Covington, IN). The moisture contents of the grain samples were measured using the 72 hour whole kernel oven dring method [29]. The moisture contents were 14.7% and 13.9% wet basis for corn and wheat respectively. To generate uniform subsample sets, Boerner divider was used to split the sample into a certain sample size. Before feeding the grain kernel into the SBT, the sample was manually checked kernel by kernel. Only the whole kernels were saved for the test, i.e. cracked, broken, chipped, and kernels with pericarp damage were removed [30]. After the kernels were fed into the confined cup through the inlet, the switch of the device was turned on and the sample was processed for a predetermined time duration. During the test, the impacting blade was spun at a speed of 1788 rpm as measured by the tachometer. The processed sample was first sieved with a sieve (different sieves for corn and for wheat) to separate the fine material from the kernels. The kernels retained on the sieve were inspected individually and all the whole kernels were picked out. The remaining damaged kernels were combined with the fine material. The masses of the whole kernels and the damaged kernels were measured with an electronic balance. The damage fraction can be calculated as the ratio of the mass of the damaged kernels to the total sample mass.

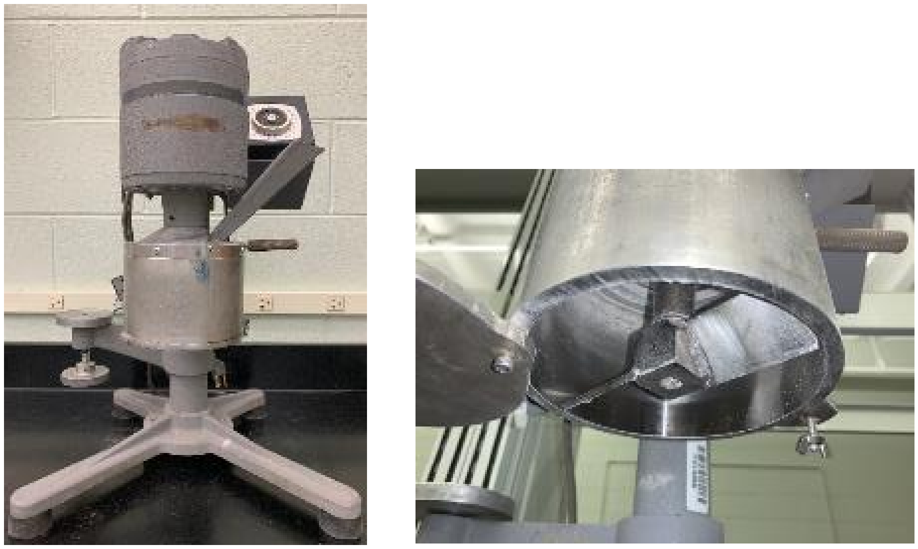

(a) (b)

Figure 6.2 Stein breakage tester. (a): Front view; (b): Impacting blade inside the confined cup

For this impact test, two parameters, i.e. sample size and time duration of the test, can be varied to create different test conditions. The sample sizes used for corn were 50-gram, 100-gram, and 150-gram. Only one sample size was used for wheat, 25-gram. The 100-gram corn and 25-gram wheat samples were impacted by the device for 15, 30, 45, and 60 seconds. For all the other sample sizes, only the samples impacted for 30 and 60 seconds were collected due to time limitations. For each test condition, the damage fractions of three replicates were determined. Table 6.1 provides a summary of the test conditions.

Table 6.1 Test conditions of the validation experiment

Test material	Sample size (gram)	Time duration (sec)
Corn	50	30
		60
	100	15
		30
		45
		60
	150	30
		60
Wheat	25	15
		30
		45
		60

6.2.4 Simulation Setup and Input Parameters

The grain kernel impact test conducted by the SBT was simulated using EDEM. The major parts of the SBT, including the inlet, the shaft, the blade, and the cup, were scanned with a 3D scanner (Creaform HandySCAN 700). The CAD models of the parts were reconstructed using Geomagic Design X (3D Systems, Rock Hill, SC) and imported into EDEM. Fig. 6.3 shows the geometric configuration used in the simulation.

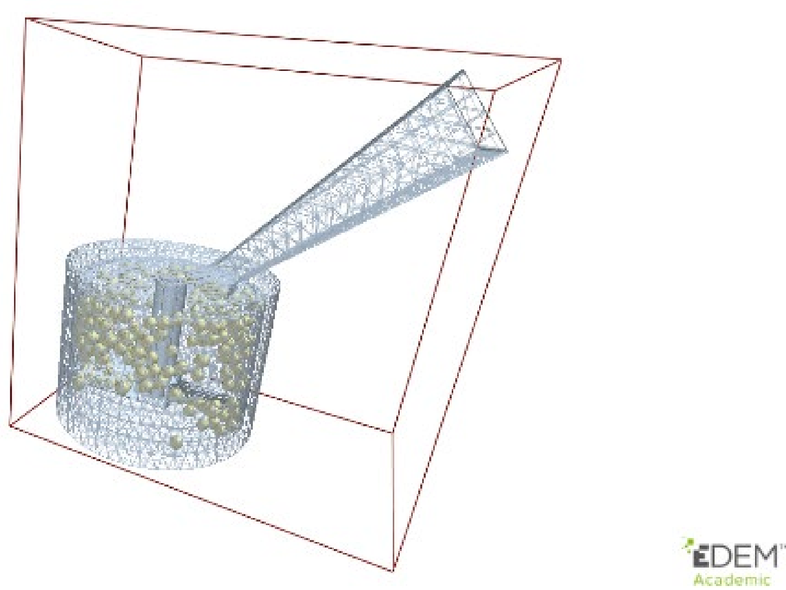

Figure 6.3 Geometric configuration of the SBT simulation

Most of the values of the input parameters used in the simulation, i.e. material properties, interaction properties, and the damage probability function, were either directly measured from the experiment or acquired from literature. A summary of the input parameters and corresponding sources of the values can be found in section 4.3.2. For particle shape, attempts were made to model the grain kernel as a glued-sphere particle. However, there were challenges when implementing the damage model. For this study, all the simulations used single spheres to model the grain kernels. The material used to construct the SBT is assumed to be steel. The material properties for the steel acquired from the Engineering Toolbox (https://www.engineeringtoolbox.com/) were 0.29 for Poisson's ratio, 7870 kg/m^3 for density and 205 GPa for Young's modulus.

6.3 Results and Discussion

6.3.1 Single Impact Simulation

A simple single impact simulation was used to verify that the model was able to generate reasonable values of the damage fraction based on the particle impact velocity and damage probability function that was used. In the simulation, a large number of particles were impacted normally on a flat surface at a fixed velocity of 15.6 m/s, as shown in Fig. 6.4. Each particle was only impacted once, and particle-particle contact was avoided. Using the damage probability function, the theoretical damage fraction for the test was found to be 0.53. Three simulations were conducted with a different number of particles being impacted, i.e. 100, 1000, and 10000 particles. The result is shown in Fig. 6.5 which indicates that, for all three tests, the damage fractions predicted by the simulations were close to the theoretical value. In addition, the difference between the simulation value and theoretical value decreased when the number of particles increased.

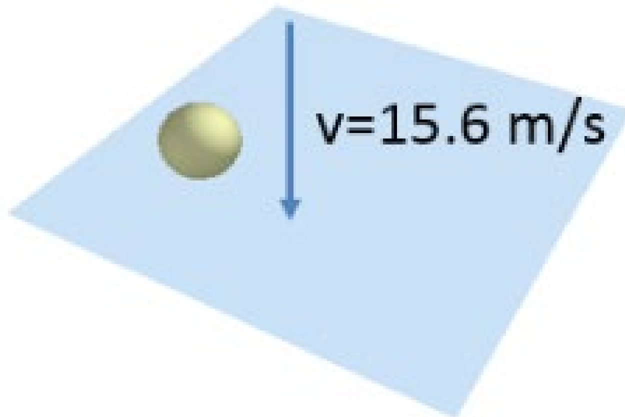

Fig. 6.4 Single impact simulation setup

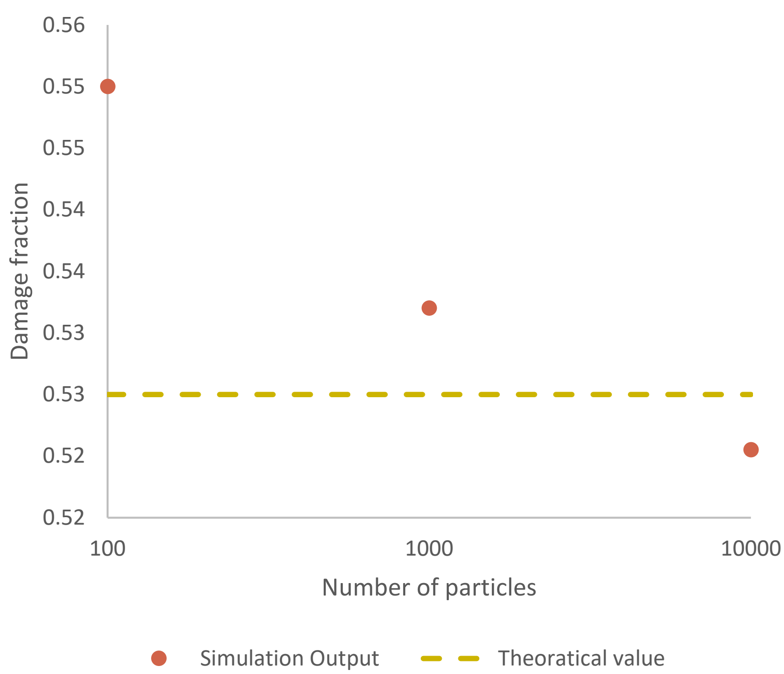

Fig. 6.5 Number of particles being impacted versus damage fraction

6.3.2 Multiple Impact Simulation

To verify that the cumulative effective impact energy was recorded correctly by the damage model, a single particle multiple impact simulation was created. In the simulation, the gravity was set to zero to facilitate interpretation of the velocity and impact energy data. A particle was shot downward in the box with the specified speed causing it to impact the bottom surface. The simulation configuration is shown in Fig. 6.6. The particle rebounds between the upper surface and bottom surface until the velocity decreases to zero. The normal impact velocity and the cumulative effective impact energy were recorded for each contact event and are plotted against time in Fig. 6.7. The result shows that: 1. the cumulative effective impact energy only increases when the energy increment of a given contact is larger than the threshold energy; 2. The cumulative effective impact energy only increases once for a given contact. These observations regarding the damage model demonstrate that it is able to predict the cumulative effective impact energy correctly.

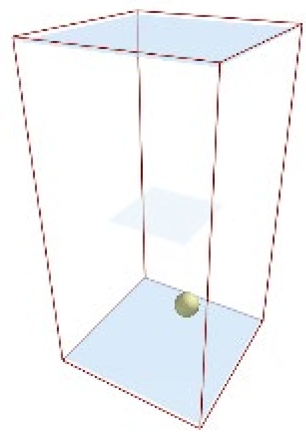

Fig. 6.6 Multiple impact test simulation configuration

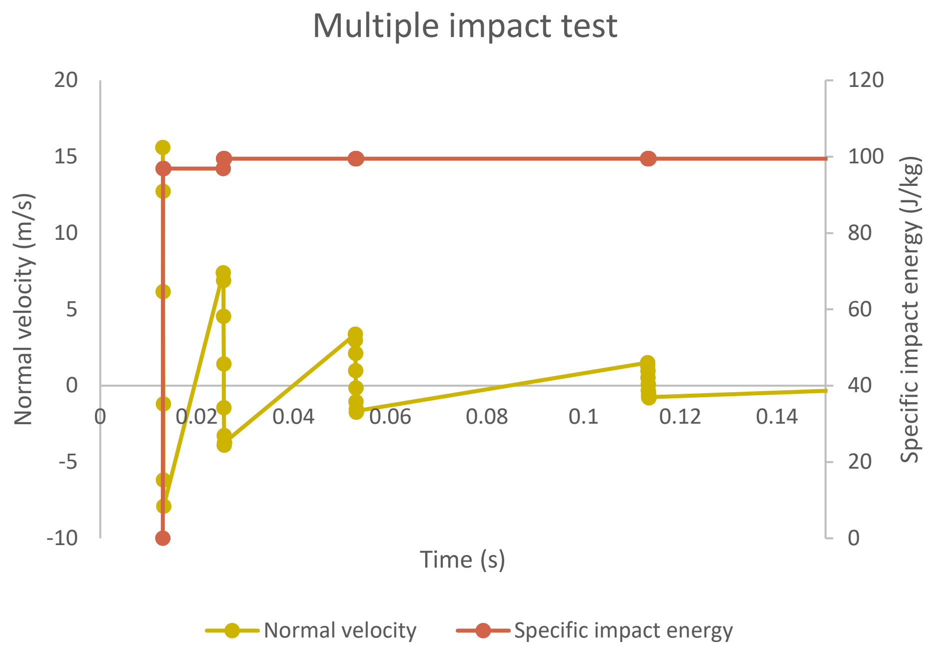

Fig. 6.7 Normal velocity and specific impact energy plot against time for multiple impact test simulation

6.3.3 Stein Breakage Tester

6.3.3.1 The Effect of Threshold Energy, $E_{m,min}$

SBT simulations were first conducted using the Weibull distribution parameters acquired from the characterization test (WBT). However, it was found that the simulation results deviated greatly from the results of the experiment. It was suspected that the damage probability function acquired from WBT test was not applicable to the SBT test, due to the difference in the damage mechanism of the two devices. Efforts were made to find a set of Weibull distribution parameters that would allow the simulation model to generate results that agree well with the results of the experiment. Different groups of Weibull distribution parameters were used as the input of the simulations. For each groups of parameters, the threshold energy was arbitrarily chosen; while the $f_{Mat.}$ and α were acquired by refitting the WBT data with the assigned threshold energy. This is based on the assumption that the $f_{Mat.}$ and α were measured correctly by the characterization test, while the threshold energy in the characterization test differed from the threshold energy in validation test.

Fig. 6.8 shows the change of the damage fraction over time when different groups of Weibull distribution parameters were used. The simulation results were plotted as lines, experiment measurements were plotted as dots, and the error bars show the 95% confidence intervals of the experimental measurements. In general, the damage fraction decreases with an increase in the threshold energy. This is because more low energy impact events will be considered as having no contribution to particle damage if the threshold energy increases. For corn, when the threshold energy was set to be 50 kg/J, the simulation results matched the experimental results well at all time levels. The simulation curve was within the 95% confidence intervals of the experimental measurements. However, for wheat, no threshold energy was found that made the simulation results agree well with experimental results at all timesteps. The mismatch of the results may indicate that the SBT system for wheat has different $f_{Mat.}$ and α values from the ones acquired from WBT test data.

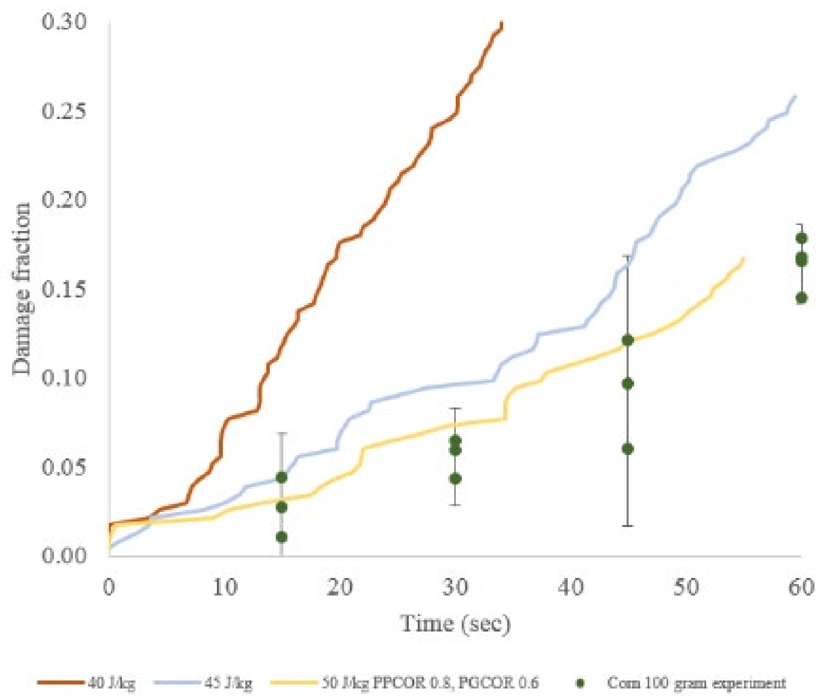

(a)

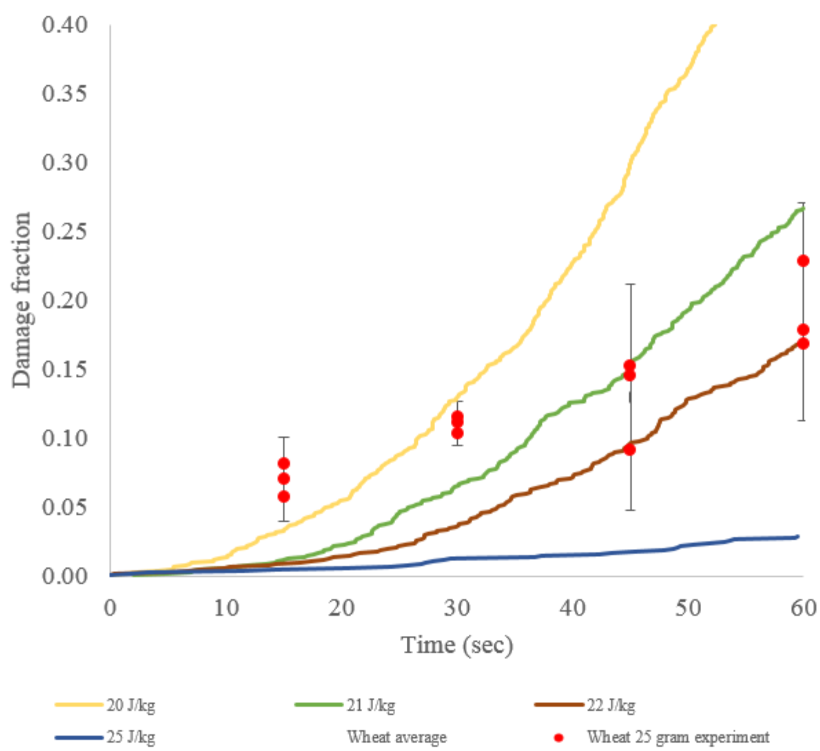

(b)

Fig. 6.8 Damage fraction versus time with different threshold energy levels. (a) 100-gram corn sample; (b) 25-gram wheat sample

6.3.3.2 The effect of sample size

As shown in the previous section, the model using 50 kg/J as the threshold energy gave a prediction that agreed well with the experimental result, when 100-gram corn sample was impacted in SBT. It would be interesting to see if the model could still give a good prediction of the damage fraction when different sizes of the sample are tested. Experimental measurements of the 50-gram and 100-gram corn samples are plotted in Fig. 6.9 with the corresponding simulation results. The damage model was able to give a prediction that agreed with the experimental data for both 50-gram and 150-gram sample sizes. Though the model overpredicts the damage fraction at 30 seconds for the 150-gram sample, the difference between the experimental mean value and the simulation value is only 0.02.

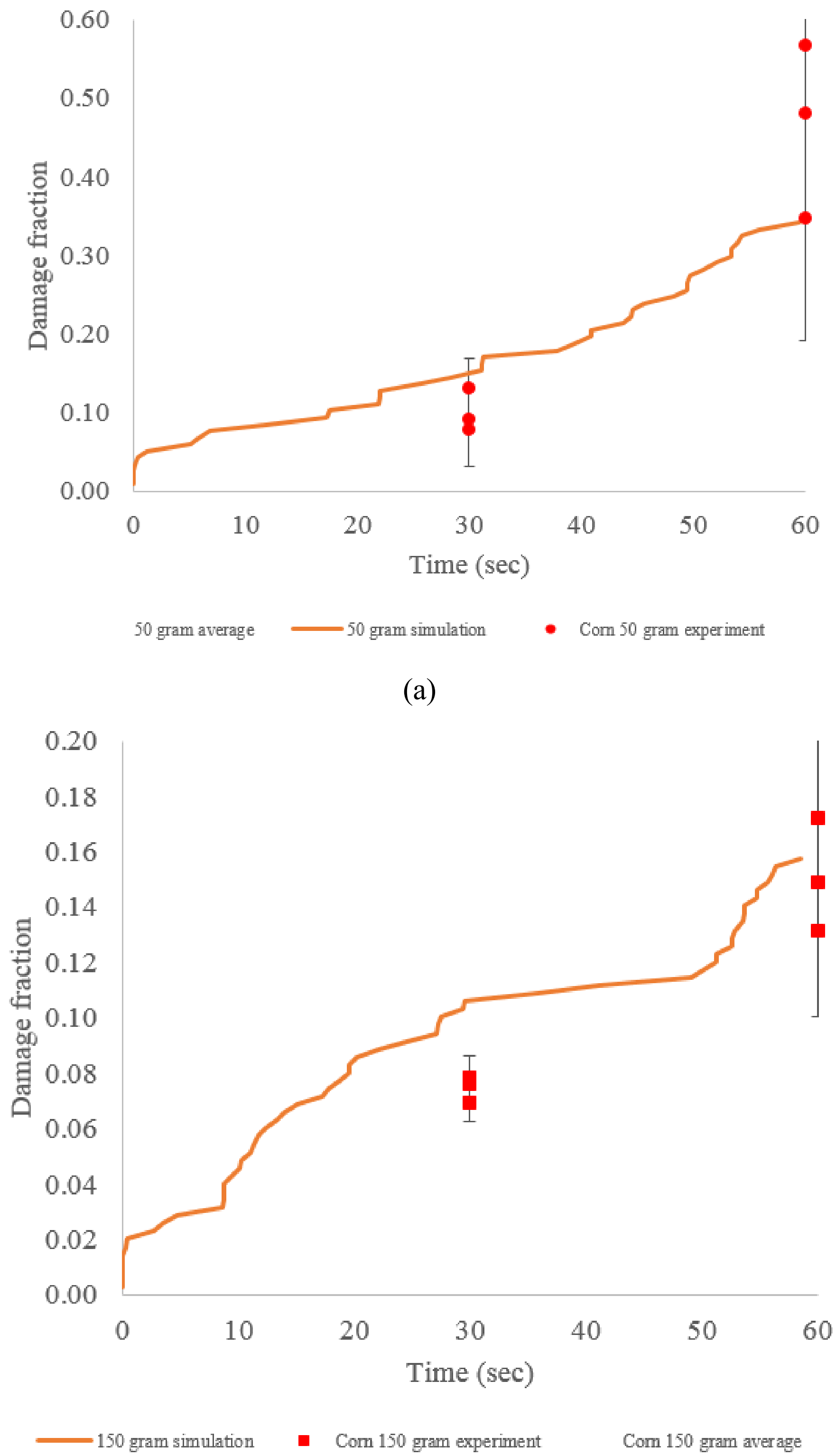

(a)

(b)

Fig. 6.9 Damage fraction versus time with different sample size. (a) 50-gram corn sample; (b) 150-gram corn sample

6.3.3.3 Effect of coefficient of restitution (COR)

In dilute phase flow, the COR usually has a major influence on particle flow behavior. The effect of COR on the damage fraction was investigated via sensitivity analysis. Two sets of corn kernel simulations were run with a fixed particle-particle COR and a fixed particle-geometry COR, respectively. The simulation results are shown in Fig. 6.10.

In one set of simulations, the particle-geometry COR was fixed at 0.6, and different particle-particle COR values, i.e. 0.2, 0.4, 0.6, and 0.8, was used. The results show that the damage fraction after one-minute of impact increases from 12 % to 22% as the particle-particle COR increases from 0.2 to 0.8. This change in damage fraction aligns with expectations. With a higher particle-particle COR, the particle velocity after the collision will be higher. Thus, more grain will be damaged by the higher impact energy.

In the other set of simulations, the particle-particle COR was fixed at 0.2, and the particle-geometry COR was varied as 0.2, 0.4, 0.5, 0.6, 0.7, and 0.8. It was found that the damage fraction after one-minute of impact decreases from 0 to 1 as the particle-geometry COR increases from 0.2 to 0.8. The damage fraction changed drastically with changes in particle-geometry COR, meaning that the damage fraction is very sensitive to particle-geometry COR. The exact reason for this phenomenon is not yet clear. One possible explanation is that for a high particle-geometry COR, the majority of the grain stays at the top of the SBT chamber and. Thus, there are fewer particle-blade impact events. On the other hand, for a low particle-geometry COR, the majority of the grain stays in the lower part of the chamber and there are a large number of particle-blade impact events. The particle-blade impact is considered as the major source of damage since the highest velocity impacts in the system occurs at the blade tip.

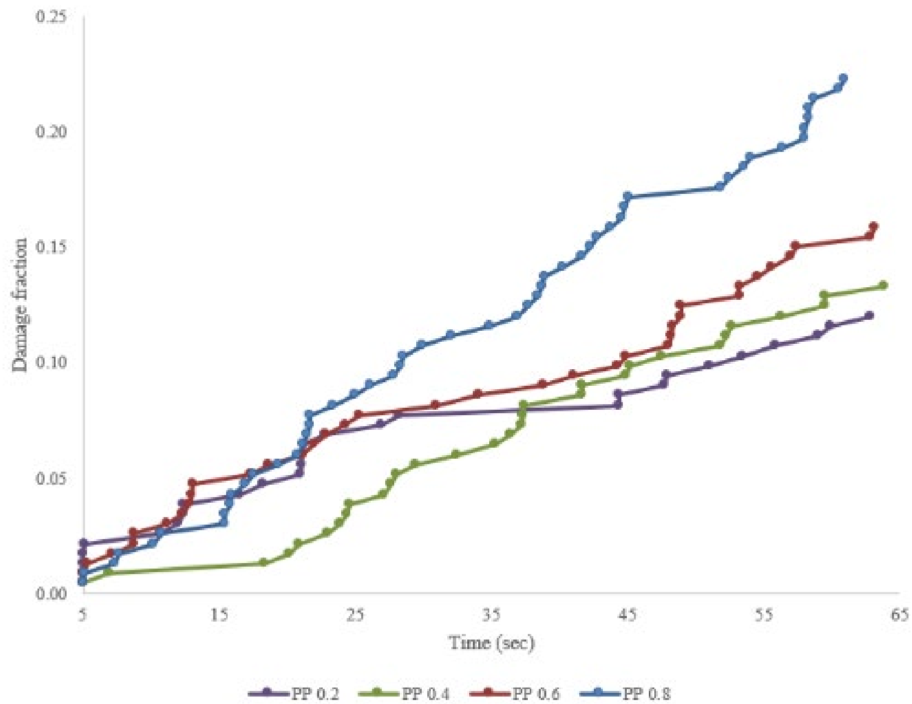

(a)

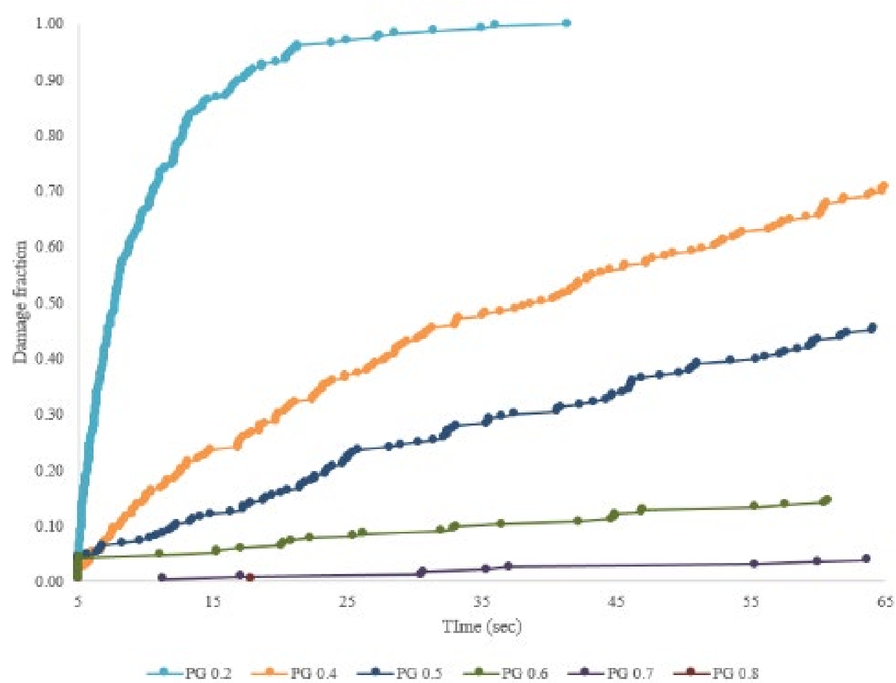

(b)

Fig. 6.10 Damage fraction versus time with different COR. (a) particle-geometry COR was fixed, and particle-particle COR was varied; (b) particle-particle COR was fixed, and particle-geometry COR was varied

6.3.3.4 Damage locations

DEM simulation is able to provide insight into a test system that is hard to be acquired from the experiment. There is no straight forward way to learn the damage location of the particles from the experiment. However, DEM simulation records the motion and loading condition of every individual particle at each time step, which makes it possible to output the damage locations. Locations of damaged particles for 100-gram corn sample after 60 seconds impact (represented as red dots) were displayed in Fig. 6.11. The side view (Fig. 6.11(a)) indicates that most of the particles were damaged at the height of the blade, while the top view (Fig. 6.11(b)) indicates that the majority of the particles were damaged at the tip of the blade. The results align with the expectation, as the highest velocity in the system is found at the blade tip.

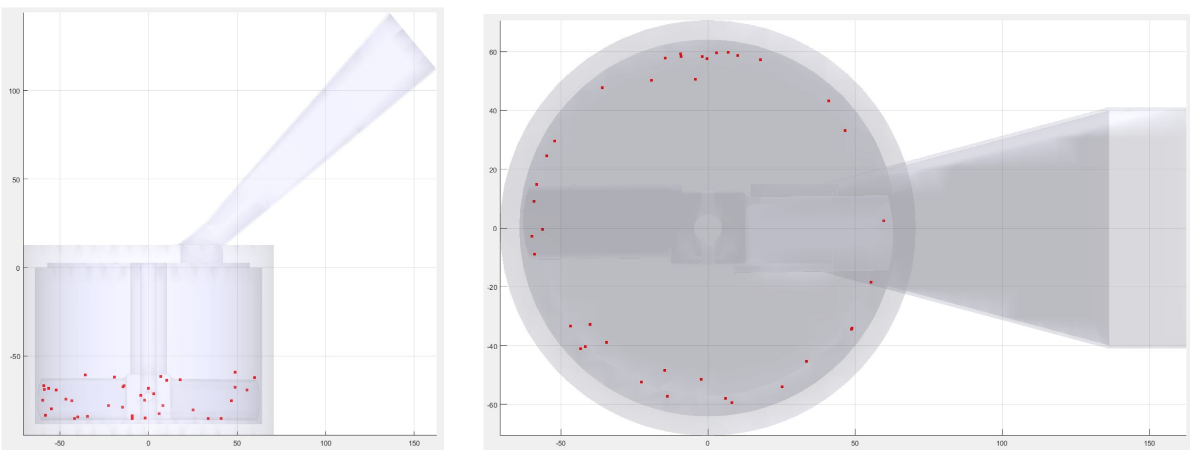

(a) (b)

Fig. 6.11 Locations of damaged particles for 100-gram corn sample after 60 seconds impact (modeled with threshold energy of 50 J/kg). (a) side view; (b) top view.

6.3.4 Model Limitations

6.3.4.1 Challenge of Using Glued-sphere Clump Model

Challenges were encountered when implementing the glued-sphere clump model for prediction damage. If multiple spheres in a single particle are in contact with another element, the impact energy calculation will be performed multiple times. However, the process should be considered as only one contact, and the calculation should only be performed once. Another pitfall of using the glued-sphere clump model was discussed by Kodam et al. [31]. When multiple component spheres of a glued-sphere clump particle are in contact, using an unchanged stiffness will result in a stiffer contact. Besides, using an unchanged damping coefficient will result in excessive damping. By comparing experimental results with the simulation, it was found that the dynamic bulk behavior of a few particles was not significantly affected by allowing multiple contacts. However, it had a significant effect on predicting the damage when a force threshold was used as the damage criteria [32].

6.3.4.2 Potential Reasons for Differences Between Experimental and Simulation Results

The inaccuracy of the simulation may come from three sources, i.e. input, model and output:

- Input

  The material properties, interaction properties, or damage probability functions may not be measured or assumed properly.

- Model
  - The model may not accurately reflect the damage mechanism. Some important factors may not be included in the model.
  - The model does not account for the effect of orientation. At the same loading, the damage probability may not be the same when the load is applied in different orientations.
  - The model does not account for the effect of loading location. For multiple loading events, loading at the same position multiple times will have a different effect from loading at multiple positions for multiple times.
  - The model does not account for the effect of the contact surface area. The model would consider contact with a flat surface and contact on a sharp edge or point as the same. However, when a kernel impacts a sharp edge there is a greater possibility of damage than when the same kernel impacts a flat surface. For WBT, the kernels were impacted on a flat surface. While for SBT, many of kernels were impacted by the sharp edge. With the same impact velocity, impacting on a sharp edge may have a higher damage probability than impacting on a flat surface, since higher stresses may be generated when impacting on the sharp edge.
  - The model does not account for the effect of shape. Challenges were encountered when implementing the glued-spheres model as described in the section above.

- Output

The approach used to quantify the damage directly affects the resulting damage fraction. For the sample tested in the WBT, the majority of the kernels were damaged severely, i.e. with open cracks, severe pericarp damage, or the kernels were crushed, and/or chipped. However, for the samples tested in the SBT, the majority of the kernels only had some minor damage, i.e. with hairline cracks and/or spots of pericarp missing. Some of the damage was difficult to identify. Thus, the damage fraction that occurred in the SBT tests may have been underestimated.

6.4 Summary

A modified Vogel and Peukert model was developed to predict the damage level and the damage location of grain kernels being process in handling devices. Grain impact damage experiments were conducted using the SBT. The same system was simulated by DEM implemented with the model. The effects of threshold energy, sample size, and coefficient of restitution on damage fraction were studied. However, it was found that the DEM simulation was not able to give a good prediction of the damage level when using the input parameters characterized by the WBT. The parameters were then recalibrated using the SBT. The new model did give a good prediction of the damage fraction for corn at different sample size levels and time levels when the newly calibrated parameter values were used. Comparing to the predictions of the corn kernel damage level, the simulation gave less accurate predictions of the damage level for wheat kernel. The wheat kernel simulation was able to accurately predict the experimental results only for impact duration of 45 and 60 seconds.

6.5 Reference

[1] Srivastava, A. K., Goering, C. E., Rohrbach, R. P., & Buckmaster, D. R. (2006). Grain Harvesting. In *Engineering Principles of Agricultural Machines* (2nd ed., pp. 403–435). St. Joseph, Michigan: American Society of Agricultural and Biological Engineers.

[2] Newbery, R. S., Paulsen, M. R., & Nave, W. R. (1980). Soybean quality with rotary and conventional threshing. *Transactions of the ASAE*, *23*(2), 303–308. Retrieved from http://ovidsp.ovid.com/ovidweb.cgi?T=JS&CSC=Y&NEWS=N&PAGE=fulltext&D=caba1&AN=19800713601 http://oxfordsfx.hosted.exlibrisgroup.com/oxford?sid=OVID:cabadb&id=pmid:&id=doi:&issn=0001-2351&isbn=&volume=23&issue=2&spage=303&pages=303-308&date=1980&title=Tran

[3] Chowdhury, M. H., & Buchele, W. F. (1978). The nature of corn kernel damage inflicted in the shelling crescent of grain combines. *Transactions of the ASAE*, *21*(4), 610–614. Retrieved from http://ovidsp.ovid.com/ovidweb.cgi?T=JS&CSC=Y&NEWS=N&PAGE=fulltext&D=caba1&AN=19792402148 http://oxfordsfx.hosted.exlibrisgroup.com/oxford?sid=OVID:cabadb&id=pmid:&id=doi:&issn=0001-2351&isbn=&volume=21&issue=4&spage=610&pages=610-614&date=1978&title=Tran

[4] Magee, K. J., Stroshine, R. L., Foster, G. H., & Baker, K. D. (1983). Nature and extent of grain damage caused by pneumatic conveying systems. In *Winter Meeting American Society of Agricultural Engineers American Society of Agricultural Engineers*.

[5] Hall, G. E., & Johnson, W. H. (1970). Corn kernel crackage induced by mechanical shelling. *Transactions of the ASAE*, *13*(1), 51–55.

[6] Jindal, V. K., Herum, F. L., & Hamdy, M. Y. (1979). Selected Breakage Characteristics of Corn. *Transactions of the ASAE*, *22*(5), 1193–1196.

[7] Singh, S. S., & Finner, M. F. (1983). A Centrifugal Impacter for Damage Susceptibility Evaluation of Shelled Corn. *Transactions of the ASAE*, *26*(6), 1858–1863.

[8] Keller, D. L., Converse, H. H., Hodges, T. O., & Chung, D. S. (1972). Corn Kernel Damage Due to High Velocity Impact. *Transactions of the ASAE*, *15*(2), 330–332.

[9] Evans, M. D., Holmes, R. G., & McDonald, M. B. (1990). Impact Damage To Soybean Seed As Affected By Surface Hardness and Seed Orientation. *Transactions of the ASAE*, *33*(1), 234–240.

[10] Kirk, I. W., & McLeod, H. E. (1967). Cottonseed Rupture from Static Energy and Impact Velocity. *Transactions of the ASAE*, *10*(2), 217–219.

[11] Sharda, R. (1976). *A Mechanical Damage Susceptibility Tester for Shelled Corn*. Ohio State University.

[12] Baryeh, E. A. (2002). Physical properties of millet. *Journal of Food Engineering*, *51*(1), 39–46. Retrieved from www.elsevier.com/locate/jfoodeng

[13] Khazaei, J., Shahbazi, F., Massah, J., Nikravesh, M., & Kianmehr, M. H. (2008). Evaluation and modeling of physical and physiological damage to wheat seeds under successive impact loadings: Mathematical and neural networks modeling. *Crop Science*, *48*(4), 1532–1544. doi:10.2135/cropsci2007.04.0187

[14] Burkhardt, T. H., & Stout, B. A. (1974). Laboratory Investigations of Corn Shelling Utilizing High-Velocity Impact Loading. *Transactions of the ASAE*, *17*(1), 11–14.

[15] Ptasznik, W., Barnard, J., Giec, W., & Khan, A. A. (1995). Susceptibility of Bean Seeds to Thermal and Impact Damage. *Journal of Agricultural Engineering Research*, *61*(2), 137–144. doi:10.1006/jaer.1995.1040

[16] Szwed, G., & Lukaszuk, J. (2007). Effect of rapeseed and wheat kernel moisture on impact damage. *International Agrophysics*, *21*(3), 299–304.

[17] Foster, G. H., & Holman, L. E. (1973). *Grain Breakage Caused by Commercial Handling Methods*. *Marketing Research Report* (Vol. No. 968).

[18] Tavares, L. M. (2009). Analysis of particle fracture by repeated stressing as damage accumulation. *Powder Technology*, *190*(3), 327–339. doi:10.1016/j.powtec.2008.08.011

[19] Vogel, L., & Peukert, W. (2003). Breakage behaviour of different materials - Construction of a mastercurve for the breakage probability. *Powder Technology*, *129*(1–3), 101–110. doi:10.1016/S0032-5910(02)00217-6

[20] Rozenblat, Y., Levy, A., Kalman, H., Peyron, I., & Ricard, F. (2013). A model for particle fatigue due to impact loads. *Powder Technology*, *239*, 199–207. doi:10.1016/j.powtec.2013.01.059

[21] Vogel, L., & Peukert, W. (2005). From single particle impact behaviour to modelling of impact mills. *Chemical Engineering Science*, *60*(18), 5164–5176. doi:10.1016/j.ces.2005.03.064

[22] Shi, F., & Kojovic, T. (2007). Validation of a model for impact breakage incorporating particle size effect. *International Journal of Mineral Processing*, *82*(3), 156–163. doi:10.1016/j.minpro.2006.09.006

[23] Bonfils, B., Ballantyne, G. R., & Powell, M. S. (2016). Developments in incremental rock breakage testing methodologies and modelling. *International Journal of Mineral Processing*, *152*, 16–25. doi:10.1016/j.minpro.2016.04.010

[24] Morrison, R. D., Shi, F., & Whyte, R. (2007). Modelling of incremental rock breakage by impact - For use in DEM models. *Minerals Engineering*, *20*(3), 303–309. doi:10.1016/j.mineng.2006.10.015

[25] Cleary, P. W., & Morrison, R. D. (2016). Comminution mechanisms, particle shape evolution and collision energy partitioning in tumbling mills. *Minerals Engineering*, *86*, 75–95. doi:10.1016/j.mineng.2015.12.006

[26] Bruchmüller, J., van Wachem, B. G. M., Gu, S., & Luo, K. H. (2011). Modelling discrete fragmentation of brittle particles. *Powder Technology*, *208*(3), 731–739. doi:10.1016/j.powtec.2011.01.017

[27] DEM Solutions Ltd. (2016). EDEM 2.6 Theory Reference Guide.

[28] Miller, B. S., Hughes, J. W., Rousser, R., & Pomeranz, Y. (1979). Note on a Method for Measuring Breakage Susceptibility of Shelled Corn During Handling. *Cereal Chemistry*, *56*(3), 213–216.

[29] ASABE Standard. (2017). *S352.2: Moisture Measurement-Unground Grain and Seeds*. St. Joseph, MI: ASABE. Retrieved from https://elibrary.asabe.org/azdez.asp?JID=2&AID=24272&CID=s2000&T=2

[30] U.S. Grains Council. (2017). *Corn harvest quality report*.

[31] Kodam, M., Bharadwaj, R., Curtis, J., Hancock, B., & Wassgren, C. (2009). Force model considerations for glued-sphere discrete element method simulations. *Chemical Engineering Science*, *64*, 3466–3475. doi:10.1016/j.ces.2009.04.025

[32] Scheffler, O. C., Coetzee, C. J., & Opara, U. L. (2018). A discrete element model (DEM) for predicting apple damage during handling. *Biosystems Engineering*, *172*, 29–48. doi:10.1016/j.biosystemseng.2018.05.015

7. CONCLUSIONS AND FUTURE WORK

7.1 Conclusions

This study aimed to develop a validated model for predicting grain kernel damage using DEM. To address this objective, a comprehensive literature review of grain kernel damage was conducted. The topics investigated included the types of damage, sources of damage, factors affecting damage, damage prediction models, and testing procedures. Grain mechanical damage can be classified into two types: external such as a removal of a chip from the kernel or a visible break in the kernel and internal such as a stress crack that develops inside the kernel and is only visible with illumination (corn kernels) or examination with X-rays (wheat kernels). The main damage mechanisms include impact, which causes external and internal cracks or even fragmentation of the kernel; attrition, which generates fine material; jamming, which deforms and breaks kernels due to high compressive forces; and fatigue, which produces broken kernels and fine material via repeatedly applied loads. Harvesting is the major cause of cracks and breakage while conveying after drying produces fine material. Grain kernel damage accumulates as the grain moves through the sequence of events in harvesting and handling. The damage level is affected by both the physical and mechanical properties of the grain and the loading conditions.

In this study, various types of testing devices were used to study the damage level under different loading conditions. Though many empirical models have been developed, only a few studies have attempted to develop mechanics-based models to predict grain kernel damage. The damage mechanisms of inorganic granular material has been extensively studied. Various mechanics-based damage prediction models have been proposed and successfully implemented in DEM. This study was the beginning of an effort to develop a DEM model that predicts grain damage by adapting these mechanics-based models.

The first step in predicting grain kernel damage with DEM is determining the material and interaction properties of corn and wheat kernels. Three different approaches were used. The X-ray micro-CT scanner, electronic balance, and reciprocating-pin tribometer were used to measure the particle shape, mass, particle-wall COF, and inter-particle COF, respectively, at the single particle level. The particle-wall CORs were calibrated using kernel drop tests. The values of other properties, including Young's modulus, Poisson's ratio, and inter-particle CORs, were acquired from the literature. The estimated parameters were used to simulate two bulk material tests: the bulk density test and the angle of repose test. The percent errors between experimental and simulated results were less than 10% for both corn and wheat. This indicates that the parameter values were properly estimated, and that the tests used in the study are appropriate for characterizing grain kernels for the purpose of DEM modeling.

The probability that grain kernels would be damaged as a result of loading by compression, impact, or abrasion was studied by measuring loading force or input energy that produced the damage. The resistance to damage by compression was determined using a universal testing machine. The average values of the fracture force are 309.4 $\pm$ 107.1 N and 83.4 $\pm$ 23.8 N for corn and wheat kernels, respectively. The average values of the fracture energy are 48.7 $\pm$ 27.1 mJ and 28.7 $\pm$ 13.5 mJ for corn and wheat kernels, respectively. A pin-on-disk tribometer was used to measure resistance to wear. The average work to cause wear damage on the kernels is 3.85 $\pm$ 1.50 J for wheat sliding against acrylic disk. The Wisconsin breakage tester was used to study resistance to repeated impact. A lognormal distribution was used to model compression damage and a Weibull distribution was used to model impact damage. The models provided a good prediction of the damage probability.

The statistical models were implemented in DEM to predict the damage level and location during grain handling process. Experiments and DEM simulations were conducted for the Stein breakage tester system to validate the impact damage model. The error between the experimental and simulation results was large, when using the damage resistance parameters characterized by the Wisconsin breakage tester. The damage resistance parameter, threshold energy, was recalibrated by matching the experimental and simulation results of running Stein breakage tester for 60 second with 100-gram of corn sample or 25-gram of wheat sample. The model could give a more accurate prediction of the damage level when using the newly calibrated parameters. For corn kernel, predictions of the simulation fell within the 95% confidence levels for the three replicates of the experiment both at different time levels and at different sample size levels. For wheat kernel, the simulation gave less accurate predictions comparing to the predictions of the corn kernel damage level. Predictions of the simulation fell within the 95% confidence levels for the three replicates of the experiment only for impact duration of 45 and 60 seconds.

7.2 Future Work

Many additional studies can be conducted to further enhance the performance of the model. Accurately measuring the model input parameters is critical to DEM simulations. First of all, it would be worth studying which parameters have a significant effect on the simulation output, how they affect the output, and why they affect the output by conducting a comprehensive sensitivity analysis. More effort should then be made to design and conduct tests to accurately measure or to determine them using calibration. As the grain kernel is a viscoelastic material, some of its mechanical properties, such as Young's modulus and COR, may change with the loading rate. Thus, it is important to measure the properties at the conditions that the gain experiences during the production process. It may also be necessary to study how the properties change with a change of loading rate.

In this thesis work, the Young's modulus values used in the simulation were acquired from the literature. More accurate values may be measured at the single particle level or determined by calibration at the bulk material level. The Young's modulus of the kernel can be directly measured using an indentation test [1]. However, one study found that the Young's moduli at different locations on a corn kernel were different [2]. Therefore, using Young's modulus measured at a single location in the simulation may not result in an accurate bulk material behavior. Another possibility would be to calibrate Young's moduli using a bulk compression test. For the test, a certain weight of kernels is placed in a topless container. The kernels are then compressed by a flat plate placed on top of the kernels. The plate displacement and the normal load applied to the plate are recorded. The same system can be simulated in DEM and Young's modulus can be varied to match the force-displacement behavior acquired from the experiment.

The kernel drop test system used in this study to measure the particle-wall COR is not suitable for measuring the inter-particle COR. A test system that can measure the inter-particle COR may be designed and constructed. The double pendulum method may be adopted to measure the inter-particle COR at the single particle level [3]. The vibrating table test could be used to calibrate the inter-particle COR at the bulk material level [4].

As discussed in section 6.3.4, a problem was encountered when implementing the impact damage model in conjunction with a glued-sphere clump model. The shape of the kernel was represented with the single-sphere model in the current study. More efforts could be made to make the damage model compatible with the glued-sphere or polyhedron shape representation.

As discussed in section 6.3.3, a large error between the experimental and simulation results was observed, when using the damage resistance parameters characterized by the Wisconsin breakage tester (WBT). One possible reason for this large error may be that in the WBT, the kernels impacted on the surface at either tip or crown orientation; while in the SBT, the kernels impacted the blade at random orientation. To overcome this challenge, another characterization test which has a damage mechanism similar to the mechanism of the SBT could be developed. Replacing the impellor in the Wisconsin breakage tester with two impacting blades and make the kernel impact on these blades may be a possible way of solving the orientation problem. In this way, the kernels would impact normally to the surface at random orientations.

In this thesis work, though models of three different damage mechanisms were implemented in DEM, only the impact damage model was validated. Future work includes the validation of compression and wear damage models. One key aspect of validation is to design test systems in which only one type of damage mechanism is dominant in each system. The test system should also be simple, so that the computational time required for a parameter study is reasonable. For the compression damage model, a bulk compression test may be used for validation. A different validation tests distinct from the bulk compression test used to calibrate Young's modulus is needed for independent verification. In the validation test, a higher normal load should be applied to the kernels until compression damage occurs. The friction damage model may be validated with a test system similar to the tangential abrasive dehulling device described in section 5.1 [5].

7.3 References

[1] González-Montellano, C., Fuentes, J. M., Ayuga-Téllez, E., & Ayuga, F. (2012). Determination of the mechanical properties of maize grains and olives required for use in DEM simulations. *Journal of Food Engineering*, *111*(4), 553–562. doi:10.1016/J.JFOODENG.2012.03.017

[2] Wang, L., Zhou, W., Ding, Z., Li, X., & Zhang, C. (2015). Experimental determination of parameter effects on the coefficient of restitution of differently shaped maize in three-dimensions. *Powder Technology*, *284*, 187–194. doi:10.1016/j.powtec.2015.06.042

[3] Hlosta, J., Žurovec, D., Rozbroj, J., Ramírez-Gómez, Á., Nečas, J., & Zegzulka, J. (2018). Experimental determination of particle–particle restitution coefficient via double pendulum method. *Chemical Engineering Research and Design*, *135*, 222–233. doi:10.1016/j.cherd.2018.05.016

[4] Elskamp, F., Kruggel-Emden, H., Hennig, M., & Teipel, U. (2017). A strategy to determine DEM parameters for spherical and non-spherical particles. *Granular Matter*, *19*(3), 46. doi:10.1007/s10035-017-0710-0

[5] Oomah, B. D., Reichert, R. D., & Youngs, C. G. (1981). A Novel, Multi-Sample, Tangential Abrasive Dehulling Device (TADD). *Cereal Chemistry*, *28*(5), 392–395. doi:10.1016/s0315-5463(81)72811-6

APPENDIX

MATLAB codes

```
%%%%%%%%%%%%%%%%%%%%%%%%%%%%%%%%%%%%%%%%%%%%%%%%%%%%%%%%%%%%%%%%%%%%%%%%%%%%
% Analysis angle of repose images 1
%%%%%%%%%%%%%%%%%%%%%%%%%%%%%%%%%%%%%%%%%%%%%%%%%%%%%%%%%%%%%%%%%%%%%%%%%%%%
function [x, y] = outline(filename, type)
    % Read the image and separate the data into 3 channels.
    I = imread(filename);
    R = I(:,:,1);
    G = I(:,:,2);
    B = I(:,:,3);
    dim = size(I);
    mask = zeros(dim(1),dim(2));

    % Using color threshold to do a first segmentation
    for i = 1:dim(1)
        for j = 1:dim(2)
            if strcmp(type,'corn')
                if R(i,j)>1.8*B(i,j)
                    mask(i,j) = 1;
                end
            elseif strcmp(type,'wheat')
                if R(i,j)>1.6*B(i,j)
                    mask(i,j) = 1;
                end
            elseif strcmp(type,'simulation')
                if B(i,j)<200
                    mask(i,j) = 1;
                end
            end
        end
    end
    % Morphological operation to enhance the image mask
    se_1 = strel('disk',2);
    mask = bwmorph(mask,'open'); % Performs morphological opening (erosion followed by dilation), 
remove noise
    mask = imclose(mask,se_1); % Performs morphological closing (dilation followed by erosion), 
closing small holes
    mask = imfill(mask,'holes'); % Fill image regions and holes
    mask = bwareaopen(mask,1000); % Remove small objects from binary image
    % mask = bwpropfilt(mask,'area',[700 800]); % Extract objects from binary image using 
properties
    bw = logical(mask);
%     Hblob = vision.BlobAnalysis;
%     [areas,centroids,bbox] = Hblob(bw);
    figure
    imshowpair(I,bw,'montage')

    % Find outline
    x = zeros(1, dim(2));
    y = zeros(1, dim(2));
    scale_ratio = 150/dim(2);
    for j = 1:dim(2)
        x(j) = j*scale_ratio;
        for i = 1:dim(1)-1
            if (mask(i,j) == 0) && ((mask(i+1,j) == 1))
                y(j) = (dim(1)-i)*scale_ratio;
                break
            end
        end
    end
end
```

```
%%%%%%%%%%%%%%%%%%%%%%%%%%%%%%%%%%%%%%%%%%%%%%%%%%%%%%%%%%%%%%%%%%%%%%%%%%%
% Analysis angle of repose images 2
%%%%%%%%%%%%%%%%%%%%%%%%%%%%%%%%%%%%%%%%%%%%%%%%%%%%%%%%%%%%%%%%%%%%%%%%%%%
clear;clc;close all;
%% Acquire outlines for corns
x = cell(1, 6);
y = cell(1, 6);
[x{1,1}, y{1,1}] = outline('outline_exp_corn7.png', 'corn');
[x{1,2}, y{1,2}] = outline('outline_exp_corn8.png', 'corn');
[x{1,3}, y{1,3}] = outline('outline_exp_corn9.png', 'corn');
[x{1,4}, y{1,4}] = outline('outline_sim_corn1.png', 'simulation');
[x{1,5}, y{1,5}] = outline('outline_sim_corn2.png', 'simulation');
[x{1,6}, y{1,6}] = outline('outline_sim_corn3.png', 'simulation');

figure
set(gcf,'units','centimeters ')
x_dim=10;
y_dim=10;
width=30;
height=8;
set(gcf,'position',[x_dim,y_dim,width,height])

plot(x{1,1}, y{1,1},'r')
hold on
plot(x{1,2}, y{1,2},'r')
plot(x{1,3}, y{1,3},'r')
plot(x{1,4}, y{1,4},'b')
plot(x{1,5}, y{1,5},'b')
plot(x{1,6}, y{1,6},'b')
xlabel('x (mm)')
ylabel('H (mm)')
legend('Experiment1','Experiment2','Experiment3','Simulation1','Simulation2','Simulation3')
%% Compare two outlines
x=unique([x1 x2]);
Y1=interp1(x1,y1,x);
Y2=interp1(x2,y2,x);
diff=Y2-Y1;
root_ssq = rssq(diff(~isnan(diff)));
figure
set(gcf,'units','centimeters ')
x0=10;
y0=10;
width=30;
height=8;
set(gcf,'position',[x0,y0,width,height])
plot(x1,y1)
plot(x, diff)
xlabel('x (mm)')
ylabel('delta H (mm)')
%% Compare two images
exp = imread('outline_exp_corn.png');
sim = imread('outline_sim_corn.png');
figure
imshowpair(exp,sim,'montage')
%% Pile height to radius ratio
ratio = zeros(1,6);
for i=1:length(x)
    yi = y{1,i};
    mid = round(length(yi)/2);
    ratio(i) = yi(mid)/75;
end
ratio_exp = mean(ratio(1:3));
ratio_sim = mean(ratio(4:6));
ratio_exp_std = std(ratio(1:3));
ratio_sim_std = std(ratio(4:6));
error = (ratio_sim-ratio_exp)/ratio_exp*100;
```

```
%%%%%%%%%%%%%%%%%%%%%%%%%%%%%%%%%%%%%%%%%%%%%%%%%%%%%%%%%%%%%%%%%%%%%%%%%%%%
% Analysis high speed camera images of Wisconsin breakage tester
%%%%%%%%%%%%%%%%%%%%%%%%%%%%%%%%%%%%%%%%%%%%%%%%%%%%%%%%%%%%%%%%%%%%%%%%%%%%
function velocity = TwoFramesVelCal(Frame1, Frame2, foldername)
    %% Input parameters
    folderpath = 'Z:\GraduateSchool\Research Project\Experiment\Wisconsin Breakage
Tester\Velocity Calculation\Manual\High speed video\Frames\';
    figure1_path = ['Frame' num2str(Frame1) '.jpg'];
    figure2_path = ['Frame' num2str(Frame2) '.jpg'];
    figure1 = imread([folderpath foldername '\' figure1_path]);
    figure2 = imread([folderpath foldername '\' figure2_path]);
    framerate = 1/2000;

    %% Spatial Calibration
    [centers, radii, ~] = imfindcircles(figure1,[30 60],'EdgeThreshold',0);
    [radius, index] = max(radii);
    center = centers(index,:);
    real_radius = 24.05/2;
    % mm/pixel
    scalerate = real_radius/radius;

    %% Overlay frames
    I = imfuse(figure1, figure2, 'falsecolor');

    %% Separate the data into 3 channels.
    R = I(:,:,1);
    G = I(:,:,2);
    B = I(:,:,3);
    dim = size(I);
    G_mask = zeros(dim(1),dim(2));
    R_mask = zeros(dim(1),dim(2));

    %% Using color threshold to do a first segmentation
    for i = 1:dim(1)
        for j = 1:dim(2)
            if R(i,j)>2*G(i,j) %??? how to find this threshold
                R_mask(i,j) = 1;
            elseif G(i,j)>2*R(i,j)
                G_mask(i,j) = 1;
            end
        end
    end

    %% Morphological operation to enhance the image mask
    se_1 = strel('disk',2);
    R_mask = bwmorph(R_mask,'open'); % Performs morphological opening (erosion followed by
dilation), remove noise
    R_mask = imclose(R_mask,se_1); % Performs morphological closing (dilation followed by
erosion), closing small holes
    R_mask = imfill(R_mask,'holes'); % Fill image regions and holes
    R_mask = bwareaopen(R_mask,50); % Remove small objects from binary image
    R_mask_props  = regionprops(R_mask);
    R_mask = bwpropfilt(R_mask,'area',[600 800]); % Extract objects from binary image using
properties

    G_mask = bwmorph(G_mask,'open');
    G_mask = imclose(G_mask,se_1);
    G_mask = imfill(G_mask,'holes');
    G_mask = bwareaopen(G_mask,50);
    G_mask_props  = regionprops(G_mask);
    G_mask = bwpropfilt(G_mask,'area',[600 800]);

    %% Generate the final mask and calculate the result.
    mask = R_mask + G_mask;
    bw = logical(mask);
    Hblob = vision.BlobAnalysis;
    [areas,centroids,~] = Hblob(bw);

    % se_2 = strel('line',20,20);
    % mask = imerode(mask,se_2);
    % regions = regionprops(mask,'centroid');
```

```
    % centroids = cat(1, regions.Centroid);

    distance = pdist(centroids,'euclidean')*scalerate;
    velocity = distance/framerate/1000;

    %% Show the results
    % Plot the spetial calibration
    figure(1)
    imshow(figure1)
    viscircles(centers, radii,'EdgeColor','b');
    title('Spatial Calibration')
    hold on
    plot(center(1),center(2), 'b*')
    text(center(1),center(2), ['num2str(scalerate) ' mm/pixel'], 'Color','red','FontSize',10)
    hold off

    % Show overlaid image
    figure(2)
    imshow(I)
    title('Overlaid Image')

    % Show kernels centroids
    figure(3)
    imshow(bw)
    hold on
    plot(centroids(:,1),centroids(:,2), 'b*')
    hold off

    % Show velocity
    % fprintf('Impact velocity is %d m/sec\n', velocity)
End

%% Calculate velocities for multiple frames
function velocities = MultFramesVelCal(FrameF, FrameL, foldername)
    velocities = zeros(1,FrameL-FrameF);
    for n = FrameF:(FrameL-1)
        velocities(n-FrameF+1) = TwoFramesVelCal(n, n+1, foldername);
    end
end
```

```
%%%%%%%%%%%%%%%%%%%%%%%%%%%%%%%%%%%%%%%%%%%%%%%%%%%%%%%%%%%%%%%%%%%%%%%%%%%
% Analysis inter-particle coefficient of friction test data
%%%%%%%%%%%%%%%%%%%%%%%%%%%%%%%%%%%%%%%%%%%%%%%%%%%%%%%%%%%%%%%%%%%%%%%%%%%
clear;clc;close all;
% load data
load('data_wheat.mat', 'data')
dynamic_COF = [];
for j = 1:length(wheat_wheat)
    i = wheat_wheat(j);
    i=90;
    elm = data{i};
    range = [1800, 12400];
    T = elm(range(1):range(2), 1);
    Fx = elm(range(1):range(2), 2);
    Fz = elm(range(1):range(2), 3);
    x = elm(range(1):range(2), 4);
    z = elm(range(1):range(2), 5);
    dz = elm(range(1):range(2), 5) - max(z);
    COF = elm(range(1):range(2), 9);

    average_COF = mean(COF);

    angles = [];
    diff = 200;
    t = T((1+diff/2): (length(COF)-diff/2));

    for n = (1+diff/2): (length(COF)-diff/2)
        z_distance = abs(dz(n-diff/2)- dz(n+diff/2));
        x_distance = abs(x(n-diff/2) - x(n+diff/2));
        angle = pi/2-atan(z_distance/x_distance);
        angles = [angles, angle];
    end
    angles_degree = angles * 57.2958;
    figure;
    plot(t,angles_degree)
    title('T vs Contact angle')
    xlabel('T (sec)')
    ylabel('Contact angle (deg)')

    actual_COF = [];
    angle_change = [];
    diff2 = 50;
    tt = T((1+diff/2+diff2/2): (length(COF)-diff/2-diff2/2));
    for n = (1+diff/2+diff2/2): (length(COF)-diff/2-diff2/2)
        angle = angles(n-diff/2);
        if angle*57.2958 >= 85 || angle*57.2958 <= 80
            angle = nan;
        end
        angle_change =[angle_change, angles(n-diff2/2-diff/2)-angles(n-diff/2+diff2/2)];
        if abs(angles(n-diff2/2-diff/2)-angles(n-diff/2+diff2/2))>0.01
            angle = nan;
        end

        if COF(n) <= average_COF
            temp = abs( (abs(Fx(n))*sin(angle)+Fz(n)*cos(angle)) / (Fz(n)*sin(angle)-
abs(Fx(n))*cos(angle)) );
        else
            temp = abs( (abs(Fx(n))*sin(angle)-Fz(n)*cos(angle)) /
(abs(Fx(n))*cos(angle)+Fz(n)*sin(angle)) );
        end

        if temp>max(COF)
            temp = nan;
        end

        actual_COF = [actual_COF, temp];
    end

    dynamic_COF = [dynamic_COF,nanmean(actual_COF)];

    figure
```

```
    plot(tt,actual_COF)
    hold on
    plot(T,COF)
    legend('Processed data','Original data')
    xlabel('T (sec)')
    ylabel('COF')
end
```

```
%%%%%%%%%%%%%%%%%%%%%%%%%%%%%%%%%%%%%%%%%%%%%%%%%%%%%%%%%%%%%%%%%%%%%%%%%%%%
% Analysis particle-wall coefficient of friction test data
%%%%%%%%%%%%%%%%%%%%%%%%%%%%%%%%%%%%%%%%%%%%%%%%%%%%%%%%%%%%%%%%%%%%%%%%%%%%
clear;clc;close all;
%% Calculate static and dynamic COF
load('data_wheat.mat', 'data')
for i=93
    elm = data{i};
    range = [1, 12400];
    T = elm(range(1):range(2), 1);
    Fx = elm(range(1):range(2), 2);
    Fz = elm(range(1):range(2), 3);
    x = elm(range(1):range(2), 4);
    z = elm(range(1):range(2), 5);
    dz = elm(range(1):range(2), 5) - max(elm(range(1):range(2), 5));
    COF = elm(range(1):range(2), 9);
    time_step = 0.005;
    h = figure(i);
    set(h,'visible','on');
    xlabel('T (sec)')
    ylabel('COF')
    ylim([0 0.15])
    box on
    % Find valley by invert the data
    invertedCOF = max(COF) - COF;
    % Find the peak values and the peak indexes
    [peakValues, indexes] = findpeaks(invertedCOF, T, 'MinPeakDistance',5);
    peakValues = max(COF) - peakValues;
    peakNum = numel(indexes);

    % Find the sliding interval, discard the first and the last periods
    sliding_interval = zeros(peakNum-2, 2);
    discard_region = 200;
    for idx = 2:peakNum-1
        sliding_interval(idx-1,1) = int16(indexes(idx)/time_step + discard_region);
        sliding_interval(idx-1,2) = int16(indexes(idx+1)/time_step - discard_region);
        hold on
        ax = gca;
        ax.ColorOrderIndex = 1;
        plot(T(sliding_interval(idx-1,1):sliding_interval(idx-1,2)), COF(sliding_interval(idx-
1,1):sliding_interval(idx-1,2)))
    end

    % Calculate the dynamic COF
    mean_sliding_interval = zeros(peakNum-2,1);
    for idx = 1:peakNum-2
        mean_sliding_interval(idx) = mean(COF(sliding_interval(idx,1):sliding_interval(idx,2)));
    end
    dynamic_COF = mean(mean_sliding_interval);

    % Calculate the static COF for acrylic, discard the first and last periods
    % Get the static COF by finding the MAX
    static_COF_list_acrylic = zeros(peakNum-2,2);
    region_width = 150;
    for idx = 2:peakNum-1
        index = int16(indexes(idx)/time_step);
        [M, I] = max(COF(index:(index+region_width)));
        static_COF_list_acrylic(idx-1, 1) = I+index;
        static_COF_list_acrylic(idx-1, 2) = M;
    end
    static_COF = nanmean(static_COF_list_acrylic(:,2));
end
```

```
%%%%%%%%%%%%%%%%%%%%%%%%%%%%%%%%%%%%%%%%%%%%%%%%%%%%%%%%%%%%%%%%%%%%%%%%%%%
% Show damage location using data output by DEM simulation
%%%%%%%%%%%%%%%%%%%%%%%%%%%%%%%%%%%%%%%%%%%%%%%%%%%%%%%%%%%%%%%%%%%%%%%%%%%
clear;clc;close all;
%% Plot 3D geometry
function Plot3DGeometry()
    [v,f,name] = stlRead('stein_large_impeller.stl');
    figure;
    object.vertices = v;
    object.faces = f;
    patch(object,'FaceColor',       [0.8 0.8 1.0], ...
             'EdgeColor',       'none',        ...
             'FaceLighting',    'gouraud',     ...
             'AmbientStrength', 0.15,   ...
             'FaceAlpha', 0.1);

    % Add a camera light, and tone down the specular highlighting
    camlight('headlight');
    material('dull');

    % Fix the axes scaling, and set a nice view angle
    axis('image');
    view([-135 35]);
    grid on;
    title(name);
    hold on
end


%% Read in data values
filename = 'D:\Zhengpu\Wisconsin breakage tester\contact.csv';
[num,txt,raw] = xlsread(filename);
% Split data based on type of contact
particle_geometry = num(num(:,9)==0,:);
particle_particle = num(num(:,9)==1,:);

%% Impact energy delta histogram
ImpactEnergy_Delta = num(:,6);
histogram(ImpactEnergy_Delta)
xlabel('ImpactEnergy Delta')
ylabel('Frequency')

%% Particle-geometry contact
% Plot3DGeometry()
x_pg = particle_geometry(:,3)*1000;
y_pg = particle_geometry(:,4)*1000;
z_pg = particle_geometry(:,5)*1000;
ImpactEnergy_Delta_pg = particle_geometry(:,6);
Norm_velocity_pg = particle_geometry(:,8);
scatter3(x_pg,y_pg,z_pg, 10, Norm_velocity_pg,'filled')
colorbar
caxis([7, 20])
%% Particle-particle contact
% Plot3DGeometry()
x_pp = particle_particle(:,3)*1000;
y_pp = particle_particle(:,4)*1000;
z_pp = particle_particle(:,5)*1000;
ImpactEnergy_Delta_pp = particle_particle(:,6);
Norm_velocity_pp = particle_particle(:,8);
scatter3(x_pp,y_pp,z_pp, 10, Norm_velocity_pp,'filled')
colorbar
caxis([7, 20])
%% Check how many events are particle-blade edge impact
Plot3DGeometry()
particle_edge = particle_geometry(particle_geometry(:,4)*1000>-66.8 &
particle_geometry(:,4)*1000<-60.8,:);
x_pe = particle_edge(:,3)*1000;
y_pe = particle_edge(:,4)*1000;
z_pe = particle_edge(:,5)*1000;
ImpactEnergy_Delta_pe = particle_edge(:,6);
Norm_velocity_pe = particle_edge(:,8);
```

```
scatter3(x_pe,y_pe,z_pe, 10, Norm_velocity_pe,'filled')
colorbar
caxis([7, 20])
%% Check negative velocity
Plot3DGeometry()
negative_velocity = num(num(:,8)<0,:);
x_nv = negative_velocity(:,3)*1000;
y_nv = negative_velocity(:,4)*1000;
z_nv = negative_velocity(:,5)*1000;
ImpactEnergy_Delta_nv = negative_velocity(:,6);
Norm_velocity_nv = negative_velocity(:,8);
scatter3(x_nv,y_nv,z_nv, 10, Norm_velocity_nv,'filled')
colorbar

%% Plot damage location with scatter point (not working)
for i=1:length(num)
    % circle for particle-geometry contact
    if num(i,9)==0
        scatter3(num(i,3),num(i,4),num(i,5), 'o', 'r')
    % cross for particle-particle contact
    elseif num(i,9)==1
        scatter3(num(i,3),num(i,4),num(i,5), 'x', 'g')
    end
    hold on
end
%% Plot 3D histogram
close all
figure('position', [200, 200, 500, 400]);
h1 = histogram2(x,y,[24 12],'FaceColor','flat');
colorbar

figure('position', [700, 200, 500, 400]);
h2 = histogram2(x,z,[12 12],'FaceColor','flat');
colorbar

figure('position', [1200, 200, 500, 400]);
h3 = histogram2(y,z,[12 12],'FaceColor','flat');
colorbar

%% Plot 3D model
[v,f,name] = stlRead('stein_large_impeller.stl');
figure;
object.vertices = v;
object.faces = f;
patch(object,'FaceColor',       [0.8 0.8 1.0], ...
         'EdgeColor',       'none',        ...
         'FaceLighting',    'gouraud',     ...
         'AmbientStrength', 0.15,   ...
         'FaceAlpha', 0.1);

% Add a camera light, and tone down the specular highlighting
camlight('headlight');
material('dull');

% Fix the axes scaling, and set a nice view angle
axis('image');
view([-135 35]);
grid on;
title(name);
hold on
```